

# MODELLING INTERSTELLAR EXTINCTION IN STELLAR POPULATIONS

**Alexander Lisboa-Wright**

A thesis submitted in partial fulfilment of the requirements of Liverpool John Moores  
University for the degree of Master of Philosophy

Astrophysics Research Institute  
Faculty of Engineering and Technology

October 2019

## Abstract

In stellar astrophysics, the determination of the magnitude of interstellar extinction is critical, due to its effect on the observed brightness and colour of the stars. Extinction is therefore an important factor in deriving scientific information from the colour-magnitude diagrams (CMDs) of stellar populations. The treatment of extinction in standard CMD analyses is to employ constant ratios of extinction in each photometric filter relative to the visual Johnson- $V$  filter, denoted  $A_X/A_V$  in a generic filter  $X$ .

This work presents a theoretical analysis of the behaviour of the extinction ratios  $A_X/A_V$  in multiple photometric systems as the values of three stellar parameters (effective temperature, surface gravity and metallicity) were varied. The results of this analysis show significant variations in the value of  $A_X/A_V$  with changes in the stellar parameters. Analytic functions of these stellar parameters are proposed to describe these variations.

Also presented is an application of these results to a highly-reddened star cluster whose members also have accurate Gaia parallax measurements. When a proper analysis, which considers the variation of extinction ratios with stellar parameters, is used on the cluster data, it is shown that there is a non-negligible impact on the age determination for the cluster.\*\*\*\*ADD NUMERICAL RESULTS!!!

## Units & Terminology

Unless stated otherwise, all quantities will be described in CGS units (masses in grams, lengths in centimetres, times in seconds, energies in ergs).

In this project, the notation  $\log(x)$  represents the logarithm of  $x$  to the base 10. The natural logarithm of  $x$  will be expressed as  $\ln(x)$ .

Each of the quantities below is relevant to this project and, unless stated otherwise, will be the only quantity denoted by the symbol assigned to it below.

$M$  : mass

Luminosity :  $L$

Radius :  $R$

Gravitational acceleration :  $g$

Solar mass :  $M_{\odot} = 1.989 \times 10^{33} \text{ g}$

Solar luminosity :  $L_{\odot} = 3.842 \times 10^{33} \text{ erg s}^{-1}$

Solar radius :  $R_{\odot} = 6.957 \times 10^{10} \text{ cm}$

Gravitational constant :  $G = 6.6723 \times 10^{-8} \text{ cm}^3 \text{ g}^{-1} \text{ s}^{-2}$

Planck's constant :  $h = 6.6261 \times 10^{-27} \text{ cm}^2 \text{ g s}^{-1}$

Boltzmann's constant :  $k_B = 1.3806 \times 10^{-16} \text{ cm}^2 \text{ g s}^{-2} \text{ K}^{-1}$

Stefan-Boltzmann constant :  $\sigma_{\text{SB}} = 5.678 \times 10^{-5} \text{ erg cm}^{-2} \text{ K}^{-4} \text{ s}^{-1}$

parsec (pc) :  $1 \text{ pc} = 3.086 \times 10^{18} \text{ cm}$

\*\*\*\*ADD TEXT LINKING PARAGRAPHS!!!

# Chapter 1

## Introduction

### 1.1 \*\*\*\*Interstellar extinction

#### 1.1.1 Physical origin & definition

As the light emitted from a star travels towards a distant observer, its intensity, or flux, decreases with distance via an inverse-square law. Stars emit light across the full range of the electromagnetic spectrum. Therefore, a beam of light from a star will consist of photons with an extremely wide range of wavelengths.

However, the interstellar medium (ISM) is not a perfect vacuum. It contains many different structures, such as clouds of diffuse gas and dust grains, that can absorb or scatter light passing through. For a given light source, this causes its brightness to appear lower than it would otherwise and changes the distribution of the brightness with photon wavelength. A beam containing photons with a sufficiently large range of wavelengths will therefore lose some of its photons, and therefore flux, due to interactions with the ISM through which it travels. The magnitude of loss is determined by the wavelengths of the photons, the fraction of the beam consisting of photons at those wavelengths and the state of the ISM. For a given source, its interstellar extinction value represents the fraction of its original flux absorbed or scattered due to all extinction events along the line-of-sight between the source and the observer.

Optical extinction in the ISM is dominated by contributions from dust grains (Gontcharov, 2016). The effect of dust clouds on optical light travelling towards observers is particularly apparent when examining star clusters and galaxies (including the Milky Way), with the dust obscuring optical light from sources behind the clouds. One prominent example of an interstellar dust cloud extinguishing optical light from background stars is the Coalsack Nebula.

Mathematically, extinction,  $A$ , is defined using the standard astronomical system of flux magnitudes via the following equation:

$$\begin{aligned}
m - M &= 5 \log \left( \frac{d}{\text{pc}} \right) - 5 + A \\
&= (m_0 - M) + A
\end{aligned} \tag{1.1}$$

where  $m$  is the apparent magnitude of the source,  $M$  is its absolute magnitude,  $d$  is the distance to the source,  $m_0$  is the intrinsic apparent magnitude and  $(m_0 - M)$  is the (true) distance modulus.

When a broadband beam of light passes through a dust cloud, the loss of flux due to absorption or scattering is related to the optical depth,  $\tau$ . The optical depth is defined along the line-of-sight via:

$$\tau(l) = \int_0^l \rho \kappa dl = \int_0^l n \sigma dl \tag{1.2}$$

where  $l$  is the length of the path taken by the beam through the cloud,  $\rho$  is the mass density of the local cloud material,  $\kappa$  is the material's opacity,  $n$  is the particle number density and  $\sigma$  is the particle interaction cross-section.

It should be noted that all quantities in the integrands in Equation 1.2 depend on local conditions at each point along the path travelled by the beam. These quantities therefore cannot be immediately discounted as being constant along the entire path required for the integration, let alone throughout the entire cloud. Furthermore, the dependence\*\*\*\* of opacity, and subsequently optical depth, on the chemical composition of the dust causes a variation of its value with the wavelength of photons in the beam.

The variation in flux of the light beam with distance travelled through the cloud  $l$  is best expressed using the optical depth:

$$f(l) = f_0 e^{-\tau(l)} \tag{1.3}$$

where  $f$  is the flux of the beam after it exits the cloud and  $f_0$  is the flux at the point where the beam first encounters the cloud (i.e., at  $l = 0$ ). Returning to Equation 1.1, we can use the relation in Equation 1.3, together with the standard equation which defines the relationship between two different magnitudes, to define extinction in terms of optical depth:

$$A = m - m_0 = -2.5 \log \left( \frac{f}{f_0} \right) = -2.5 \log(e^{-\tau}) \tag{1.4}$$

Therefore, we can define the extinction in terms of the distance travelled through, and the composition of, the ISM, both of which are accounted for in the optical depth:

$$A = 2.5 \log(e) \times \tau = 1.086\tau \approx \tau \quad (1.5)$$

In conclusion, to a first-order approximation, the extinction is equal to the optical depth along the line of sight. Hence, the mathematical representation of extinction is proven to be aligned with its physical definition as the fraction of photons scattered and absorbed by the interstellar dust.

The incidence of absorption and scattering events depends, in part, on the wavelength of the incoming photons. This dependence is also incorporated into the optical depth via the interaction cross-section  $\sigma$  in Equation 1.2. If a dust particle in the ISM is (naively) assumed to be spherical with radius  $r$ , the Mie solution (Mie, 1908) to Maxwell's equations can be used to estimate the extinction cross-section of the dust grains. The Mie solution describes the scattering of EM waves in the specific case in which the waves interact with homogeneous dielectric spheres, such as atoms and particles, and is accurate for all wavelengths.

According to the Mie solution, the light extinguished by a dielectric sphere can be described by an infinite series of partial EM waves radiated by the electric and magnetic multipoles in the sphere (Grainger et al., 2004), with each partial wave corresponding to a given multipole order  $n$ . A dimensionless extinction efficiency factor  $Q_{\text{ext}}$ , representing the ratio of the sphere's extinction cross-section to its geometric cross-section ( $\pi r^2$ ) can be calculated analytically using this approach. Figure 1.1 shows the behaviour of  $Q_{\text{ext}}$  with changing wavelength  $\lambda$  when all other parameters, including particle type and size, are fixed.  $Q_{\text{ext}}$  is plotted as a function of the so-called size parameter  $\alpha = (2\pi r/\lambda) \propto 1/\lambda$ .

For the regime in which particles are much larger than the wavelength of the incoming light ( $\lambda \ll r$ , which is on the right of the figure),  $Q_{\text{ext}}$  becomes constant with regard to wavelength, converging to a value of 2 through the damped oscillation beginning at the graph peak at  $\alpha \sim 6$ . In the limit where  $\lambda \gg r$ , the Mie solution produces the standard theory of Rayleigh scattering for small particles, meaning that  $Q_{\text{ext}}(\lambda) \propto \lambda^{-4}$  and, consequently  $Q$  decreases towards zero at progressively larger wavelengths, shown by the behaviour of the curve in Figure 1.1 between the origin and the straight-line ( $\lambda \sim r$ ) region.

Crucially, when the photon wavelength is on the order of the dust particle size ( $\lambda \sim r$ ),  $Q_{\text{ext}} \propto r/\lambda$ , as seen in the straight-line region of Figure 1.1. Therefore, for a sphere of known radius  $r \sim \lambda$ , the extinction cross-section  $\sigma(\lambda)$  follows the same behaviour as  $Q_{\text{ext}}$ :

$$\sigma(\lambda) = Q_{\text{ext}}(\lambda)\pi r^2 \propto \frac{\pi r^3}{\lambda} \quad (1.6)$$

meaning that, for a given dust particle with known radius  $r$ , its contribution to the

extinction cross-section is proportional to  $1/\lambda$ .

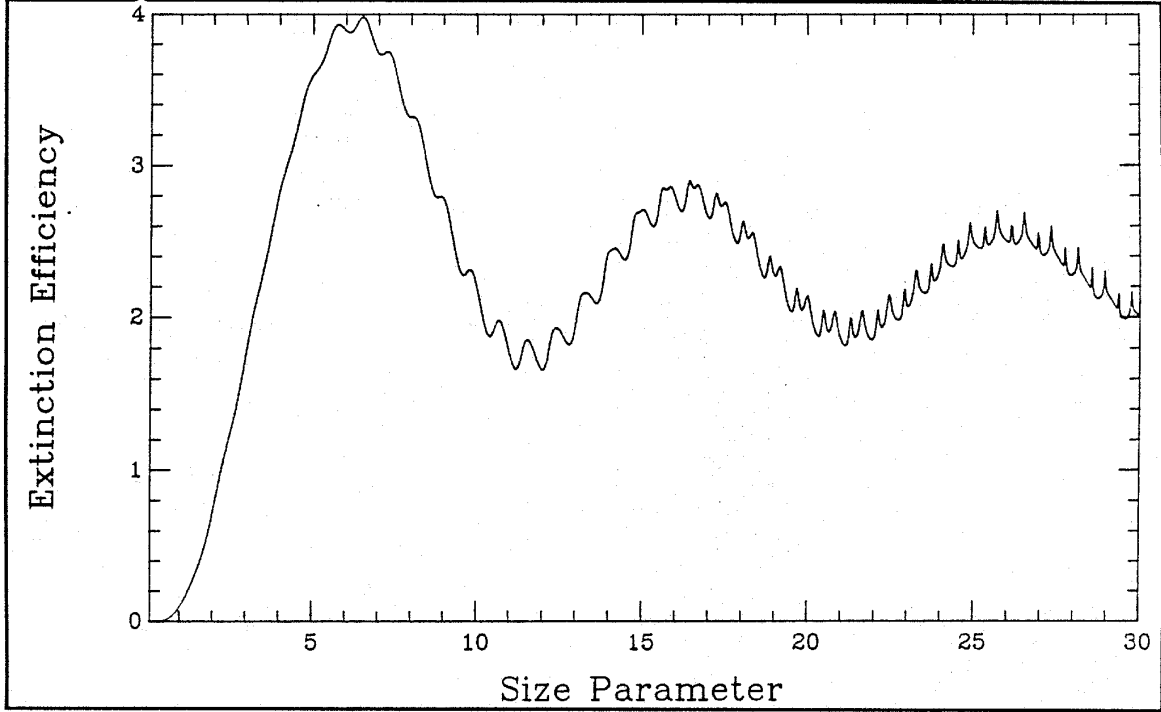


Figure 1.1: The variation of  $Q_{\text{ext}}$  as a function of the size parameter  $\alpha = (2\pi r/\lambda)$  at a fixed value (1.33) of the complex refractive index  $m$ . Source: <http://eodg.atm.ox.ac.uk/user/grainger/research/book/protected/Chapter5.pdf>

As mentioned earlier, at wavelengths in and around the optical spectral region, the absorption mechanism in the ISM is dominated by interstellar dust. Typical interstellar dust grains have radii ranging between 100 and 1000 nm (Witt, 2000), but the dominant grain size is 300 nm (Landgraf et al., 2003). Therefore, the condition  $\lambda \sim r$  is satisfied for interstellar dust in the UV-to-near-IR spectral range, which covers approximately a 100-1000 nm wavelength range. Therefore,  $\sigma(\lambda)$  is greatest when the photon wavelength is in the region of 300 nm, which is located within the UV wavelength regime. The effect of extinction is therefore significantly greater in the UV than in the IR. Although this spherical model is somewhat simplistic for the case of interstellar dust grains, its general conclusions align with observational results.

If we refer back to Equations 1.2 and 1.3, with this knowledge of the behaviour of  $\sigma$ , it can be seen that in the UV-to-NIR regime, the optical depth (and hence extinction) is greater at shorter, bluer wavelengths, which causes the source star to appear redder than its true colour. Hence, the effect of extinction is sometimes referred to as “reddening”.

### 1.1.2 Empirical extinction curves

From the results of Mie scattering summarised in Section 1.1.1, it is clearly very important to both understand and measure any variations in extinction. In fact, the observed variation of extinction with wavelength discussed in the previous section has been studied for decades. Various authors have produced empirical results intended to better model the changes in the magnitude of extinction over an extended wavelength range, as explicit functions of wavelength or as values or functions unique to each one of a selection of photometric filters.

Rieke & Lebofsky (1985) found that outside dense molecular clouds, which have high opacities and whose lines-of-sight are less frequently used in observations as a result, all extinction laws for all the filters they studied were uniform between wavelengths of 1 and 13  $\mu\text{m}$  when observing sources in the direction of the Galactic Centre. This result was then used to produce constant ratios of the extinction in those filters ( $A_X$ , where  $X$  represents a generic photometric filter) to the extinction in the  $V$  filter ( $A_V$ ), part of the Johnson-Cousins (Johnson & Morgan, 1953) filter system which has long been the standard system of filters in UV-IR spectral observations. The ratio between the extinction in  $X$  and that in  $V$  is denoted by  $A_X/A_V$ . They also determined the now-widely used global average value of 3.08 ( $\sim 3.1$ ) for  $R_V \equiv A_V/E_{B-V}$ , known as the total-to-selective extinction ratio, for the diffuse ISM.

Cardelli et al. (1989) used observations of mostly bright, hot O- and B-type main-sequence stars to produce empirical equations describing the mean ratio of extinction values at a specific wavelength  $\lambda$  ( $A_\lambda$ ) to the  $V$ -band extinction ( $A_V$ ), this ratio being denoted  $A_\lambda/A_V$ . The study produced a basic equation of the form:

$$A_\lambda/A_V = a(x) + b(x)/R_V, \quad (1.7)$$

where  $x \equiv 1/\lambda$ . The significance of  $R_V$ , as noted in the same paper, comes from its usefulness as an indicator of the nature of the interstellar medium through which the observed light travels in order to reach the observer. The total wavelength range was divided into 4 sub-ranges, each with a governing pair of empirically-determined equations to calculate  $a(x)$  and  $b(x)$ , respectively. The extinction-ratio profiles calculated using Equation 1.7 for three lines of sight are displayed in Figure 1.2.

This model underpins more recent studies of intrinsic effects on extinction (Girardi et al., 2008; Casagrande & Vandenberg, 2014, 2018a,b), and provides the basis for the synthetic  $A_X/A_V$  datasets in this project. Equation 1.7 has become a standard model for theoretical studies to employ for predictions made in the UV, optical and near-IR wavelength regions, although it is not always accurate (O'Donnell, 1994; Fitzpatrick,



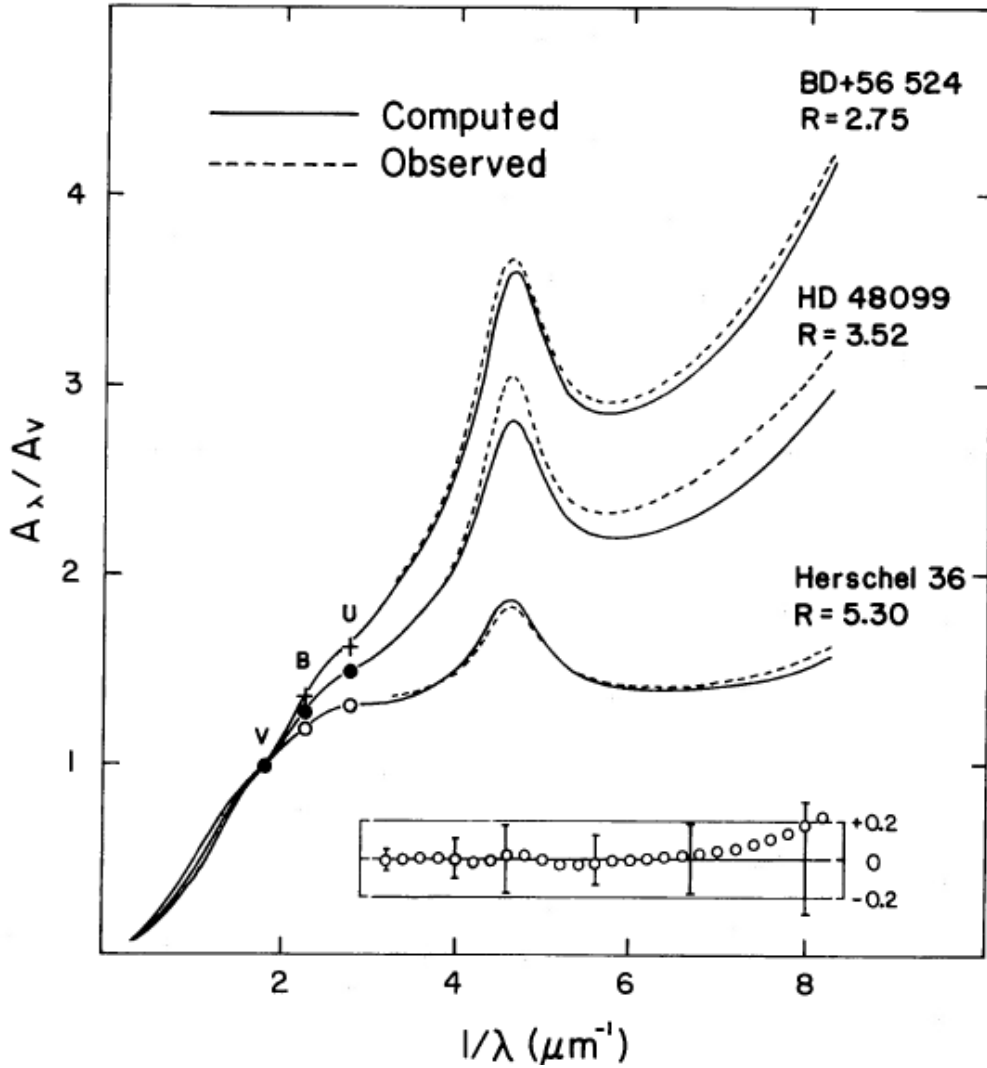


Figure 1.2: Variation of the extinction, normalised to the  $V$ -band extinction  $A_V$ , as a function of wavelength, in spectral regions ranging from the IR (left) to the UV (right). The solid lines are calculated using Equation 1.7 at the given  $R_V$  values. These values represent the lines of sight for their respective source stars, which are listed alongside. Source: Cardelli et al. (1989)

1999).

O'Donnell (1994) found deviations from the Cardelli et al. (1989) extinction law in the soft-UV spectral range using a sub-sample of 22 stars from the same dataset. This was attributed to the uncertainty in the short-wavelength cutoff of the UV-range Johnson  $U$  filter and to the presence of the Balmer discontinuity within the limits of the filter bandpass.

Fitzpatrick (1999) found that, due to the broadband nature of the Johnson filters and the general decrease of extinction with wavelength, the Cardelli et al. (1989) relations overestimate the extinction in the near-IR and blue-visible Johnson filters. The study put forward corrections to the equations for  $a(x)$  and  $b(x)$  for these wavelength regions. However, in the UV region covered by the Cardelli et al. (1989) equations, Valencic et al. (2004) found the equations to be accurate for 93% of a homogeneous UV observational database.

Casagrande & VandenBerg (2014, 2018a,b) created simple models for the parameter  $R_X = (A_X/E_{B-V})$ , consisting of a quadratic variation with effective temperature and a linear variation with metallicity (they found no significant variations with surface gravity) in multiple telescope filter systems. This was based on MARCS model stellar atmospheres, which have an upper effective temperature limit of 8000K (Gustafsson et al., 2008). The equation is independent of surface gravity and has the following form:

$$R_X = a_0 + T_4(a_1 + a_2 T_4) + a_3 [\text{Fe}/\text{H}] \quad (1.8)$$

where  $T_4 = 10^{-4} \times T_{\text{eff}}$  and  $T_{\text{eff}}$  is the effective temperature. The equation is valid for  $5250\text{K} \leq T_{\text{eff}} \leq 7000\text{K}$ . Although these models are mathematically simple (with only 4 coefficients), the limited  $T_{\text{eff}}$  range in which they are applicable is problematic, particularly in the red giant branch (RGB) and lower main sequence of any stellar population.

## 1.2 Extinction in stars & stellar populations

This project examines the effect of extinction treatment methods on interpretations of observed stellar populations. All star emits light from their surfaces, above which the photons can travel much more freely than in the stellar interior. However, the emitted photons must pass through the stellar atmosphere immediately above the surface before reaching the ISM or a distant observer. The stellar atmosphere contains atomic and ionic species which can interact with the photons. The level of interaction between the photons and the atmosphere depends not only on the photons' wavelengths but also on the nature of the atmosphere itself, which is governed by the type of star in question.\*\*\*\*

### 1.2.1 The effect of extinction on the observed magnitudes of different stellar types

To understand how extinction affects the observed magnitudes of different stellar types, we must first define the fundamental parameters that describe a stellar atmosphere, where the observed beam is first emitted by the star. This is important because these

parameters will be used in this project as the input variables on which any star-to-star variations in extinction will be modelled. Stellar atmospheres are defined by three stellar parameters: the effective temperature, surface gravity and metallicity.

### Effective temperature

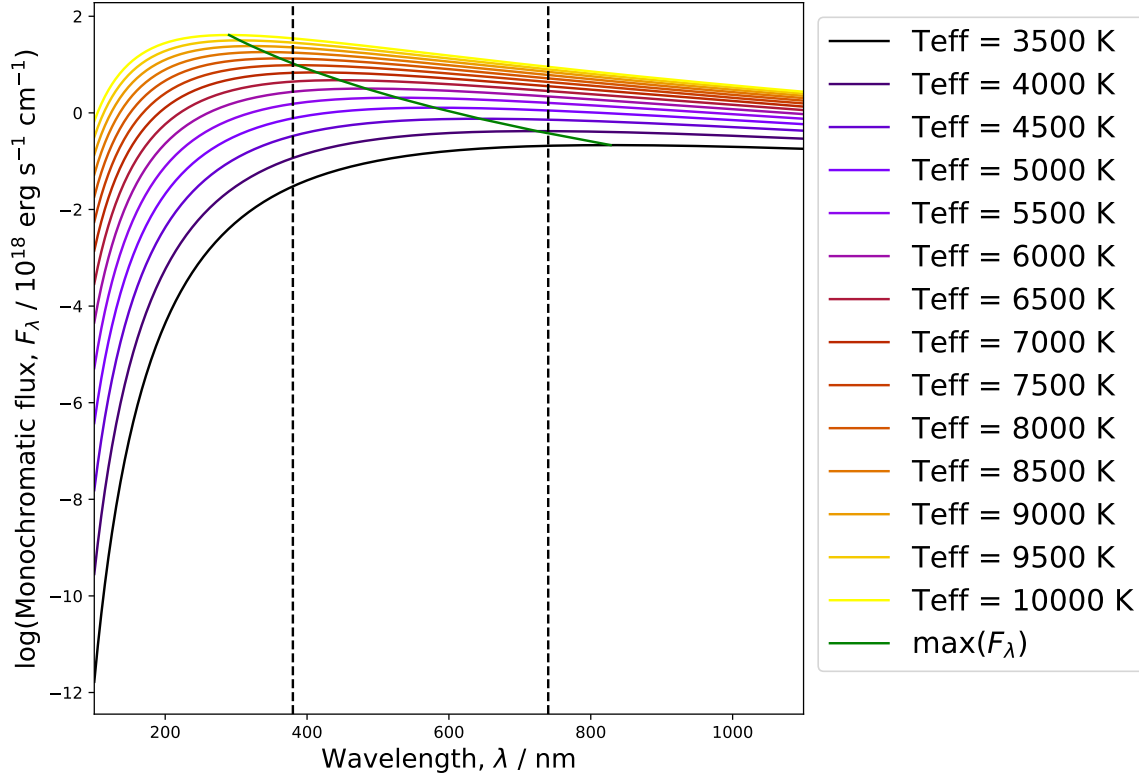


Figure 1.3: Plot of the logarithm of monochromatic flux of a black body for different stellar effective temperatures, as a function of wavelength. The black dashed lines mark the approximate limits of the visible part of the EM spectrum. The green curve represents the variation of the Planck Law maxima with effective temperature.

The effective temperature ( $T_{\text{eff}}$ ) of a star is defined as the thermodynamic temperature of a black body which produces the same stellar flux across all wavelengths (known as the bolometric flux) as that produced by the star. The equation of the radiation emitted by a black body produces the body's flux per unit wavelength per unit angular viewing area,  $F_{\lambda,bb}$ , known as the black body's monochromatic flux. The equation, known as the Planck Law, is as follows:

$$F_{\lambda,bb} = \frac{2hc^2}{\lambda^5 \left( \exp \left( \frac{hc}{\lambda k_B T} \right) - 1 \right)} \quad (1.9)$$

where  $T$  is the thermodynamic temperature of the black body,  $h$  is Planck's constant,  $c$  is the vacuum speed of light and  $k_B$  is Boltzmann's constant. This equation also holds if the light wave frequency is used instead of the wavelength, with the monochromatic flux  $F_{\nu,bb}$  now being the black body flux per unit frequency per unit angular viewing area:

$$F_{\nu,bb} = \frac{2h\nu^3}{c^2 \left( \exp \left( \frac{h\nu}{k_B T} \right) - 1 \right)} \quad (1.10)$$

In this project, the definition of monochromatic flux for any given object will be reserved exclusively for the flux per unit wavelength,  $F_{\lambda}$ , with any calculations involving black body fluxes using Equation 1.9.

The general approximation of stars to black bodies (and hence the actual stellar surface temperature to  $T_{\text{eff}}$ ) is valid because all stars have been observed to have spectra that closely resemble those of black bodies, with the notable exception of atmospheric absorption lines. The (intrinsic) bolometric luminosity of a star is used to define the effective temperature via:

$$L = 4\pi R^2 \sigma_{SB} T_{\text{eff}}^4 \quad (1.11)$$

where  $R$  is the (mean) stellar radius. Effective temperature has an effect on interstellar extinction due to its strong effect on the stellar luminosity and, hence, the flux, via the Planck Law in Equation 1.9. For a higher effective temperature, as demonstrated in Figure 1.3, there will be more photons in the broad beam of light with wavelengths that make them likely to interact with the local ISM.

## Metallicity

The atmosphere of any given star always contains a variety of chemical species, depending on the overall composition of the star, which is quantified by the stellar metallicity. These different chemical species each have different orbital configurations of atomic/ionic electron states. Each electron state absorbs and emits photons at a particular wavelength, which varies between individual states and between different atoms. Although the light absorbed by an atomic electron is re-radiated, over a large number of electrons this radiation is emitted isotropically, causing a net decrease in the flux travelling out of the stellar atmosphere in the direction of a given observer at that wavelength. Therefore, in a given wavelength range, such as that defining a particular photometric filter, a greater proportion of light in a broadband beam is absorbed in a

medium containing a mixture of many different elements than in a medium dominated by one or two elements.

From observations, it is clear that hydrogen is the most abundant element in stellar atmospheres, with helium a clear-but-distant second. The metallicity of a star is defined as the fractional abundance of heavy elements, often approximated by iron (Fe) alone, relative to the star's hydrogen (H) abundance, compared to that of the Sun. The abundances are determined by the strength of the elements' characteristic atomic absorption lines in the stellar spectra, and the metallicity itself is defined via the following equation:

$$[\text{Fe}/\text{H}] = \log \left( \frac{N_{\text{Fe}}}{N_{\text{H}}} \right) - \log \left( \frac{N_{\text{Fe},\odot}}{N_{\text{H},\odot}} \right) \quad (1.12)$$

where  $N_E$  represents the number density for a generic atomic species  $E$ . For stellar observations,  $N_E$  is measured at the surface. Since the output of Equation 1.12 is logarithmic, a value of  $[\text{Fe}/\text{H}] = 0$  indicates solar metallicity. An increase in metallicity would cause the relevant metallic absorption lines to be stronger, thus reducing the observable flux. An increased metallicity also implies an increase in abundance of sub-ferrous metals. The presence of more nuclear species, each with unique absorption line configurations, inevitably creates more observable lines, further increasing the apparent extinction in the spectral flux. The effect of this reduction in flux manifests itself as a reduction in the stellar luminosity and therefore the effective temperature when all other stellar properties (such as the mass and age) are fixed.

### Surface gravity

The definition of the stellar surface gravity  $g$  is simply the value of the standard Newtonian gravitational acceleration, applied to the stellar surface (the mass is the total stellar mass,  $M$ , and the distance is the stellar radius,  $R$ ):

$$g = \frac{GM}{R^2} = \frac{4\pi G \int_0^R \rho(r)r^2 dr}{R^2} \quad (1.13)$$

A greater surface gravity, as can be inferred from Equation 1.13, represents a surface with a higher mass density. For stars, being self-gravitating, this infers a higher atomic number density.

The effects of surface gravity on the stellar emission spectrum arise directly from the quantum mechanical properties of the interactions between the photons and atomic electrons in the stellar atmosphere. While stellar spectral lines are always broadened due to the Heisenberg uncertainty principle (an effect known as “natural broadening”), they can be broadened further by additional effects arising from the proximity (i.e. number density) of particles at the stellar surface, which is described by the strength

of the stellar surface gravity.

The impact of stellar effective temperature, metallicity and surface gravity on extinction arises through their described effect on the spectral energy distribution (SED) emitted by the stellar atmosphere. Since both the SED and the magnitude of the interstellar extinction are functions of wavelength, different stellar types, with different SEDs, can be impacted to different extents by interstellar extinction at a given wavelength.

## 1.2.2 Determining properties of stellar populations

### The role of CMDs

If we compare the individual black body spectra in Figure 1.3, it can be seen that the maximum monochromatic flux of the black body occurs at an increasingly shorter wavelength for objects with increasingly higher temperatures, as indicated by the green curve connecting the  $F_{\lambda,bb}$  maxima at different temperatures. This makes the object appear bluer to an observer. The relationship between the wavelength at which the monochromatic flux is maximal ( $\lambda_{max}$ ) and the black body temperature is quantified by Wien's displacement law:

$$\lambda_{max}T = 2.898 \times 10^6 \text{ nm K} \quad (1.14)$$

More importantly, Figure 1.3 demonstrates that, within the UV-to-IR wavelength regime, the change in monochromatic flux between values at two different wavelengths is always greater for stars with higher effective temperatures. Therefore, to measure a star's effective temperature, observers compare the star's observed flux in two filters operating at different wavelengths within this range. The difference between the star's flux magnitudes in each of the two filters is then taken, with the magnitude for the redder filter being deducted from that of the bluer filter. This quantity is known as the colour index. For two filters  $X$  and  $Y$ , with  $X$  being bluer than  $Y$ , the colour index of observations made using those filters,  $(X - Y)$ , is defined as:

$$\begin{aligned} (X - Y) &= m_X - m_Y \\ &= (m_{X,0} - m_{Y,0}) + (A_X - A_Y) \\ &= (X - Y)_0 + E(X - Y) \end{aligned} \quad (1.15)$$

where  $(X - Y)_0$  is the true or intrinsic colour index of the object,  $m_{X,0}$  and  $m_{Y,0}$  are the object's intrinsic apparent magnitudes in  $X$  and  $Y$ , respectively, and  $E(X - Y) = A_X - A_Y$  is known as the colour excess, but can also be denoted in literature using the term "reddening". The colour excess represents the effect of extinction on the observed colour index. Its importance arises from the prominence of the intrinsic colour index in determining effective temperature. Higher values of  $(X - Y)$  indicate redder stars,

with lower effective temperatures.

The most commonly-used colour index, employed as a reference for most optical observations, is the Johnson  $(B - V)$  index (Johnson & Morgan, 1953). This is due to these filters being the among most widely used and best-studied available, allowing for better comparisons of different data, including data from older archives.

It can be seen from Equation 1.11 that the luminosity (and therefore flux) of a star is dependent on radius as well as effective temperature. If a plot is made of luminosity against effective temperature (a Hertzsprung-Russell diagram), it can be seen that all stars in a given star cluster follow a single, complex track. Because the stars are approximately the same age in a typical cluster population, this track is known as an isochrone. Isochrones for different population ages and metallicities are calculated using theoretical stellar models, which cover the largest possible spread of initial stellar masses for the required age.

By examining the flux-magnitude equations from both this section and Section 1.1, it becomes clear that both the absolute filter magnitudes and the intrinsic colour indices can be combined with bolometric corrections to calculate the bolometric stellar luminosity  $L$  from observational data. To determine the detailed properties of stellar populations, all stars in an observational sample or star cluster are plotted together on a pair of axes known as a colour-magnitude diagram (CMD), which represents an observational analogue of the HR diagram (Bessell, 2005). The absolute magnitude of stars in a given filter  $Z$ ,  $M_Z$ , is on the vertical axis, with the flux increasing (and the magnitude value decreasing) upwards. The intrinsic colour index of the stars in two filters  $X$  and  $Y$ ,  $(X - Y)_0$ , is on the x-axis, with the values increasing (and stars becoming redder) to the right. Note that filter  $Z$  may be the same as either  $X$  or  $Y$ .

In practice, the universal general shape and position of stellar populations in the HR diagram and each observational CMD, particularly the position and shape of the main sequence, provides a highly useful tool for comparing stellar populations with unknown distances and extinction values to known examples and to theoretical models. This is done by alignment of the respective main sequences in CMDs, particularly the upper main sequence below the MSTO position, which contains the most luminous MS stars and is less sensitive to the (initially unknown) value of the cluster metallicity than the lower MS.

The age of an observed stellar population is determined by, firstly, correcting the data for the effects of distance and extinction and, secondly, aligning a series of isochrones, each of a different age, with the main-sequence (MS) of the observed data. The accepted age of the population is that of the isochrone which most closely follows the progression of stars along the main-sequence turn-off (MSTO). As such, any errors in the estimated extinction can potentially change the age of the best-fit isochrone and

therefore produce an erroneous estimate of the true population age.

### Comparing theoretical and observational quantities

For any observational dataset of stars, the stars' individual extinction values will be completely unknown from the data alone. In order to compare observational and theoretical data, the most convenient approach is to add the (theoretical) extinction value(s) to the theoretical dataset magnitudes (i.e., absolute magnitudes), before comparing to the distance-corrected observational data. As a result, the quantity from each dataset that is being compared is the absolute magnitude plus the extinction in each filter. If we label this quantity  $M_{\text{ext},X}$  for a generic filter  $X$ , we can define it as:

$$M_{\text{ext},X} = M_X + A_X \quad (1.16)$$

Using Equation 1.1, Equation 1.16 can now be rewritten such that  $M_{\text{ext},X}$  can be defined using both quantities derived directly from observations and those determined by theoretical models:

$$\begin{aligned} M_{\text{ext},X} &= M_X + A_X \text{ (theoretical data)} \\ &= m_X + 5 - 5 \log \left( \frac{d}{\text{pc}} \right) \text{ (observational data)} \end{aligned} \quad (1.17)$$

This allows for direct comparison of theoretical data, whose stars are treated with theoretically-determined  $A_X$  values, with distance-corrected observational data, whose stars have unknown  $A_X$  values. Equation 1.17 therefore provides a pathway for comparing the standard treatment of extinction (constant  $A_X/A_V$  ratios) with the treatment proposed in this project ( $A_X/A_V$  varying as functions of intrinsic stellar parameters). In practice, therefore, due to the unknown extinction values for the individual stars and the cluster as a whole, the axis parameters for the generic CMD in Section 1.2.2 are  $M_{\text{ext},Z}$  and  $(X - Y)$ , instead of  $M_Z$  and  $(X - Y)_0$ , respectively.

## 1.3 The standard treatment of extinction in observed stellar populations

In observations, the extinction for a given source is initially unknown. For a stellar population, observers must make use of distinctive features of stellar populations that can be used as standard candles to estimate the distance to the population, allowing the extinction to then be calculated.

The value used for the extinction ratio  $A_X/A_V$  in the standard treatment is often taken from Rieke & Lebofsky (1985). This approach has the issue of assuming that



$A_X/A_V$  is constant for all stars in a given stellar population, meaning the fraction of flux lost between the stellar surface and the observer for any beam in the wavelength range of  $X$  is always directly proportional to the fraction lost in the  $V$  band for all stars. This results in  $A_X/A_V$  values that do not account for variations between spectra of different stellar classes, which is shown to be inaccurate in the data shown in Figures 2.7 and 2.8 in Section 2.1.

Girardi et al. (2008) produced data tables of  $A_X/A_V$  for stellar atmosphere models with parameters  $T_{\text{eff}}$ ,  $\log(g)$  and  $[\text{Fe}/\text{H}]$ . They carried this out using the same ATLAS9 data (Castelli & Kurucz, 2004) that was used to generate the data for this project, but also combined it with data from other studies, which are listed in Girardi et al. (2002), resulting in data covering a parameter space extending beyond the ATLAS9 limits in all three parameters. They used the data tables to calculate the  $A_X/A_V$  values for the stellar models in Padova theoretical isochrones (Bertelli et al., 1994). While determining that the values of  $A_X/A_V$  varied significantly with  $T_{\text{eff}}$  and  $\log(g)$ , the variation with metallicity was found to be  $\sim 0.17\%$  between  $[\text{Fe}/\text{H}] = 0.0$  and  $[\text{Fe}/\text{H}] = -2.5$ . They found that, when they set  $A_V = 6$ , there was a systematic shift for the ACS filter system between extinction values calculated star-wise using the tables of  $A_X/A_V$  data and a constant extinction value applied to the entire isochrone. The constant values of  $A_X/A_V$  were calculated from a yellow dwarf in the low-extinction regime. Overall, in the single ACS CMD example shown in the study, the  $A_X/A_V$  tables produced a smaller extinction value in the F814W filter and a larger (F475W-F814W) colour index value. It also caused a change in the shape of the curve at the main-sequence turn-off (MSTO) point. They then applied the data from the tables to the case of the globular cluster M92. They found the optimal metallicity to be  $Z = 0.0004$  ( $[\text{Fe}/\text{H}] \approx -1.6$ ) instead of the value obtained by previous observers of  $Z = 0.0001$  ( $[\text{Fe}/\text{H}] \approx -2.2$ ). Therefore, their use of  $A_X/A_V$  data caused the estimated cluster metallicity to be greater than when using the standard one-size-fits-all approach to extinction.

Ortolani et al. (2017) used the tabulated extinction ratio tables resulting from Girardi et al. (2008), which demonstrated the effect of stellar parameters on the calculated extinction ratios, to search for potential discrepancies in the predicted ages of isochrones after the addition of extinction. This was performed for isochrones with real ages between 12 and 13 Gyr and employed a small selection of Johnson ( $B$ ,  $V$  and  $I$ ) and ACS (F606W, F775W and F814W) broadband filters. They found that, by employing the Girardi et al. (2008) data, the position of isochrone in the CMD shifted such that, at  $A_V = 1$ , the position of the MSTO of a 12 Gyr isochrone with individual stellar extinction values added is the same as the MSTO position for a 12.5 Gyr isochrone with the standard fixed extinction value added.

## 1.4 Project objective

The first goal of this project is to investigate the variations of the extinction ratios  $A_X/A_V$  in selected photometric filters within multiple filter systems with changes in effective temperature, surface gravity and metallicity. This will be carried out using a large library of theoretical stellar spectra covering all main stages of stellar evolution. Analytic fitting functions will be employed to model the  $A_X/A_V$  variations in each filter as a function of the stellar parameters.

The results of the fitting process will then be applied to the CMD of a representative observational example of a relatively high-extinction open cluster. The CMD will be fitted with two theoretical isochrones. For the first case, a constant  $A_X/A_V$  value will be applied to the entire isochrone. For the second, varying  $A_X/A_V$  values will be applied, using the fitting results. The best estimates for the ages and  $A_V$  values in both cases will be compared, giving a quantitative illustration of the importance of the effect of the stellar parameters on  $A_X/A_V$  ratios used in CMD fitting.

# Chapter 2

## Data & methodology

### 2.1 Calculating extinction ratio data

When observing stars through a photometric filter, only a small fraction of the bolometric stellar flux that reaches the telescope is detected, since stars emit photons with wavelengths across the full EM spectrum. This is due to the design of the filter in question, which determines the fraction of photons detected at a given wavelength, known as the transmittance. The variation in transmittance as a function of photon wavelength is known as a transmission curve, bandpass or filter response function. Examples of filter response functions for the photometric systems are given in Figures 2.3-2.6. It is clear that the range of wavelengths for which the transmittance is non-zero, for any filter, is very narrow when compared to the full EM spectral range.

The significance of this relatively narrow wavelength range occurs when analysing observational data using the results of theoretical stellar models, which determine the state of a stellar evolution model at a specified age, in the form of isochrones. In this project, isochrones are the central tool to compare the effects of using variable and fixed extinction ratios on the estimated age of star clusters. The results of theoretical evolutionary models are expressed in terms of a star's bolometric quantities, such as the bolometric luminosity, the effective temperature and the metallicity, which in turn can be used to calculate further important quantities, such as the stellar radius (via Equation 1.11) and surface gravity (via Equation 1.13). Therefore, to correctly compare theoretical models and isochrones, which use bolometric data, to observational photometric data, by necessity limited by the use of filters, mathematical methods must be used to transform the theoretical stellar evolution model data into the form of filter-based fluxes and magnitudes.

### 2.1.1 The role of stellar evolution and atmosphere models

The first step in this transformation is to compute theoretical stellar spectra. This is done using stellar atmosphere models, which use values of  $T_{\text{eff}}$ ,  $\log(g)$  and  $[\text{Fe}/\text{H}]$ , taken from the appropriate stellar evolution models, as a basis to produce a theoretical emission spectrum for that star, in the form of a table showing a list of desired wavelengths  $\lambda$  and the theoretical monochromatic flux at that wavelength,  $F_\lambda$ , defined at the atmospheric/stellar radius,  $R$ . To apply the spectrum to the case of a distant observer, the equation linking the relevant flux definitions to the observer distance,  $d$ , must be included:

$$f_\lambda d^2 = F_\lambda R^2 \quad (2.1)$$

where  $f_\lambda$  represents the (theoretical) monochromatic flux at a given wavelength  $\lambda$  at the observer's distance from the source. However, as with all flux magnitudes, the predicted apparent magnitude for a distant star, with unknown extinction, must be linked to a known reference point. This requires the detailed knowledge of a reference spectrum, of a nearby star which is unlikely to experience significant extinction. For all filter systems studied in this project, the nearby bright star Vega ( $\alpha$  Lyr) was used as the reference object. Using Vega as the reference star is the most well-known approach to photometric calibration (Casagrande & Vandenberg, 2014), not only due to its high apparent brightness and close proximity to Earth, but also due to its spectral classification as an A0 star, which should theoretically have an apparent magnitude  $m_X = 0$  in any given filter.

After accounting for the effect of interstellar extinction on an object's detected flux, its apparent magnitude in the wavelength range of a generic filter  $X$ , defined as increasing from the shortest ( $\lambda_1$ ) to the longest ( $\lambda_2$ ) wavelength for which its response function is non-zero, can be calculated in terms of parameters determined theoretically by both stellar evolution and atmosphere models:

$$m_X = -2.5 \log_{10} \left( \frac{\int_{\lambda_1}^{\lambda_2} f_\lambda (10^{-0.4A_\lambda}) S_\lambda d\lambda}{\int_{\lambda_1}^{\lambda_2} f_\lambda^0 S_\lambda d\lambda} \right) + m_X^0 \quad (2.2)$$

where  $A_\lambda$  is the extinction as a function of wavelength (see Equation 2.7 later for calculation of values from the Cardelli et al. (1989) extinction law),  $S_\lambda$  represents the filter response function of  $X$  and  $f_\lambda^0$  and  $m_X^0$  represent the monochromatic flux and apparent magnitude, respectively, in  $X$  of Vega. The use of these two well-determined observational parameters allows the remaining terms to be fixed to a known scale.

### 2.1.2 Bolometric corrections

For an observed star at an unknown distance  $d$ , Equation 2.1 cannot give the magnitude of the theoretical spectrum at the observer distance,  $f_\lambda$  with any reasonable

certainty. The uncertainty in  $f_\lambda$  then causes uncertainty regarding the extinction  $A_\lambda$  given its position in the same integrand in Equation 2.2.

Stellar evolution models, such as the BaSTI model used in this project, offer predictions for the values of bolometric stellar parameters, such as the luminosity, effective temperature, radius and surface isotope abundances, for as many stellar models as possible, whose results are stored in databases. This makes these evolution models very useful both as a basis for stellar atmosphere models and for generating isochrones, meaning they are very useful for studying star clusters, whose members are generally born around the same time. However, the bolometric stellar properties generated by the evolutionary models are not described as functions of wavelength, making them useless for the integration terms in Equation 2.1. Equation 2.1 does, however, have great value via the inclusion of the well-constrained observed Vega quantities, which provide a necessary reference for interpreting newly-observed stars. Therefore, the uncertainty arising from  $f_\lambda$  must be eliminated by linking predicted quantities from theoretical stellar evolution models to observed quantities. The bolometric data from the theoretical models must be converted into filter-based quantities in order to compare theoretical predictions with observational data (Flower, 1996), thereby supplying information about the observed stars that cannot be determined from the observations alone (Girardi et al., 2002) and allowing predictions to be made about those stars. The bolometric correction is the quantity which determines this conversion. To make use of bolometric corrections, the absolute magnitude,  $M_X$ , of the star in filter  $X$  must be calculated. This can be done using the apparent magnitude standard equation which links the two quantities:

$$M_X = m_X - 2.5 \log_{10} \left( \left( \frac{d}{10 \text{pc}} \right)^2 \right), \quad (2.3)$$

This represents the second step required for the comparison of theoretical isochrones to the observational case, and requires the calculation of bolometric corrections.

To derive the equation linking a bolometric correction with the extinction, we start with the definition of a bolometric correction for filter  $X$ , which is denoted by  $BC_X$ :

$$BC_X \equiv M_{\text{bol}} - M_X \quad (2.4)$$

where  $M_{\text{bol}}$  is its (predicted) absolute bolometric magnitude, defined relative to the Sun using:

$$M_{\text{bol}} = M_{\text{bol},\odot} - 2.5 \log_{10} \left( \frac{4\pi R^2 F_{\text{bol}}}{L_\odot} \right) \quad (2.5)$$

where  $M_{\text{bol},\odot}$  is the solar absolute bolometric magnitude, which is assumed in this work to have a value of 4.75,  $L_\odot$  is the solar luminosity, for which a value of  $3.844 \times 10^{33} \text{ erg s}^{-1}$  is used, and  $F_{\text{bol}}$  is the bolometric flux at the stellar surface. It should be noted

that  $F_{\text{bol}} = \sigma_{\text{SB}} T_{\text{eff}}^4$  and therefore  $4\pi R^2 F_{\text{bol}}$  is simply equal to the bolometric stellar luminosity  $L$ , and is therefore determined solely by the theoretical stellar model used. The bolometric correction for filter  $X$  can therefore be expressed, via Equations 2.2-2.5, purely in terms of extinction, theoretical stellar quantities independent of distance and observationally well-constrained reference parameters:

$$BC_X = M_{\text{bol},\odot} - m_X^0 - 2.5 \log_{10} \left( \frac{4\pi R^2 F_{\text{bol}}}{L_{\odot}} \right) + 2.5 \log_{10} \left( \frac{\int_{\lambda_1}^{\lambda_2} F_{\lambda} (10^{-0.4A_{\lambda}}) S_{\lambda} d\lambda}{\int_{\lambda_1}^{\lambda_2} f_{\lambda}^0 S_{\lambda} d\lambda} \right) \quad (2.6)$$

The output value of Equation 2.6 therefore varies with changes in the effective temperature, surface gravity and metallicity of the stellar atmosphere model, via  $R$ ,  $F_{\lambda}$  and  $F_{\text{bol}}$ , and the extinction  $A_{\lambda}$ .  $A_{\lambda}$  is usually parametrised relative to the extinction in the well-studied Johnson- $V$  filter,  $A_V$ . To extract  $A_{\lambda}$ , we use the simple relation:

$$A_{\lambda} = \left( \frac{A_{\lambda}}{A_V} \right) A_V \quad (2.7)$$

together with the Cardelli et al. (1989) extinction law for  $A_{\lambda}/A_V$ , which is monochromatic and therefore must be placed within the integrand of Equation 2.6. Given that the Cardelli et al. (1989) extinction law is normalised to  $A_V$ , the value of  $A_V$  must be specified prior to the calculation of the bolometric correction. Equation 2.6 was implemented twice, once for each of two distinct  $A_V$  values (for this project these were  $A_V = 0, 1$ ). It should be noted that  $BC_X(A_V = 0)$  essentially assumes no extinction in any filter. Therefore, two output values were calculated for Equation 2.6, one for each  $A_V$  value. The difference between these two outputs was then taken to extract the extinction ratio  $A_X/A_V$ , via the following equation (Girardi et al., 2008):

$$(A_X/A_V) A_V = BC_X(0) - BC_X(A_V) \equiv m_{X,0} - m_X(A_V) \quad (2.8)$$

Any dependence of the  $A_X/A_V$  data on the measurements for Vega or the Sun from Equation 2.6 is eliminated during the subtraction, as these terms are unaffected by the  $A_{\lambda}$  value. However, effects due to the nature of the atmosphere of the stellar source on the extinction ratio will remain present, in the form of the integrations of  $F_{\lambda} S_{\lambda}$  and  $F_{\lambda} S_{\lambda} \times (10^{-0.4A_{\lambda}})$ , respectively, in the two bolometric correction terms in Equation 2.8.

### Comparison with colour corrections

It is important to note that a bolometric correction is different from the equally well-known quantity known as a colour correction. Colour corrections are tools to determine

the true apparent magnitudes and colours of stars which are observed through a particular set of filters from the magnitudes recorded by the instrument. Observations made using a particular filters are described using the filter’s effective wavelength  $\lambda_{\text{eff}}$ , defined as an average over the filter wavelength interval, weighted by the source spectrum and the filter response function:

$$\lambda_{\text{eff}} = \frac{\int_{\lambda_1}^{\lambda_2} \lambda f_{\lambda} S_{\lambda} d\lambda}{\int_{\lambda_1}^{\lambda_2} f_{\lambda} S_{\lambda} d\lambda} \quad (2.9)$$

where all terms take the same definitions as in Equation 2.2. However, with the source stellar spectrum initially unknown, in practice the observed stellar spectrum is calculated using a single fixed wavelength value for the whole filter, known as the reference wavelength,  $\lambda_{\text{ref}}$  (Pajot et al., 2006), instead of the effective wavelength. This does not match with the definition of  $\lambda_{\text{eff}}$  in Equation 2.9, however. In the equation, the integrand in the numerator is a product of both the wavelength and monochromatic flux. This means that the shape of the observed spectrum within the filter wavelength range also has an impact on the final filter  $\lambda_{\text{eff}}$ , and so the real value of  $\lambda_{\text{eff}}$  is weighted by the flux of the source itself,  $f_{\lambda}$ . This causes a significant issue due to the fact that for different types of stars, the effective wavelength of the same filter is different (Beichman et al., 1988), while in practice, the fixed filter  $\lambda_{\text{ref}}$  value must be used due to the influence of the (unknown) source spectrum on the effective wavelength.

This mismatch between  $\lambda_{\text{eff}}$  and  $\lambda_{\text{ref}}$  must be compensated for, in order to obtain the true source spectrum. This is done by multiplying the observed spectral flux by a calibration factor known as the “colour correction”. The size of this correction factor is different for different filters, as they occupy different wavelength regions and therefore experience different weights when calculating the true  $\lambda_{\text{eff}}$ . Different source spectra also produce different colour corrections, as can be seen by their impact on  $\lambda_{\text{eff}}$  in Equation 2.9. To determine the correction factors for sources observed through the filter in question, well-tested synthetic spectra must be used, as these are free of any potential observational bias. To simulate emission from stars and interstellar dust, quasi-black body or “grey body” spectra are used, whose behaviour is defined by a Planck function (see Equation 1.9) multiplied by a power-law wavelength term ( $\lambda^{-\alpha}$ ), and are therefore governed by the effective temperature of the Planck function and the value of the power-law index  $\alpha$ . Examples of tables of colour correction factors, with the values of  $T_{\text{eff}}$  and  $\alpha$  for the associated spectra, can be found in Table Suppl.VI.C.6 of Beichman et al. (1988) and Table 2 of Pajot et al. (2006).

This stands in contrast with bolometric corrections, which link two predicted bolometric absolute magnitudes, one bolometric and the other specific to a given filter response function. The two  $A_X/A_V$  treatment methods are not impacted by this effect. The stellar spectra used for the FBER approach are generated directly from known theoretical model atmospheres before encountering either the filter response function or the Cardelli et al. (1989) extinction law in Equations 2.2 and 2.6. The extinction ratio

values selected for the fixed-extinction ratio case are selected from the same database used by the FBER models, and so are also unaffected.

### 2.1.3 Choice of $R_V$ and $A_V$ values

In order to generate tables of bolometric corrections, the relevant software required the user to input a single, global value for the parameters  $R_V$  and  $A_V$ . The global  $R_V$  value, which is applied to the Cardelli et al. (1989) monochromatic extinction law, was chosen as  $R_V = 3.1$ . This is equal to the mean diffuse ISM value calculated by Rieke & Lebofsky (1985) and widely used in analysis of stellar observations. The choice for the non-zero value of  $A_V$  was required in order to generate the  $A_X/A_V$  data via Equation 2.8. The choice for this global value was made as  $A_V = 1.0$ . This value was chosen for multiple reasons.

Firstly, a value of  $A_V = 1.0$  is sufficiently large for differences between both BC datasets to become apparent in the  $A_X/A_V$  data calculated from Equation 2.8, which makes it more practical for training extinction ratio models.

#### Forbes effect

A value of  $A_V = 1.0$  is also sufficiently small for the Forbes effect to have a negligible impact, even for filters with the widest bandwidths. The Forbes effect occurs as a broadband beam of light, such as that emitted by a star, passes through an extended partially-transparent medium, such as the Earth's atmosphere or an interstellar gas or dust cloud. It states that the greater the distance travelled by a light beam through the medium, the more penetrating the beam becomes (Forbes, 1842). The physical basis for this effect is that those photons in the original beam whose wavelengths make them the most likely to be absorbed or refracted are, on average, the earliest to be separated from the beam path as the beam through the medium. Therefore, as the beam travels through the medium, its constituent photons are progressively less likely to be interact with the medium (Grebel & Roberts, 1995). Since a higher fraction of its photons are retained as the distance through the medium increases, the beam is more penetrating (Ohvri et al., 1999).

This has the effect of producing a non-linear increase in extinction for one filter relative to the increase in another (Grebel & Roberts, 1995; Girardi et al., 2008). It should be emphasised that the Forbes effect occurs regardless of the source star's spectral type, and therefore represents an additional source of uncertainty when calculating extinction for highly-reddened stellar populations.

The Forbes effect has an impact on the non-zero  $A_V$  value chosen for Equation 2.8 because if  $R_V$  is held constant at the standard diffuse ISM value of 3.1 (Cardelli et al.,



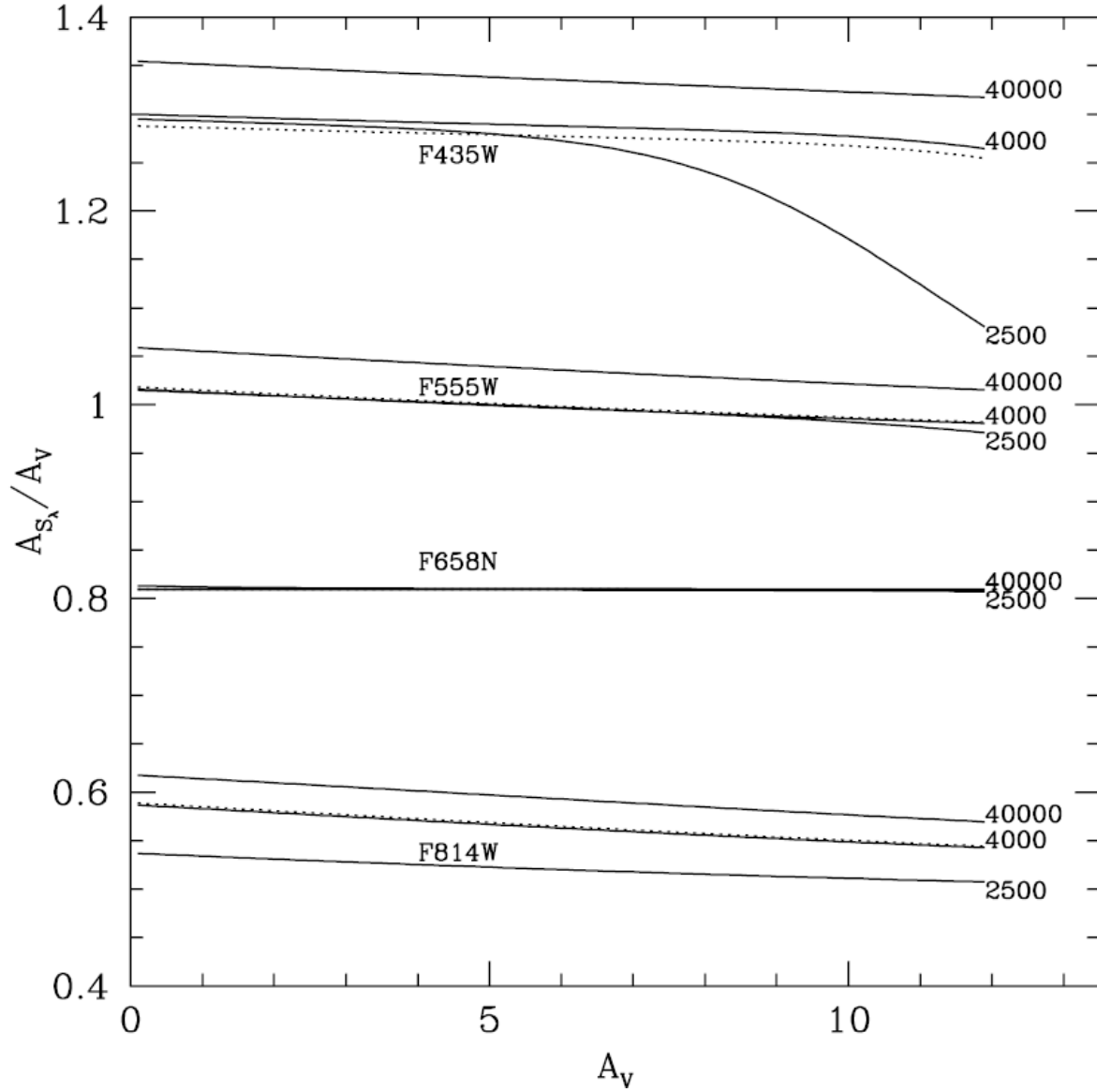


Figure 2.1: Plots of  $A_X/A_V$  for selected ACS filters as functions of the initial  $A_V$  value selected for the calculation of bolometric corrections. Solid lines represent dwarfs ( $\log(g) = 5.0$ ), while dashed lines represent giants, which are defined by the relation  $T_{\text{eff}} = 3250 + 500 \log(g)$  (i.e.  $\log(g)$  is decreasing towards the right side of the plot). The variation of  $A_X/A_V$  with chosen  $A_V$  simulates the strength of the Forbes effect. Source: Girardi et al. (2008)

1989), a larger  $A_V$  value implies a longer path through the ISM, and thus a stronger Forbes effect. According to Girardi et al. (2008), as illustrated in Figure ??, any significant impact from the Forbes effect on the values of  $A_X/A_V$  occurs for a chosen  $A_V \gtrsim 4$ . They found that the effect was particularly strong for stars with  $T_{\text{eff}} \lesssim 3000\text{K}$  and that, unsurprisingly, it became greater as the wavelength range covered by the

filter response function increased.

### Comparison with observed clusters

An  $A_V$  value of 1.0 represents a cluster environment with an overall extinction which is high, but still realistic, when compared to extinction in observed star clusters. This assessment is justified according to the data in Table 2 of Siegel et al. (2019). The  $A_V$  in that table were obtained by multiplying the  $E_{B-V}$  values by an  $R_V$  value of 3.1, as was assumed for the synthetic data in this project. This assumption as applied to the table is justified on the basis that, with only a small number of exceptions, the clusters were assessed as obeying the Milky Way law for extinction as a function of wavelength, which is the same as that employed in the seminal extinction-modelling studies, such as Cardelli et al. (1989). As shown in Figure 2.2, out of the 49 open clusters in the table, only 3 have  $A_V$  values greater than 1.0. However, the largest  $A_V$  value calculated was 2.17. This result puts the  $A_V$  value of 1.0 assumed for this project near the midpoint of the total  $A_V$  range covered by the clusters in the Siegel et al. (2019) sample. Therefore, the  $A_V$  value of 1.0 was assessed as realistic in the context of observed star clusters.

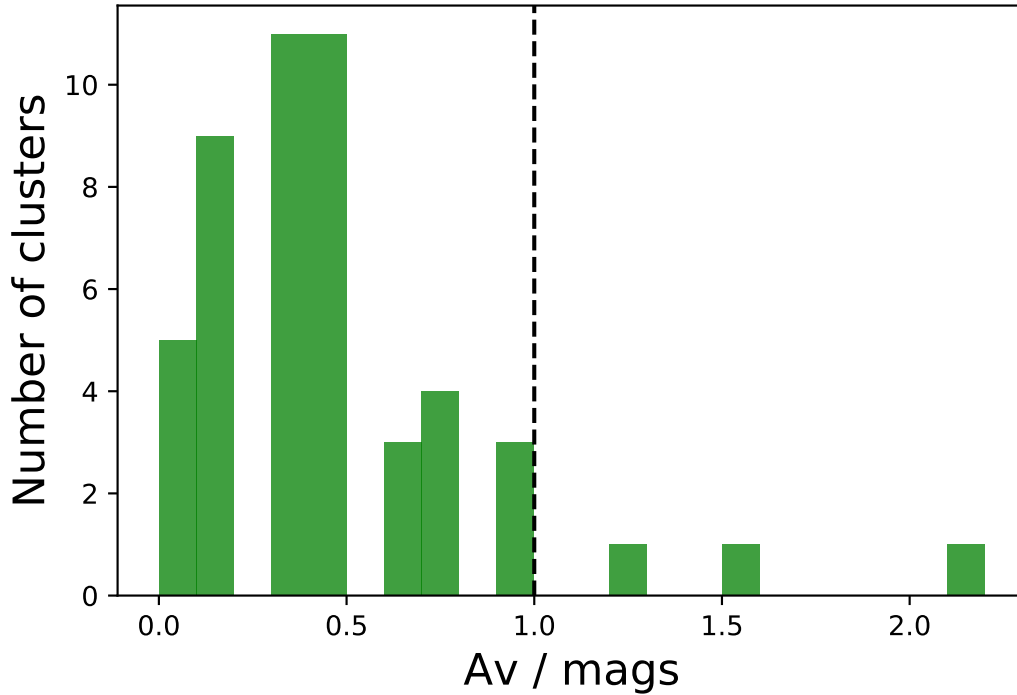


Figure 2.2: Histogram of  $A_V$  values of clusters listed in Table 2 of Siegel et al. (2019). The vertical dashed line at  $A_V = 1.0$  represents the value selected in this project.

## 2.2 Filters studied

In this project, three broad-band filter systems were employed. Two are systems on board the Hubble Space Telescope (HST). These are the Advanced Camera for Surveys (ACS), installed in 2002 on the HST (Sarajedini et al., 2007), and the Ultraviolet Imaging Spectrograph channel of the Wide-Field Camera 3 (WFC3/UVIS), installed on the HST in 2009 (Kalirai et al., 2010; MacKenty et al., 2010). The third is the single set of three broadband filters mounted on the Gaia space observatory (Jordi et al., 2010), launched in 2013.

Examples of response functions for the three filter systems employed in this project are shown in Figures 2.3-2.6. By comparing these with the filters' information in Table 2.1, it can be seen that the exact shape of the response function has a substantial impact on the observed flux, as shown in its contribution to the value of the apparent magnitude in Equation 2.2 and the filter effective wavelength in Equation 2.9, which in turn necessitates the use of colour corrections, as detailed in Section 2.1.2.

Reference will also be made to the Johnson-Morgan UBV filter system (often simply known as the Johnson system) (Johnson & Morgan, 1953), later extended as the Johnson-Cousins UBVRI (Bessell, 1990) system, which has been in use for decades and continues to be the standard reference for more modern filter systems. Of particular importance are the Johnson blue ( $B$ ) and yellow ( $V$ ) filters, as these formed the original benchmark for observing stellar populations and evolutionary stages.

The standard treatment of extinction for isochrones in CMDs is to apply a single constant value of the extinction ratio for a given filter  $X$  to all objects in the isochrone. This quantity is usually expressed as a fixed extinction ratio  $A_X/A_V$  of the (constant) coefficient value in the Johnson- $V$  filter, the standard visual comparison filter. This value is maintained for all stars, regardless of the different effective temperatures, metallicities or surface gravities of the different types of stars present in any given population. The wavelengths of optical light lie between 3800 Å and 7400 Å, with the  $V$  filter having a central wavelength of 5500 Å.

In Table 2.1, all the filters used for this project are listed. The name of each filter is displayed alongside its central wavelength ( $\lambda_{\text{cen}}$ ), full-width at half-maximum (FWHM) and the minimum ( $\lambda_{\text{min}}$ ) and maximum ( $\lambda_{\text{max}}$ ) detection wavelengths. Hence, when combined, these filters cover wavelengths from the soft-ultraviolet (soft-UV) to the near-infrared (NIR), including all visible wavelengths. The FWHM is defined as the difference between the lowest and highest wavelength values at which the transmittance value is half of its maximum value for the filter, typically assuming the response function can be approximated as a Gaussian distribution centred on the central wavelength. The FWHM acts as an approximate measure of the wavelength range within which the filter can be used for observations.

System	Filter	$\lambda_{\text{cen}} / \text{\AA}$	FWHM / $\text{\AA}$	$\lambda_{\text{min}} / \text{\AA}$	$\lambda_{\text{max}} / \text{\AA}$
ACS	F435W	4359	881	3610	4860
	F475W	4781	1403	3863	5563
	F555W	5413	1236	4584	6209
	F606W	5961	2255	4634	7180
	F625W	6323	1390	5446	7100
	F775W	7763	1517	6804	8632
	F814W	8117	2096	6885	9648
WFC3	F218W	2216	329	1990	2603
	F225W	2341	464	1990	2968
	F275W	2696	417	2282	3119
	F300X	2722	660	2137	4098
	F336W	3368	550	3014	3707
	F390W	3929	951	3255	4470
	F438W	4322	674	3895	4710
	F475W	4768	1482	3942	5582
	F555W	5262	1578	4381	7045
	F606W	5941	2298	4700	7204
	F625W	6274	1573	5414	7138
	F775W	7725	1454	6869	8571
	F814W	7814	1505	6978	9684
Gaia	$G$	6631	4397	3321	10515
	$G_{\text{bp}}$	5330	2530	3283	6714
	$G_{\text{rp}}$	7896	2956	6296	10637

Table 2.1: Basic properties of the filters employed in this project. See text for details. Source: <http://svo2.cab.inta-csic.es/svo/theory/fps3/index.php>

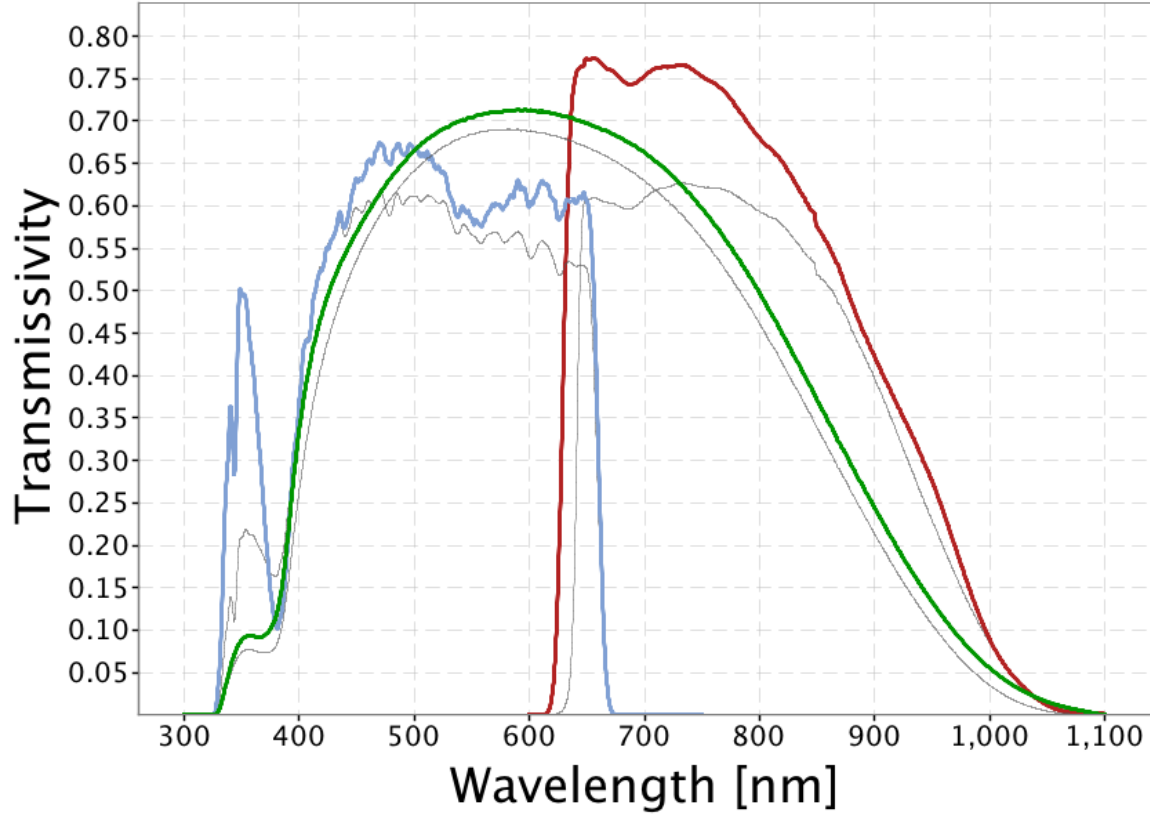


Figure 2.3: Filter response functions for Gaia broadband photometric filters. The three coloured curves show the response functions for the  $G$  (green),  $G_{bp}$  (blue) and  $G_{rp}$  (red) filters as used for Gaia Data Release 2 (DR2). These three DR2 curves were employed for all Gaia-related calculations in this project. The three grey curves show the nominal response functions for the same filters as described in the pre-launch stage by Jordi et al. (2010). These grey curves were used for Gaia DR1 only. Source: [https://www.cosmos.esa.int/web/gaia/iow\\_20180316](https://www.cosmos.esa.int/web/gaia/iow_20180316)

### 2.3 Trends in $A_X/A_V$ data

For all filters described in Section 2.2, the greatest variations in the  $A_X/A_V$  data occur with changes in  $T_{\text{eff}}$ , with changes due to  $\log(g)$  and  $[\text{Fe}/\text{H}]$  being much less significant. This is to be expected, given that the value of  $T_{\text{eff}}$  has a significant effect on the magnitude and shape stellar spectral energy distribution (see Figure 1.3), while the effects of the surface gravity and metallicity are restricted to the absorption lines in the SED. Plots of  $A_X/A_V$  against  $T_{\text{eff}}$  for atmospheres at solar metallicity are presented in Figure 2.7 for the WFC3 and Gaia filters and Figure 2.8 for the ACS filters.

Another general feature is the convergence of  $A_X/A_V$  to a single maximum value in each filter, at  $T_{\text{eff}} = 50,000$  K, for higher effective temperatures, independent of

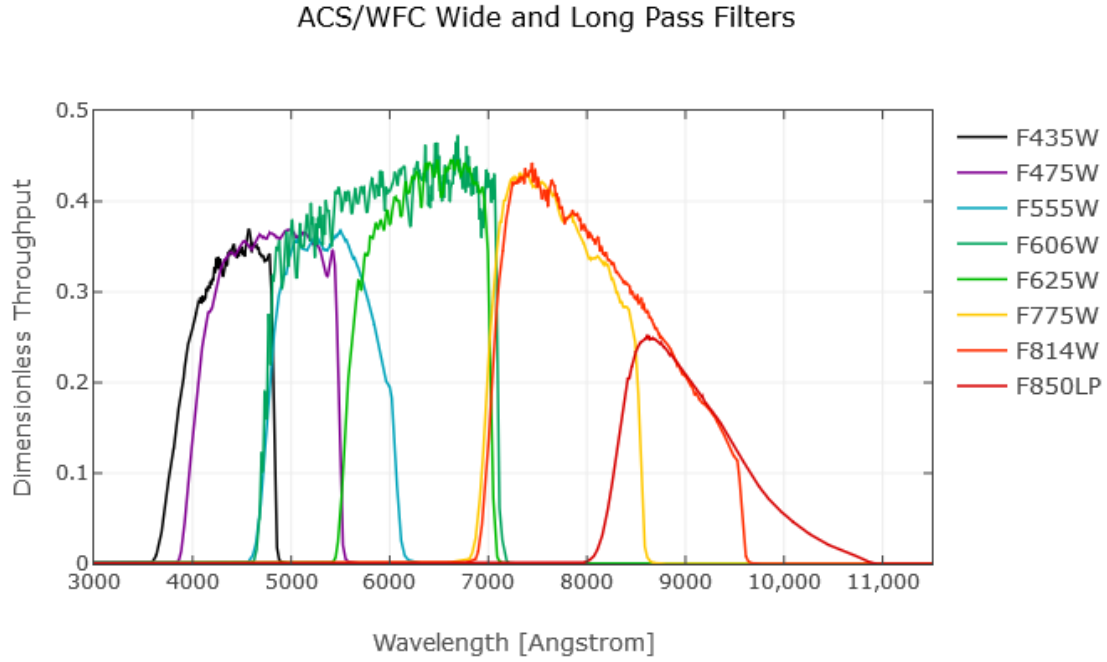


Figure 2.4: Filter response functions for wide-field ACS filters. Source: <http://www.stsci.edu/hst/acs/analysis/throughputs>

metallicity and surface gravity. In most filters, this convergence is achieved to within a margin of 0.01 from the value at  $T_{\text{eff}} = 50,000$  K around temperatures of 20,000 K. The region of parameter space in  $T_{\text{eff}}$ ,  $\log(g)$  and  $[\text{Fe}/\text{H}]$  characterised as having achieved this convergence will be referred to henceforth as the “high- $T_{\text{eff}}$  plateau region” or simply “plateau”.

In general, the values of  $A_X/A_V$  for a given stellar atmosphere increase as the central wavelength of the filter decreases, reflecting the greater extinction effect of the ISM dust in the UV and optically blue spectral regions, as detailed in Section 1.1.1. This can be seen by looking at the scales on the y-axes of the respective sub-plots in Figures 2.7 and 2.8. The UV filters host both the highest plateau  $A_X/A_V$  values and the greatest range in  $A_X/A_V$  between the plateau  $T_{\text{eff}}$  region and that with the coolest atmospheres.

A property found in the data for some filters, which becomes more pronounced at higher stellar metallicities, is the tendency of the gradient of  $A_X/A_V$  with increasing  $T_{\text{eff}}$  to become significantly less positive at the lowest temperatures in the data, typically around 4000K and below. The spread in  $A_X/A_V$  values for different  $\log(g)$  is typically about 0.02-0.04, with a linear progression from  $\log(g) = 5.0$  at the lowest

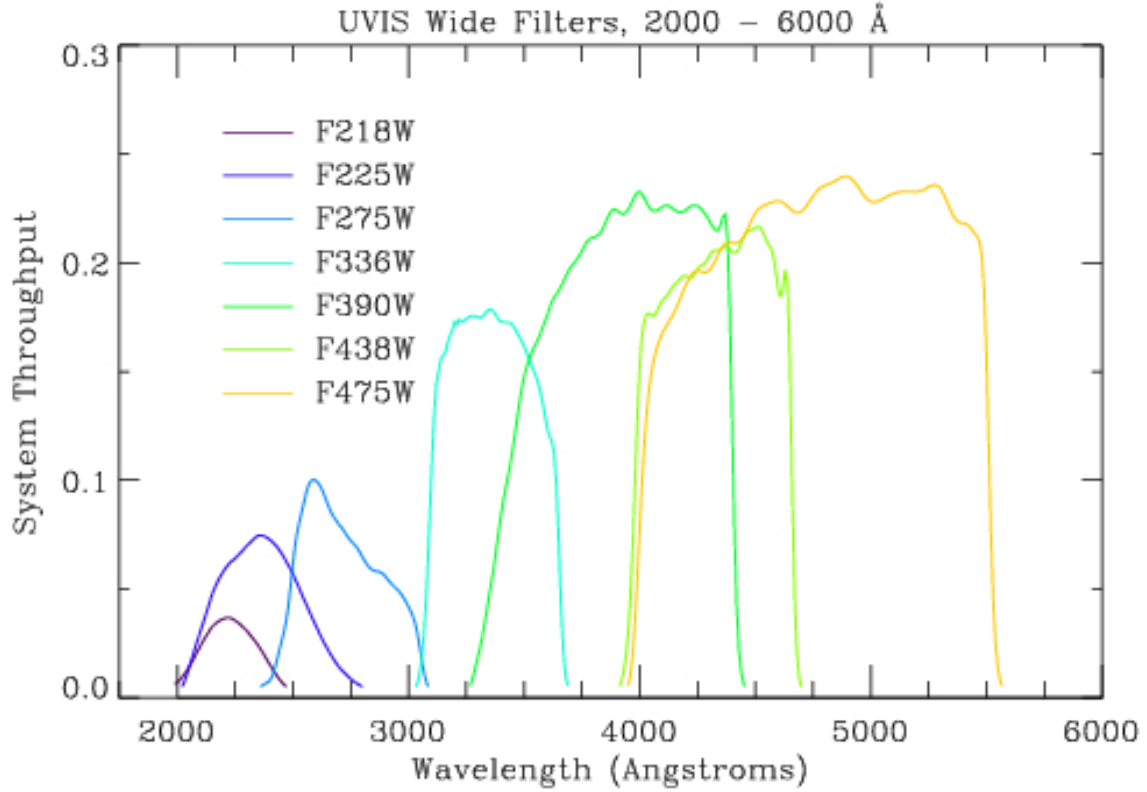


Figure 2.5: Filter response functions for wide-field WFC3 filters. Source: [http://www.stsci.edu/hst/wfc3/ins\\_performance/throughputs/UVIS\\_filterthru.html](http://www.stsci.edu/hst/wfc3/ins_performance/throughputs/UVIS_filterthru.html)

end to  $\log(g) = 0.0$  at the highest. In some filters, at the highest metallicity employed ( $[\text{Fe}/\text{H}] = 0.5$ ), this phenomenon causes the gradient to invert and become significantly negative, reversing the trend everywhere else in the data, including for the same filters at lower metallicity. Due to the shape of the resulting point-to-point line in these axes, as plotted in both Figures 2.7 and 2.8, it has been dubbed the “tail-flick” phenomenon. In the same figures, the phenomenon is particularly prominent in the plots for the ACS F435W, WFC3 F438W, F475W (both WFC3 and ACS) and Gaia  $G_{\text{bp}}$  filters.

This gradient inversion was treated as an artefact of non-physical origin caused by the known significant uncertainties in ATLAS9 at effective temperatures below 4500K (Castelli & Kurucz, 2004; Girardi et al., 2008). Furthermore, the spread in  $A_X/A_V$  at low  $T_{\text{eff}}$  values due to the tail-flick phenomenon is sufficiently small relative to the  $A_X/A_V$  values at low effective temperatures in every relevant filter to be insignificant in terms of the final effect of extinction on the CMD positions of isochrones. As a result, only data for atmospheres with effective temperatures above those affected by the gradient inversion was used by the algorithm to fit the coefficients of the chosen

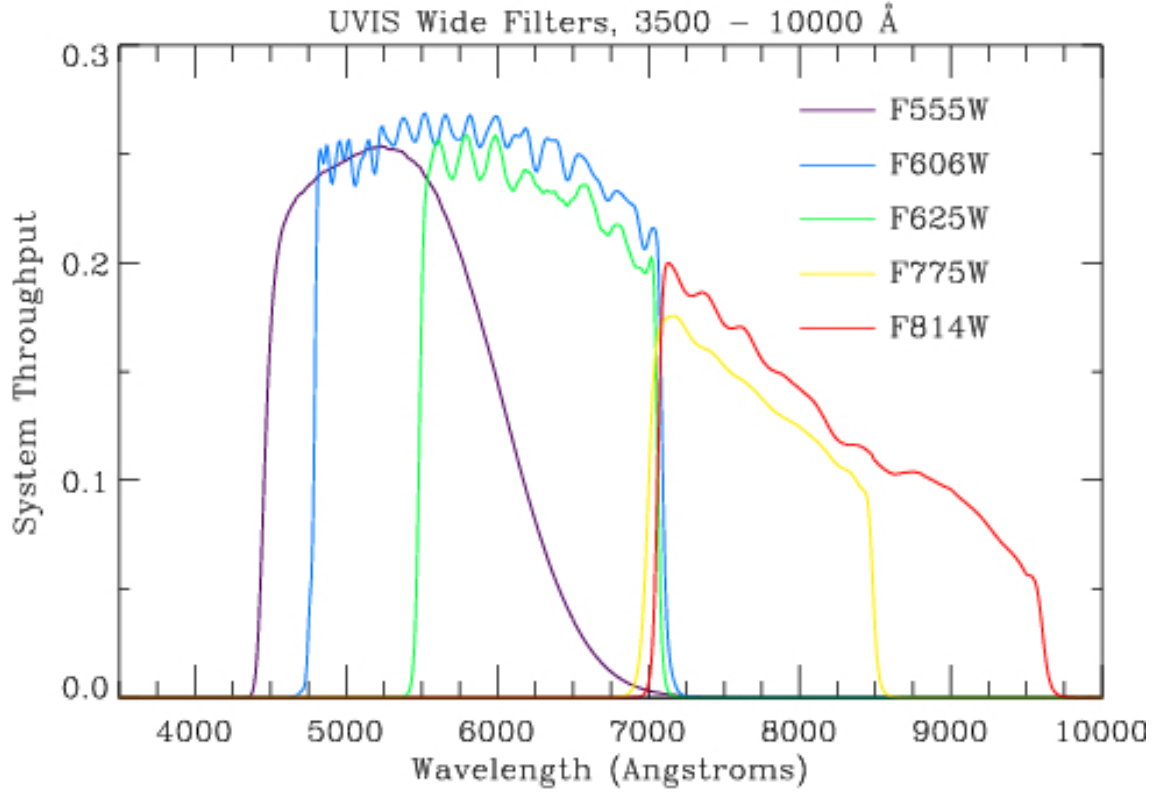


Figure 2.6: Filter response functions for wide-field WFC3 filters. Source: [http://www.stsci.edu/hst/wfc3/ins\\_performance/throughputs/UVIS\\_filterthru.html](http://www.stsci.edu/hst/wfc3/ins_performance/throughputs/UVIS_filterthru.html)

functions.

## 2.4 Variations in extinction ratio data due to stellar atmospheres

The data showing variations in the  $A_X/A_V$  data, generated via Equations 2.6 and 2.8, with effective temperature are shown for the WFC3 and Gaia filters in Figure 2.7 and for the ACS filters in Figure 2.8. It can be seen in the right-hand column of Table 2.2 that there are significant variations in the  $A_X/A_V$  data as the parameters describing the model stellar atmosphere are varied. In particular, for the shortest-wavelength WFC3 UV filters, the total range can be greater than 2.0, which, for a chosen  $A_V$  of 1 mag, means that the extinction for different types of stars can vary by as much as two orders of magnitude, purely as a result of the type of star being observed.



System	Filter	Minimum $A_X/A_V$	Maximum $A_X/A_V$	Total $A_X/A_V$ range
ACS	F435W	1.263	1.355	0.092
	F475W	1.117	1.229	0.112
	F555W	0.998	1.047	0.049
	F606W	0.865	0.962	0.097
	F625W	0.835	0.865	0.030
	F775W	0.624	0.651	0.027
	F814W	0.565	0.610	0.045
WFC3	F218W	0.897	2.935	2.038
	F225W	0.586	2.634	2.049
	F275W	0.773	2.065	1.292
	F300X	1.323	2.043	0.720
	F336W	1.587	1.647	0.060
	F390W	1.390	1.484	0.094
	F438W	1.302	1.352	0.050
	F475W	1.110	1.220	0.110
	F555W	0.977	1.080	0.103
	F606W	0.869	0.965	0.094
	F625W	0.841	0.879	0.038
	F775W	0.629	0.657	0.028
	F814W	0.566	0.615	0.049
Gaia	$G$	0.636	1.033	0.397
	$G_{\text{bp}}$	0.943	1.220	0.277
	$G_{\text{rp}}$	0.566	0.676	0.110

Table 2.2: Global minima and maxima (over all combinations of  $T_{\text{eff}}$ ,  $\log(g)$  and  $[\text{Fe}/\text{H}]$ ) for  $A_X/A_V$  in each of the filters studied in this project.

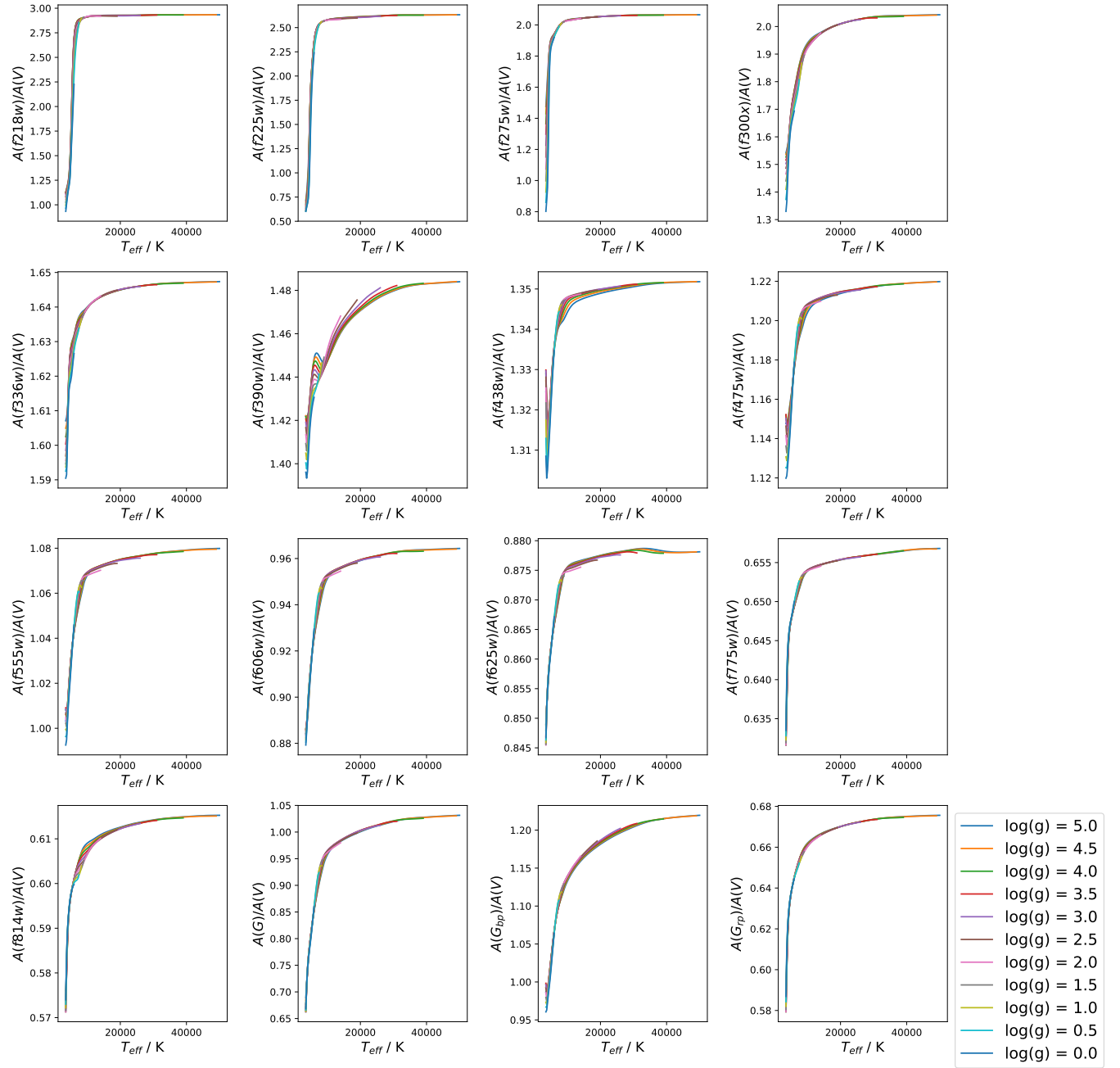


Figure 2.7: Solar-metallicity extinction ratio data for the WFC3 (first 13 panels) and Gaia (last 3) systems, with point-to-point lines connecting datapoints for a fixed  $\log(g)$  value.

This is important as these variations are independent of any effect due to interaction of the light emitted with the ISM. By looking at the scales of the vertical axes in these figures, it is clear that both the average value of, and the variations in,  $A_X/A_V$  are of different magnitude in different filters. For example, an overall trend seems to

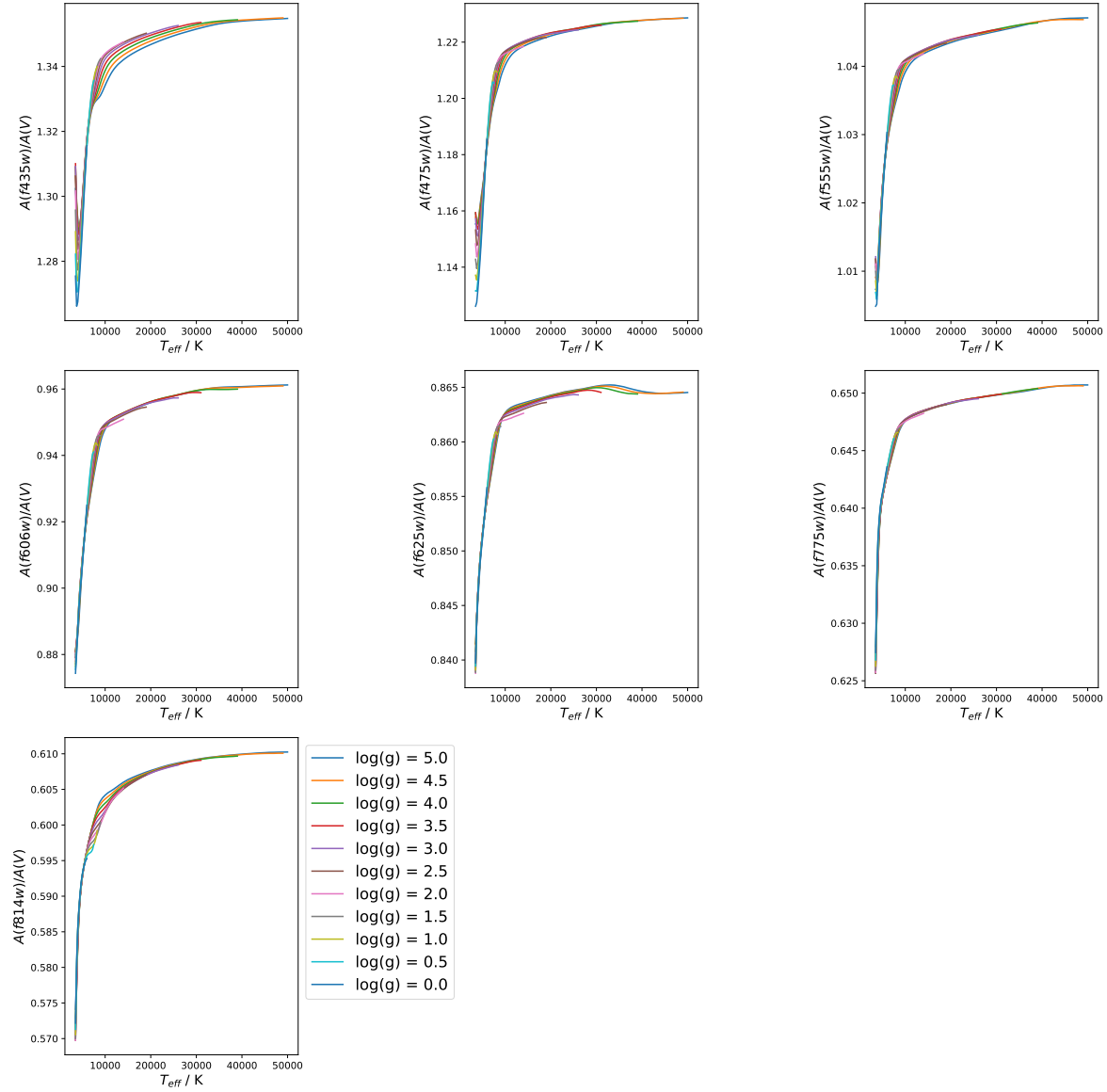


Figure 2.8: Same as Figure 2.7, except the filters shown here are for the ACS system.

be that bluer filters produce higher average values of  $A_X/A_V$ , which is expected given the variations of extinction with wavelength used for Equation 2.6, as shown in Figure 1.2.

To model these data, functions of  $T_{\text{eff}}$ ,  $\log(g)$  and  $[\text{Fe}/\text{H}]$  were created which would be able to describe the variations in  $A_X/A_V$  to a sufficient degree of accuracy. The aim of creating these functions is to reduce the large quantity of data present in the tables resulting from the implementation of Equation 2.8 across all available ATLAS9 atmospheres, with the same information being stored instead as the much smaller number

Isochrone (Age/Myr , [Fe/H])	$T_{\text{eff}}$ minimum	$T_{\text{eff}}$ maximum	$\log(g)$ minimum	$\log(g)$ maximum
500,0.002	2870	9640	0.886	5.137
1000,0.002	2824	8035	1.608	5.184
5000,-1.049	3118	7112	0.456	5.318
10000,-1.049	3086	6412	0.286	5.332

Table 2.3: Ranges of effective temperature and surface gravity in selected BaSTI isochrones

of coefficients for the functions. For each filter, there was a unique combination of coefficient values and, in certain cases, a new function and number of coefficients.

\*\*\*\* QUANTIFY THINGS IN THE PARAGRAPH BELOW!!! To generate the coefficient values and errors, the form of the function was set manually after visually examining the variations in the  $A_X/A_V$  data when plotted against three stellar atmosphere parameters. These functions were then fitted to the data using a least-squares fit algorithm, with the function coefficients acting as the free parameters to be fitted. The acceptable standard deviation in  $A_X/A_V$  for the fit was also set manually. If a particular function form was unable to accurately describe the data, or could not be fitted without producing infeasibly large or near-zero errors in one or more coefficients, it was modified or discarded as appropriate. This was repeated until a function could be found for each of the filters studied in this project which could describe the data to at least a reasonable degree of accuracy, using coefficients with plausible errors.

## 2.5 Isochrone CMD fitting

To match the quantities of observational datasets (with unknown extinction) and isochrones, it is necessary to correct the observational data for distance and add extinction to the isochrones. This is that standard procedure used when analysing observational data, as detailed in Section 1.2.2. Thus, the  $M_{\text{ext},X}$  (see Equation 1.17) values for the isochrones and the observational data are being compared. The functions, whose final forms and coefficients are detailed in Section 3.1, were then applied to the isochrone object dataset, producing values of  $M_{\text{ext},X}$  for each filter for all objects, as is the standard for analysing observational data with unknown extinction values. The colour magnitudes for stars in isochrones were calculated after the extinction ratios and  $A_V$  as  $(X - Y) = M_{\text{ext},X} - M_{\text{ext},Y}$ .

When comparing the two methods for calculating extinction, in order to test for any differences in projected isochrone age via the MSTO, a range of ages must be considered. A “primary” age was utilised as the true cluster isochrone age. This primary

isochrone was subjected to both the function-based (FBER) and fixed extinction-ratio methods. Two isochrones with ages equidistant from the primary were subjected to the standard fixed-extinction method only. All four of the resulting  $M_{\text{ext},X}$  isochrones were plotted together in the four chosen CMD axes, together with the original (zero-extinction) isochrone for visual reference.

This procedure was employed for two values of  $A_X/A_V$  for the fixed-extinction treatment. Both were extracted from the ATLAS9 data tables for a  $\log(g)$  value of 5.0 to represent a main-sequence star, which is suitable when MSTO positions are being compared. Given the large number of filters studied in this project, four commonly-used CMD axes were selected to test for any effects of a  $A_X/A_V$  function. Two of these are specific to the WFC3 system, with one CMD each for ACS and Gaia.

## 2.6 Observational test case: NGC 6793

To test the effects of the two different treatments of  $A_X/A_V$  on observational data, both were employed to predict the isochrone parameters (age,  $[\text{Fe}/\text{H}]$  and  $A_V$ ) for the open cluster NGC 6793.

NGC 6793 has little information available in the literature when compared to other open clusters (Bossini et al., 2019). Three observational studies have been published which give estimates for the properties of the cluster. The basic properties for all three studies are listed in Table 2.4.

However, NGC 6793 was selected as the test case because it has the significant advantage of having both a high  $A_V$  extinction value among known star clusters (see the discussion in Section 2.1.3) and a full set of Gaia parallax measurements for its member stars. The accurate distances to all its members allows for a higher degree of confidence in the position of the observed cluster CMD. Meanwhile, a high  $A_V$  value increases any disagreement between the extinction treatments being compared for the cluster. Consequently, any resulting disagreement in estimates of the best-fit isochrone parameters for the cluster become greater and more significant. Furthermore, the presence of multiple studies, all of which disagree on the values of the cluster age and distance and none of which provide a final estimate of the cluster metallicity. Therefore, these studies disagree on precise location of the isochrone in the CMD, which provides an opportunity to test the effect of changing the method of extinction treatment for multiple published isochrone paths while keeping the same single observational dataset, thus making this cluster more useful regarding the goals of this project\*\*\*\*.

The Gaia DR2 dataset for NGC 6793 was obtained from the VizieR online data catalogue provided by Gaia Collaboration et al. (2018). The data contained the paral-

Cluster property	K05	K13	GC18
Distance modulus / mag	10.73	9.399	8.894
-> distance / pc	1400	724	601
log(age / yr)	8.64	8.695	8.78
-> Age / Myr	437	495	603
$E_{B-V}$ / mag	0.17	0.312	0.272
-> $A_V$ / mag (if $R_V = 3.1$ )	0.53	0.967	0.843
[Fe/H]	?	?	?
Members	? (> 3 ACSS-2.5)	133*	465 (271 with Gaia photometry)**
Parallax / mas	?	?	$1.6672 \pm 0.0021$
Proper motion (RA) / (mas/yr)	?	?	$3.8120 \pm 0.0131$
Proper motion (Dec) / (mas/yr)	?	?	$3.5622 \pm 0.0136$

\*number of  $1\sigma$  objects inside MWSC "cluster corona border"

\*\*apparent disagreement between member numbers for clusters listed in Tables 2 and A.4 in GC18.

Table 2.4: Observational parameters for NGC 6793, according to Kharchenko et al. (2005) (K05, WEBDA archive page), Kharchenko et al. (2013) (K13, VizieR archive page) and Gaia Collaboration et al. (2018) (GC18), respectively.

laxes and proper motions (PMs) for both the cluster and its 465 members the members' apparent magnitudes in all three Gaia filters. All parameters came with error estimates. The resulting CMD is shown in Figure 2.9. However, the full dataset includes objects with distances which appear to lie far outside the expected range based on studies of other open clusters (Schilbach et al., 2006). Therefore, to restrict the dataset to a more realistic stellar population, distance cuts were implemented. In line with the limits set out by Schilbach et al. (2006), the highest cluster radius limit was selected initially.

Since the Gaia data also included PMs for all objects, this information can also be used to test the feasibility of the initial sample of stars. Regarding the PM of cluster members, the membership calculation method of Kharchenko et al. (2003) was employed. For each object, this method gives membership probabilities of (a) 61%, (b) 14% and (c) <1% Dias et al. (2006) if the following conditions are satisfied:

- the object is within (a)  $1\sigma$ , (b)  $2\sigma$  and (c)  $3\sigma$ , respectively, of the mean cluster PM (given in Table 2.4).
- the object is within a photometric error of  $1\sigma$  of the colour index to the left (bluer side) of the zero-age main sequence (ZAMS) in the CMD.

The first condition was tested first for the NGC 6793 data. Limits were placed on the deviation of the PM of the member stars from the cluster in both the right ascension and declination directions. The errors on the PMs for the individual stars are between one and three orders of magnitude greater than the error on the cluster

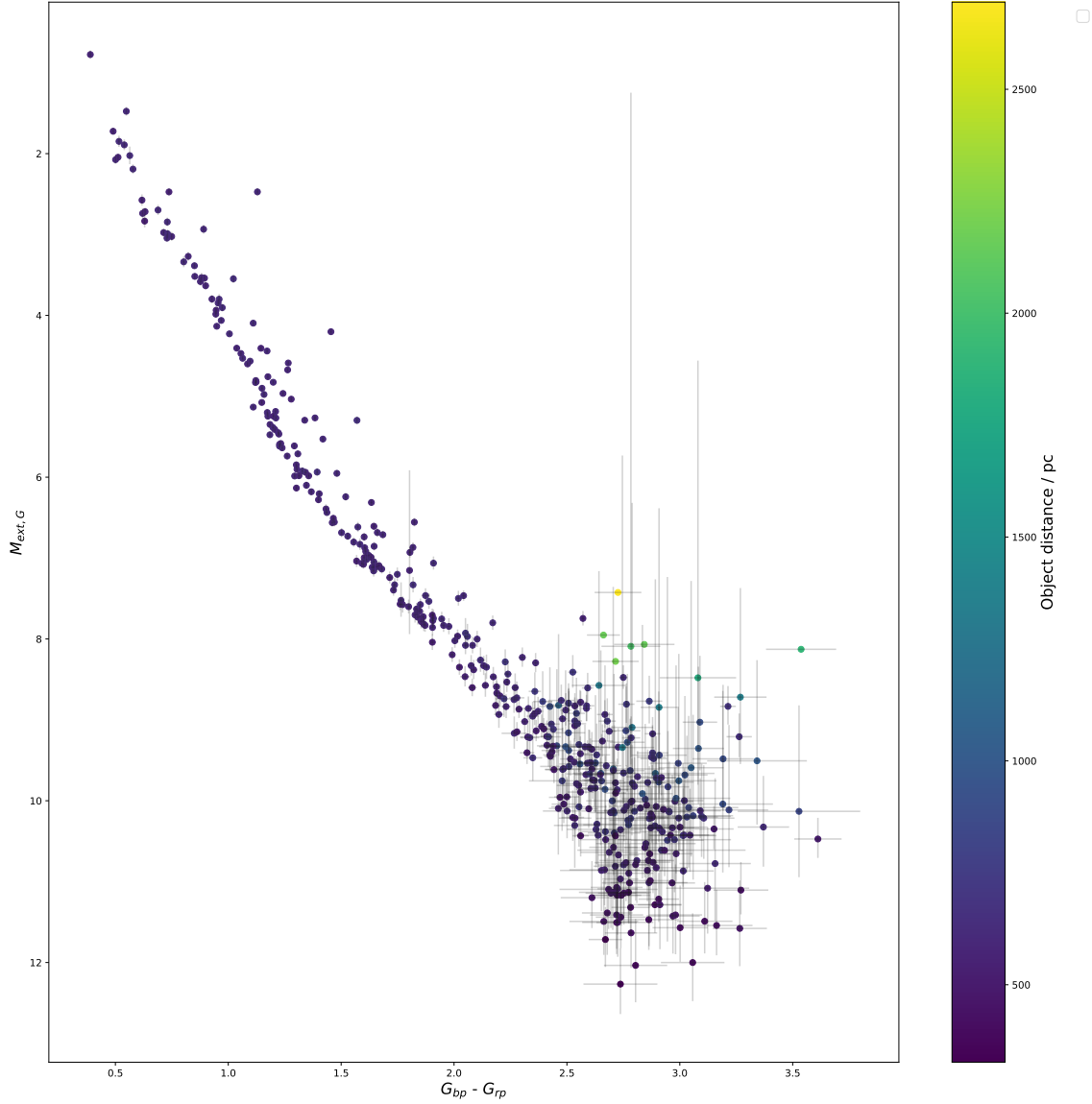


Figure 2.9: Gaia  $G$ -( $G_{bp}$ - $G_{rp}$ ) CMD of NGC 6793, showing the 465 cluster members in the GC18 VizieR table, corrected for their individual distances with errorbars shown. The color of each object is determined by its parallax-derived distance, while the errorbars are calculated using both photometric and parallax errors.

PM in both directions. Therefore the  $\sigma$  selected for use in both directions was that of each respective star. As with the radius criterion, a generous threshold was set for the PM of  $3\sigma$ . The results of the PM and radius-based criteria were plotted together to be compared visually in the cluster CMD.

The results are shown in Figure 2.10. Despite the low threshold of success for both criteria, only 129 stars out of 465 ( $\sim 28\%$ ) fulfil both simultaneously. Looking at the

results of Figure 2.10 and the distance and errors for the same objects shown in Figure 2.9, several conclusions can be drawn:

- The proper motion criterion is satisfied by a significantly higher number of stars than the radius criterion (340 and 231, respectively).
- The radius criterion selects almost all of the brightest MS stars in the data, but a significant portion of these are not selected using the PM criterion.
- The stars with the most anomalous calculated distances and the highest parallax errors in Figure 2.9 are nearly all selected using the PM criterion only. These objects are also in the faintest region of the CMD, which likely contributes to their high parallax errors. These objects, in general, were also found to have higher-than-average PM errors, which is likely to be the cause of their selection by the PM criterion.

Consequently, the PM criterion was deemed unnecessary for the isochrone comparison required for testing extinction treatment methods. Even without the additional colour-index constraint from Kharchenko et al. (2003) and using a very low membership success threshold, the criterion results in a CMD with too few bright MS stars, which meant that the comparison of isochrone ages using the MSTO region could not be carried out.

Hence, the radius criterion was implemented, giving 231 objects in the CMD to be analysed, which is smaller than the sample of 271 members used by GC18 for their parameter determination. The size and composition of the final dataset adequately reflected both the need for maintaining sufficient data points, to achieve a valid comparison to the previous studies of NGC 6793, particularly GC18, and the need to eliminate the most anomalous data from the GC18 cluster sample.

The isochrone fitting for NGC 6793 was done by eye using a plot of the cluster's observed Gaia CMD, with the position of each star corrected for its parallax distance. Using the values of  $E_{B-V}$  and age from GC18, a standard-case isochrone was derived, again assuming a diffuse ISM (i.e.,  $R_V = 3.1$ ). The standard treatment was employed twice, creating a different isochrone each time. Each time, a different fixed value of  $A_X/A_V$  was used, reflecting the significant changes in the value of  $A_X/A_V$  for different stellar types, as noted in Section 2.4. The fitting process was carried out in sequential stages:

1. First, the upper main sequence of the FBER isochrone below the MSTO region was fitted to that of the standard-case isochrone by varying the value of  $A_V$  used to calculate the final FBER value for each stellar object.
2. Next, the FBER isochrone metallicity was varied in an attempt match the observed lower main-sequence.



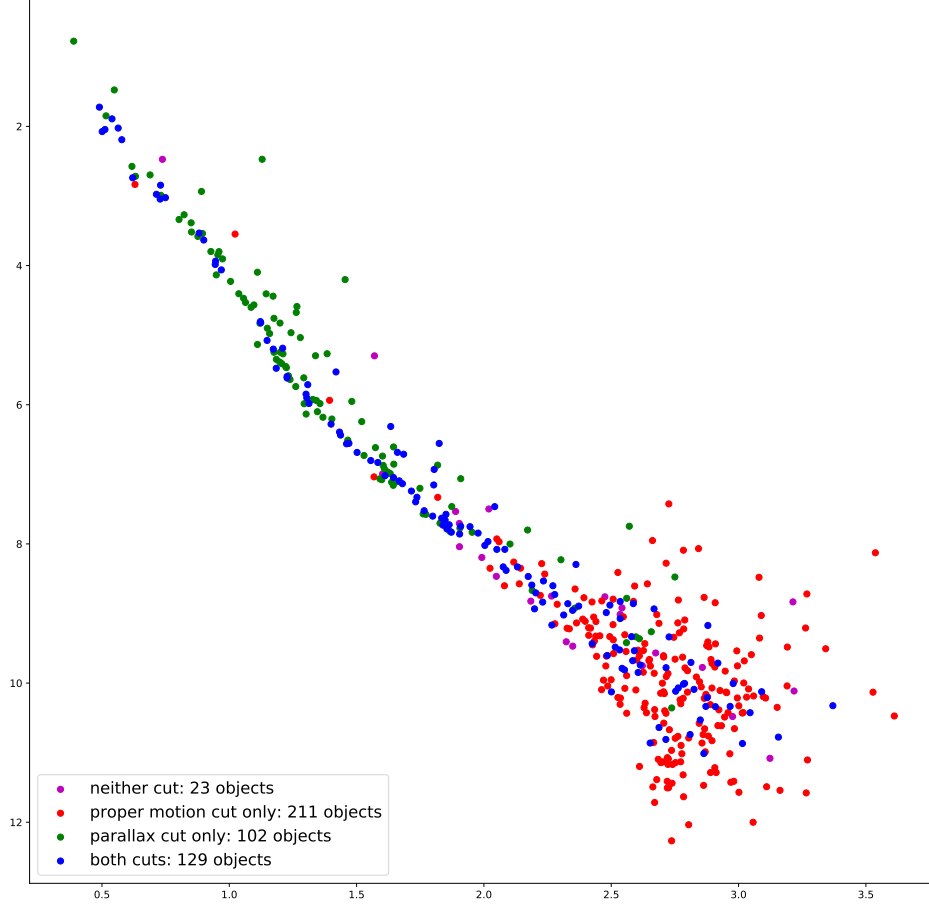


Figure 2.10: CMD showing all 465 NGC 6793 cluster source objects from the initial dataset. The colour indicates the membership likelihood of each source. The stars with the highest likelihood (in blue) are those which satisfy both the proper motion and cluster radius criteria. Those which fulfil only the proper motion criterion are shown in red and those which fulfil only the radius criterion are in green. Purple indicates stars which fulfil neither.

3. Finally, the age of the FBER isochrone was varied to match the observed MSTO location in the NGC 6793 data as far as possible.

It should be noted that, when fitting to the upper main sequence below the MSTO, priority was given to fainter objects in the MS, as these are most likely to be obser-

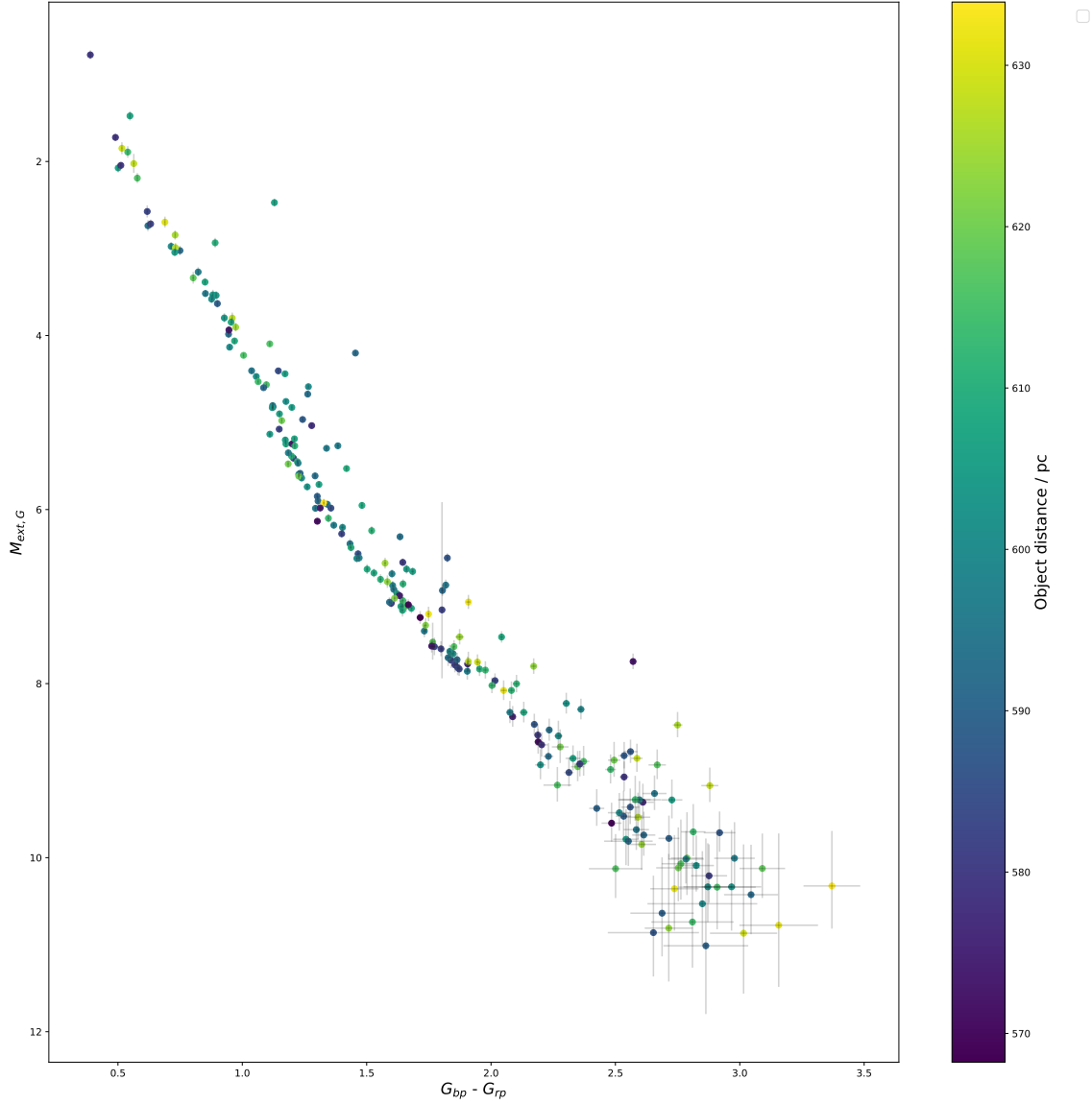


Figure 2.11: Gaia  $G$ -( $G_{bp}$ - $G_{rp}$ ) CMD of NGC 6793 after \*\*\*\*cuts have been applied. The positions, colours and errors of each objects are the same as in Figure 2.9.

variations of single stars unaffected by photometrically-unresolved binary companions, making them the most likely to conform to the predictions of stellar evolution models. \*\*\*\*linkage!!!! \*\*\*\*The isochrone with the resulting parameters was then plotted alongside the two standard-case isochrones. The resulting curves were compared to each other for accuracy with respect to the observational data. In the final stage, the FBER isochrone and the most accurate of the two standard-case isochrone were plotted over the data and their positions and isochrone parameters compared.

## 2.7 Software used

### 2.7.1 Isochrones

The isochrones used in this project were generated using the latest Bag of Stellar Tracks and Isochrones (BaSTI) web interface (Pietrinferni et al., 2004; Hidalgo et al., 2018). The filter systems whose throughput data were employed by BaSTI to generate the fluxes for the isochrones were ACS, WFC3 and Gaia-DR2. It should be noted that the WFC3 isochrone output for BaSTI does not include flux magnitudes for the F300X filter.

To obtain isochrones from the online database, the desired range of isochrone ages, initial metallicity and photometric filter system must be specified. Therefore, the values of these quantities are shared by all stellar objects in any given isochrone. The output from the BaSTI database for each model stellar object gives the object's initial mass and current mass (i.e. after a time equal to the isochrone age), together with the logarithms of the stellar luminosity in solar units ( $\log(L/L_{\odot})$ ) and of the effective temperature in K ( $\log(T_{\text{eff}})$ ), followed by the predicted absolute magnitudes (with zero extinction) of the object in each filter of the system.

### 2.7.2 Stellar atmosphere models

To generate the predicted stellar flux, pre-calculated ATLAS9 model stellar atmosphere spectra (Kurucz, 1993) were employed. The spectra came in the form of tables incorporated wavelengths, ranging from 9 nm to 160,000 nm, with a resolution of 2 nm or less in the UV, and the predicted monochromatic flux at those wavelengths. Each table, representing one stellar spectrum, is identified by the surface gravity, effective temperature and metallicity of the stellar atmosphere producing that spectrum. Table 1 of Castelli & Kurucz (2004) contains precise details of the coverage of the model atmospheres in  $(T_{\text{eff}}, \log(g))$  parameter space, while a brief summary of the limits of the space is listed in Table 2.5. Four input metallicities were used for ATLAS9, at values of  $[\text{Fe}/\text{H}] = -2, -1, 0$  and  $0.5$ , covering the metallicities of most observed globular and open clusters. The data for each metallicity value was subject to the same  $T_{\text{eff}}$  and  $\log(g)$  coverage in ATLAS9.

To make the results of this project apply to the greatest possible range of stellar types, the model atmospheres being employed must ideally be able to reproduce all observed stellar types. Since ATLAS9 atmospheres are constructed from a grid of  $T_{\text{eff}}$  and  $\log(g)$  values (Castelli & Kurucz, 2004), the simplest method of ascertaining their applicability is to obtain the widest possible range of  $T_{\text{eff}}$  and  $\log(g)$  values for the stellar objects which make up the isochrones being employed.

Parameter / unit	Minimum	Maximum	Number of values
$T_{\text{eff}} / \text{K}$	3500	50000	76
$\log(g / \text{cm s}^{-2})$	0.0	5.0	11
$[\text{Fe}/\text{H}]$	-2.0	0.5	4

Table 2.5: Ranges for the input parameters for ATLAS9 atmospheric models

However, the BaSTI data format for a given isochrone does not include explicit values of the surface gravities or radii of the constituent stars. Therefore, to derive the surface gravity  $g$  of a given star, we must combine Equation 1.11, to derive the stellar radius, and Equation 1.13, resulting in the following definition of  $g$ :

$$g = \frac{4\pi G M_* \sigma_{\text{SB}} T_{\text{eff}}^4}{L_*} \quad (2.10)$$

After this had been completed for all points along an isochrone, each star had a co-ordinate in  $(T_{\text{eff}}, \log(g))$  parameter space, plus the metallicity of the overall isochrone model. These co-ordinates were then plotted over the grid of co-ordinates for which ATLAS9 spectra were available, as listed in Table 1 of Castelli & Kurucz (2004). The results are shown in Figure 2.12, using stars in isochrones with ages of 15 Myr (red points) and 15 Gyr (black points). These ages are near the available age limits for BaSTI stellar models at  $[\text{Fe}/\text{H}] = -1$ . The blue points represent the ATLAS9 model grid, which extends to the left beyond the  $T_{\text{eff}}$ -scale presented in the figure, up to a  $T_{\text{eff}}$  value of 50,000 K.

With the exception of the very coolest, and therefore faintest, main sequence stars in the bottom right of the figure, it is clear from Figure 2.12 that the ATLAS9  $T_{\text{eff}}\text{-}\log(g)$  grid covers the required parameter space for isochrones of all ages including extremely young and extremely old clusters. Any changes in the position of the isochrones in the  $(T_{\text{eff}}, \log(g))$  plane at the plotted ages due to a change in metallicity were found to have a minimal impact on the overlap between the ATLAS9 grid and both isochrones in the  $(T_{\text{eff}}, \log(g))$  plane. Crucially, the MSTO region and the vast majority of the main sequence are both within the region covered by the ATLAS9 grid at all ages and metallicities.

This near-complete coverage of stellar objects in isochrones at all ages allows the ATLAS9 data to be applied to the MSTO locations at all isochrone ages, which ensures the applicability of the best-fit isochrone parameter comparisons (see Section 2.5 later) to populations of all ages. Therefore, ATLAS9 is a suitable basis from which start calculating bolometric corrections and therefore, via Equation 2.8, extinction ratios.

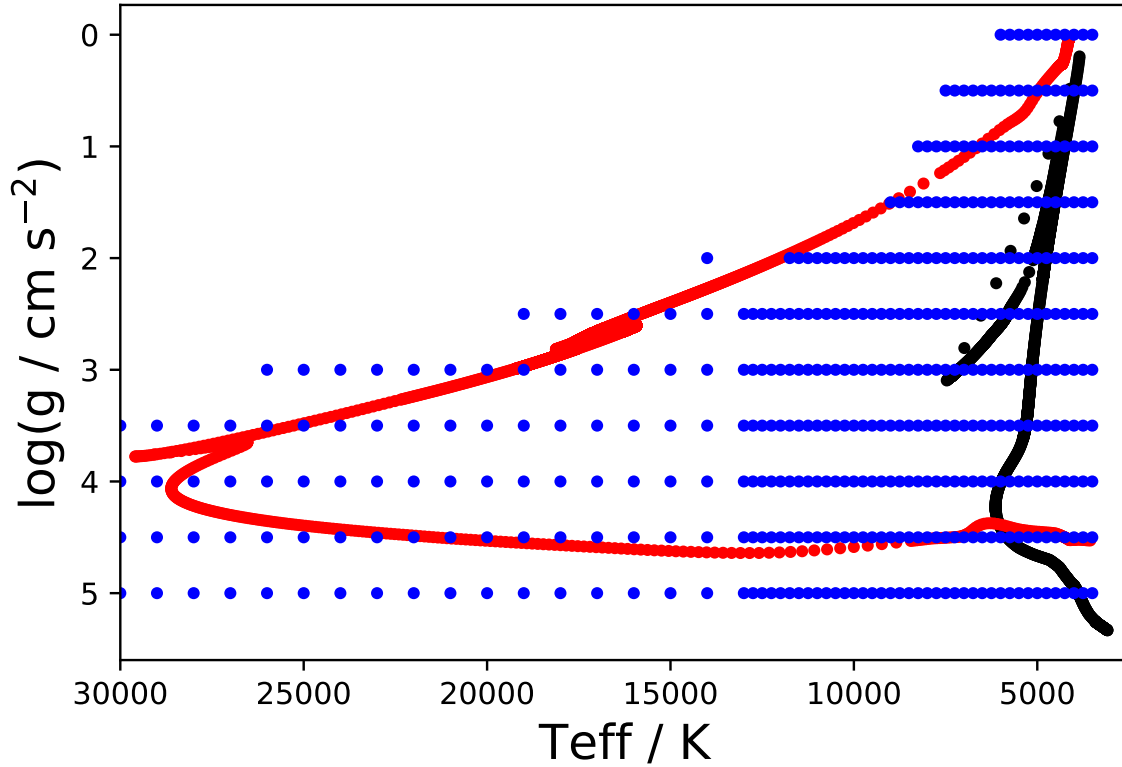


Figure 2.12:  $T_{\text{eff}}\text{-}\log(g)$  scatter plot for a BaSTI 15 Myr,  $[\text{Fe}/\text{H}] = -1$  isochrone (red), a BaSTI 15 Gyr,  $[\text{Fe}/\text{H}] = -1$  isochrone (black) and ATLAS9 model grid (blue) for  $T_{\text{eff}} \leq 30000$  K.

### 2.7.3 Programming languages

The tables of bolometric corrections were generated using a FORTRAN 77 code which incorporated Equations 2.4-2.8 and input data files with tables describing the response functions of all relevant filter systems (described in detail in Section 2.2) at the same wavelengths as those listed in the ATLAS9 model atmosphere tables, with the number of tables for each stellar metallicity value equal to the total number of  $(T_{\text{eff}}, \log(g))$  combinations available.

Once the bolometric correction tables were produced, all subsequent processes, including the subtraction required to obtain  $A_X/A_V$  shown in Equation 2.8, were written in Python 2.7 in the form of an IPython notebook. The repository containing all data, plots and programme codes for this project can be found at [https://github.com/AlexlwAstro/phd\\_work](https://github.com/AlexlwAstro/phd_work).

# Chapter 3

## Results and discussion

### 3.1 Extinction ratio models

In order to find suitable model functions without running into issues with degeneracy between coefficients, such as a coefficient that is multiplied into another (while incorrectly being treated as distinct), in the same function, the relative magnitude of the variations of  $A_X/A_V$  with each of the three stellar parameters became important. Degenerate coefficients were identified via two or more coefficients having both apparently plausible values, defined as values which were not at the limits or midpoint of the acceptable range set prior to fitting and which were produced consistently over many fitting iterations, and abnormally high standard deviations. If, upon further investigation, the coefficients were found to contribute to the same attribute of the overall function, the function was rewritten to combine the relevant coefficients into one describing the same attribute.

This resulted in relatively simple functions expressed solely in terms of  $T_{\text{eff}}$ , which caused the greatest variations, to be fitted first. The coefficients resulting from the fitting process were then incorporated into the function to form a predicted  $A_X/A_V$  model of  $T_{\text{eff}}$ . The residuals generated by the subtraction of this predicted model from the original data could then be examined for any significant disagreements between the data and these simple models and for any further variations with  $\log(g)$  or  $[\text{Fe}/\text{H}]$ . This allowed functions to be constructed incrementally, with a lower risk of becoming overly complex - too many coefficients would create errors that were significantly greater in degenerate coefficients than in non-degenerate ones. This would obscure any useful information about the validity of the function form.

The fitting operation for the initial functions of  $T_{\text{eff}}$  only was carried out on the dataset for solar metallicity ( $[\text{Fe}/\text{H}] = 0.0$ ) ATLAS9 atmospheres and, because it gave the greatest number of  $T_{\text{eff}}$  data points,  $\log(g) = 5.0$ . Due to the difficulties posed by the tail-flip phenomenon in certain filters, when fitting for  $A_{\text{pow}}$  and  $A_{\text{exp}}$ , the lower  $T_{\text{eff}}$  limit for the fitting data was set at 4500K for all filters. This dataset will be referred

to as the basic fitting data (BFD). The first functions to be fitted to the BFD had the following forms:

$$A_{\text{pow}} = \left( \frac{A_X}{A_V} \right)_{\text{pow}} (T_{\text{eff}}) = a(T_4)^b + c \quad (3.1)$$

$$A_{\text{exp}} = \left( \frac{A_X}{A_V} \right)_{\text{exp}} (T_{\text{eff}}) = a \exp(bT_4) + c \quad (3.2)$$

where  $T_4 = 10^{-4} \times T_{\text{eff}}$ . These functions were fitted separately to the BFD for each filter and compared both visually and via the size of the residuals. The most accurate function form was then selected as the final form. The results of this fitting process are detailed, for the cases where either the  $A_{\text{exp}}$  or the  $A_{\text{pow}}$  fitting result was sufficiently accurate, in Table 3.1. The table shows the filters and lists which of the two functions provided the best fit for the relevant data, followed by the respective coefficient values and the associated uncertainties. Due to the fitting data being restricted to atmospheres with  $T_{\text{eff}}$  values greater than 4500K, the models could not simply be assumed to apply to cooler atmospheres as well. The final column in Table 3.1 lists the lowest  $T_{\text{eff}}$  value for which the given combination of coefficient values is valid at all combinations of surface gravity and metallicity, denoted by  $T_{\text{min}}$ , together with the maximum deviation of the extinction ratio model from the data, over all stellar atmospheres with  $T_{\text{eff}} \geq T_{\text{min}}$ , including those not in the BFD (i.e, at non-solar metallicities and lower surface gravities), in brackets.

For the wide-field WFC3, ACS (Casagrande & Vandenberg, 2014) and Gaia (Casagrande & Vandenberg, 2018b) filters that were examined in the relevant studies, the opportunity was taken to compare the models for  $R_X = (A_X/E_{B-V})$  calculated in those studies, whose basic form is shown in Equation 1.8, with the  $A_X/A_V$  data calculated in this project for the same filters. To perform this comparison, it is necessary to define  $A_X/A_V$  explicitly in terms of  $R_X$ . Using the definitions of  $R_X$  and  $R_V$ , this can be done via the following equation:

$$\frac{A_X}{A_V} = \frac{R_X}{R_V} = \frac{R_X}{3.1} \quad (3.3)$$

The  $R_X$  models, when modified in this way to produce predictions of  $A_X/A_V$  values, consistently underestimate the  $A_X/A_V$  values listed in the data for atmospheres at  $\log(g) = 4.0$  (the  $R_X$  models used atmospheric data with  $\log(g) = 4.1$ ) in this project in almost all filters. However, within the metallicity and temperature ranges for which these  $R_X$  models are applicable (detailed in Section 1.1.2), they remain in agreement with the data to within a deviation in  $A_X/A_V$  of 0.03, which is a similar level of accuracy to that achieved by the  $A_X/A_V$  functions produced in this project for the same filters.

There were filters, namely the four WFC3 filters with the shortest central wavelengths (F218W, F225W, F275W and F300X), for whose BFD neither  $A_{\text{pow}}$  nor  $A_{\text{exp}}$  was able to produce an accurate fit across all combinations of  $\log(g)$  and  $[\text{Fe}/\text{H}]$ . For these filters, more intricate functions were sought, including functions with explicit dependences on  $g$  and  $[\text{Fe}/\text{H}]$ . Several unsuccessful methods were made before an acceptable function was found for these filters.

The most successful approach for these filters involved plotting all the available  $A_X/A_V$  data for each filter, in all possible 2D and 3D axis combinations, and analysing it visually. The trends seen in the data were analysed to determine both a basic overarching function for the extinction ratio, describing the greatest variations in  $T_{\text{eff}}$ , and describing the parameters in this function using further mathematical functions (referred to hereafter as “sub-functions”) within this main function. Examples of sub-functions are given in Equations 3.4 and 3.5, with the relevant overarching function given in Equation 3.6.

The details of the final form of the functions for these filters, including dependences on any of the stellar parameters, were deduced by fitting a logistic function of  $T_{\text{eff}}$  to the  $A_X/A_V$  data for each  $([\text{Fe}/\text{H}], \log(g))$  combination. This was chosen on the basis that  $A_{\text{exp}}$  had been superior to  $A_{\text{pow}}$  in describing the data for these particular filters and because the low- $T_{\text{eff}}$  change in gradient appeared to be more significant than for other filters. Furthermore, the gradient was not inverted, as can be seen in Figure 2.7, thus avoiding any tail-flicks. Of particular importance was the additional fact that the  $T_{\text{eff}}$  gradient in the region between the shallow low- $T_{\text{eff}}$  gradient and the plateau appears to lead to an asymptote at lower stellar effective temperatures, if the shallower low- $T_{\text{eff}}$  gradient is ignored when constructing and fitting a function (as was done for both  $A_{\text{exp}}$  and  $A_{\text{pow}}$ ). In these four filters, this steep gradient was found to cause functions such as  $A_{\text{exp}}$  and  $A_{\text{pow}}$  to predict negative values of the extinction ratio at  $T_{\text{eff}}$  values that were still above the lowest values derived from observations of cool stars (excluding brown dwarfs). This issue is resolved by the logistic function’s property of converging to a constant value for both high and low values of  $T_{\text{eff}}$ . Therefore, for these filters, the data to which the functions were fitted encompassed all available  $T_{\text{eff}}$  values down to the ATLAS9 minimum of 3500K. For a general logistic function in  $T_{\text{eff}}$  (whose basic form is shown in Equation 3.6), there are four key parameters:

- The global maximum value, denoted in this case by  $A_{\text{max}}$ ;
- The global minimum value,  $A_{\text{min}}$ ;
- The exponential decay coefficient,  $k$ ;
- The  $T_{\text{eff}}$ -coordinate of the midpoint of the characteristic S-shape, or sigmoid, of the logistic curve function curve, in this case  $T_0$ .



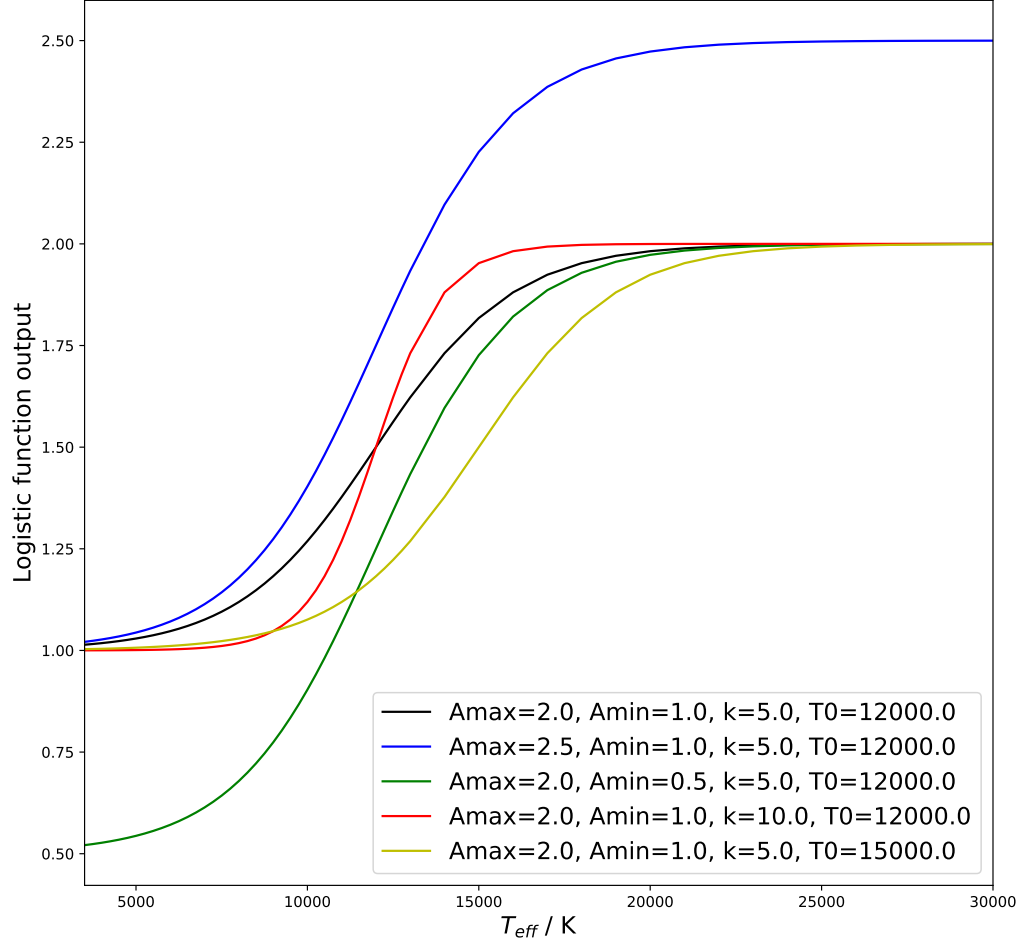


Figure 3.1: Plots of several generic logistic functions, all described by the four parameters ( $A_{\text{max}}$ ,  $A_{\text{min}}$ ,  $k$ ,  $T_0$ ) listed in the text. Each curve illustrates the effect of changing the value of one parameter, as detailed in the legend, from the values listed for the black curve.

Figure 3.1 shows a plot of five generic logistic curves of  $T_{\text{eff}}$  described by the four parameters listed above, with the black curve used as a reference and each of the other four curve differing from this curve by one of the four parameter values, as detailed in the legend. Changing the values of  $A_{\text{min}}$  (blue curve) and  $A_{\text{max}}$  (green curve) change the maximum and minimum of the function output, respectively, when compared to the black curve. Increasing the  $k$  value (red curve) causes a more rapid exponential decay between  $A_{\text{min}}$  and  $A_{\text{max}}$  and, by doing so, effectively reduces the  $T_{\text{eff}}$  range within

which output values change. Increasing the value of  $T_0$  (yellow curve) shifts the entire black curve to the right of the plot without changing its shape. Looking at  $A_X/A_V$  data for the four\*\*\*\* relevant WFC3 filters in Figure 2.7, it is apparent that while some of the logistic parameters, such as  $A_{max}$ , can be taken as constant for all combinations of  $\log(g)$  and  $[\text{Fe}/\text{H}]$ , others clearly vary with these parameters. An example of the latter is  $T_0$ . The relevant curves in Figure 2.7 show that as  $\log(g)$  decreases, the  $A_X/A_V$  midpoint of the curve occurs at progressively higher  $T_{\text{eff}}$  - meaning that  $T_0$  must replicate this behaviour in the models. A similar pattern occurs when analysing the behaviour of  $A_X/A_V$  with varying metallicity in the same filters.

It was confirmed that this logistic function of  $T_{\text{eff}}$  could describe the  $A_X/A_V$  variations accurately in each filter for every combination of atmospheric  $\log(g)$  and  $[\text{Fe}/\text{H}]$  values, using the four parameters listed above. This was done numerically by fitting the logistic function to the  $A_X/A_V$  data for each  $(\log(g), [\text{Fe}/\text{H}])$  combination individually. The values produced for the four coefficients of the logistic function listed above for each of these fits were tabulated along with the  $\log(g)$  and  $[\text{Fe}/\text{H}]$  values of their respective datasets. This table was then analysed for trends in the coefficient values as  $\log(g)$  and  $[\text{Fe}/\text{H}]$  were varied. This allowed for the incremental construction, where necessary, of sub-functions to describe the parameters of the main  $T_{\text{eff}}$  logistic function in terms of  $\log(g)$  and  $[\text{Fe}/\text{H}]$ .

Many different forms, of varying complexity, were tested for these sub-functions. With each new form, the sub-functions were incorporated into the main  $T_{\text{eff}}$ -logistic function. In some cases, sub-functions with explicit  $T_{\text{eff}}$  dependences were included. The resulting function was then subjected to a fit on the entire  $A_X/A_V$  dataset, covering the entire  $(T_{\text{eff}}, \log(g), [\text{Fe}/\text{H}])$  parameter space available. The suitability of each function was influenced by both the size of the  $A_X/A_V$  residuals and on the relative errors on the coefficients resulting from the fit. The importance of the latter was due to multiple factors:

- the possibility of degeneracies between coefficients being overlooked during the construction of either the sub-functions, the overall function or both, which would result in anomalously high errors for the relevant coefficients;
- the possible occurrence of near-zero best-fit value for a given coefficient with a high associated error, indicating that the coefficient was describing a trend not actually present in the data and that, therefore, the overall function was overly complex;
- the danger of coefficient values not departing from the initial value with zero error, indicating that, for that coefficient, the algorithm was unable to achieve convergence, even after a very large number of iterations.

The best form for the sub-functions which represented  $T_0$  and  $k$  in each filter were found to be simple functions of  $\log(g)$  and  $[\text{Fe}/\text{H}]$ , independent of  $T_{\text{eff}}$  variations, as

System	Filter	Function ( $A_{\text{pow}}$ or $A_{\text{exp}}$ )	Coefficients			$T_{\text{min}}$ / K	Max. deviation in $A_X/A_V$
			$a$	$b$	$c$		
ACS	F435W	exp	$-0.1436 \pm 0.0310$	$-2.159 \pm 0.360$	$1.352 \pm 0.002$	3500	0.03
	F475W	exp	$-0.2137 \pm 0.0469$	$-2.660 \pm 0.380$	$1.226 \pm 0.002$	4000	0.03
	F555W	exp	$-0.0914 \pm 0.0476$	$-2.677 \pm 0.901$	$1.045 \pm 0.002$	3500	0.01
	F606W	exp	$-0.2183 \pm 0.0554$	$-2.867 \pm 0.445$	$0.959 \pm 0.002$	3500	0.01
	F625W	exp	$-0.0719 \pm 0.0798$	$-3.332 \pm 2.000$	$0.865 \pm 0.002$	3500	0.01
	F775W	pow	$-0.0035 \pm 0.0042$	$-1.488 \pm 1.541$	$0.651 \pm 0.003$	3500	0.01
	F814W	pow	$-0.0070 \pm 0.0046$	$-1.374 \pm 0.830$	$0.611 \pm 0.003$	3750	0.02
WFC3	F336W	pow	$-0.0074 \pm 0.0041$	$-1.525 \pm 0.727$	$1.648 \pm 0.003$	3500	0.03
	F390W	exp	$-0.0695 \pm 0.0057$	$-0.644 \pm 0.177$	$1.489 \pm 0.005$	4500	0.04
	F438W	exp	$-0.1132 \pm 0.0658$	$-3.084 \pm 1.032$	$1.350 \pm 0.002$	3750	0.02
	F475W	pow	$-0.0179 \pm 0.0037$	$-1.718 \pm 0.275$	$1.220 \pm 0.003$	4000	0.02
	F555W	pow	$-0.0138 \pm 0.0033$	$-1.887 \pm 0.333$	$1.080 \pm 0.003$	3750	0.02
	F606W	exp	$-0.2131 \pm 0.0559$	$-2.879 \pm 0.460$	$0.962 \pm 0.002$	3500	0.02
	F625W	pow	$-0.0042 \pm 0.0031$	$-2.063 \pm 1.025$	$0.879 \pm 0.002$	3500	0.01
	F775W	pow	$-0.0033 \pm 0.0041$	$-1.529 \pm 1.634$	$0.657 \pm 0.003$	3750	0.01
	F814W	pow	$-0.0071 \pm 0.0046$	$-1.391 \pm 0.803$	$0.616 \pm 0.004$	4000	0.01
Gaia	G	pow	$-0.0888 \pm 0.0045$	$-1.402 \pm 0.064$	$1.040 \pm 0.004$	4000	0.02
	G <sub>bp</sub>	pow	$-0.1150 \pm 0.0081$	$-0.900 \pm 0.070$	$1.247 \pm 0.007$	3750	0.03
	G <sub>rp</sub>	pow	$-0.0159 \pm 0.0047$	$-1.352 \pm 0.368$	$0.677 \pm 0.004$	3750	0.02

Table 3.1: Coefficient values produced for each filter via  $A_{\text{exp}}$  or  $A_{\text{pow}}$  fitting, as appropriately labelled. Any filters missing from this table are those with data that could not be accurately fitted using either function. The errors are calculated using an acceptable  $1\sigma$  margin,  $\Delta(A_X/A_V)$ , of 0.01. The penultimate column displays the lowest effective temperature, including for atmospheres outside the BFD, for which the given model and coefficients were able to describe the  $A_X/A_V$  data across all values of  $\log(g)$  and  $[\text{Fe}/\text{H}]$  to within the global deviation shown in the final column.

shown in Equations 3.4 and 3.5, respectively. It was found that  $A_{\text{min}}$  and  $A_{\text{max}}$  were best expressed as constants for each filter. The overall function,  $A_{\text{logis}}$ , is therefore sensitive to all three input stellar atmosphere parameters, with effective temperature having the greatest effect and the other parameters having much smaller but still significant effects, with the relative magnitudes dependent on the values of the associated coefficients.

This final form of  $A_{\text{logis}}$  was able to accurately reproduce the behaviour of almost the entire dataset. The coefficients for Equations 3.4-3.6 are given in Table 3.2.

$$T_0 = a \log(g) + b \left( \frac{[\text{Fe}/\text{H}]}{||[\text{Fe}/\text{H}]||^{1/2}} \right) + c \quad (3.4)$$

$$k = d \log(g) + e [\text{Fe}/\text{H}] + f \quad (3.5)$$

$$A_{\text{logis}} = \left( \frac{A_X}{A_V} \right)_{\text{logis}} (T_{\text{eff}}, g, [\text{Fe}/\text{H}]) = \frac{(A_{\text{max}} - A_{\text{min}})}{(1 + \exp(-10^{-4}k(T_{\text{eff}} - T_0)))} + A_{\text{min}} \quad (3.6)$$

All the functions are consistent with the general trends predicted by the physics in stellar atmospheres, since the effective temperature has the greatest effect upon the

Filter	Coefficient						Max. deviation in $A_X/A_V$		
	$a$	$b$	$c$	$d$	$e$	$f$	$A_{min}$	$A_{max}$	
F218W	-120.9±4.1	467.6±7.9	5673±16	1.435±0.209	-3.211±0.382	19.19±0.62	1.026±0.012	2.909±0.003	0.25
F225W	-97.21±3.85	357.2±7.9	4967±22	-0.174±0.136	-2.691±0.256	18.62±0.55	0.337±0.028	2.581±0.003	0.3
F275W	-239.0±12.0	236.0±20.4	4161±79	-2.117±0.326	-2.140±0.445	22.20±1.48	0.409±0.113	2.030±0.003	0.2
F300X	-302.1±45.0	350±125	4270±913	-0.176±0.087	-0.352±0.115	4.315±0.529	1.000±0.199	2.015±0.004	0.15

Table 3.2: Coefficient values for the non-trivial  $A_X/A_V$  function  $A_{logis}$ , described in Equations 3.4-3.6, produced by fitting to UV filter data with The errors are calculated using an acceptable  $1\sigma$  margin,  $\Delta(A_X/A_V)$ , of 0.1. The bottom row represents the maximum deviation from the data across the entire ( $T_{eff}$ ,  $\log(g)$ ,  $[Fe/H]$ ) parameter space. All results are valid down to  $T_{eff} = 3500$  K.

value of  $A_X/A_V$ , with relatively minor effects due to spectral absorption lines, via surface gravity and metallicity. In general stars with higher effective temperatures (and consequently stronger and bluer flux spectra) experience higher  $A_X/A_V$  values in all filters than stars with low effective temperatures. The maximum  $A_X/A_V$  value in a given filter decreases as the filter's central wavelength increases. This is expected for black-body analogues (see Equation 1.9 and Figure 1.3). Both trends are also consistent with the known short-wavelength preference of physical mechanisms causing interstellar extinction in the spectral regions covered by the filters studied in this project.

In summary, these functions are sufficiently accurate to replicate the results that would be obtained by using interpolation between the  $(T_{\text{eff}}, \log(g), [\text{Fe}/\text{H}])$  points in the initial stellar atmosphere data tables. The accuracy of these relatively simple functions is important because the  $A_X/A_V$  dataset for each filter can now be reduced to a much smaller number of degrees of freedom, equal to the number of coefficients in the relevant function. The input parameters  $(T_{\text{eff}}, \log(g)$  and  $[\text{Fe}/\text{H}])$  are required regardless of whether interpolation of the tables of  $A_X/A_V$  data or the functions are being employed, and so they make no difference when comparing the information complexity of the tables versus the functions.

## 3.2 Effect on isochrones

Once the  $A_X/A_V$  models detailed in the previous section were finalised, they were applied to isochrones in order to simulate extinction in CMDs for a stellar population at the isochrone ages. The resulting curves were then compared with those resulting from the standard method of using constant  $A_X/A_V$  values. During this comparison of methods, particular focus was given to any differences between the CMD positions of the MSTO at a given isochrone age resulting from the two methods of extinction treatment. Any differences were then used to estimate the different isochrone ages required to achieve a given isochrone MSTO position.

The  $\log(g)$  values for the stellar model objects in the BaSTI isochrones first had to be explicitly determined from the model objects' masses and radii, in order to be able to apply the extinction ratio models to them for all filters. The equations detailed in Section 2.5 were applied to the BaSTI data in order to accomplish this. The  $A_X/A_V$  functions created in this project could then be applied to the resulting data tables.

When calculating the fixed-extinction  $A_X/A_V$  values to be applied to a given isochrone, the metallicity of the isochrone first had to be accounted for, particularly for the UV filters which required an  $A_{\text{logis}}$  model. The  $A_X/A_V$  value chosen for a given isochrone metallicity was taken from the ATLAS9 model whose metallicity best matched that of the isochrone. This ATLAS9 value will be denoted  $[\text{Fe}/\text{H}]_{CM}$ , where

‘CM’ stands for ‘closest matching’.

As noted at the end of Section 2.5, two values \*\*\*\*The first value was equal to  $(A_X/A_V)_{plat} = (A_X/A_V)(T_{\text{eff}} = 50,000\text{K}, \log(g) = 5.0, [\text{Fe}/\text{H}]_{CM})$ , and the second was equal to  $(A_X/A_V)_{MS} = (A_X/A_V)(T_{\text{eff}} = 5,000\text{K}, \log(g) = 5.0, [\text{Fe}/\text{H}]_{CM})$ . This was done to reflect the fact that, for the first case, the assumption of a constant extinction value is valid in the plateau region and, for the second, the fact that, given the position of the MSTO in terms of stellar  $T_{\text{eff}}$  values, it would be more prudent to ensure that the main sequence regions immediately below the MSTO align in the CMD, making it easier to see any disagreements in the turn-off ages. For each isochrone plot for these four CMDs, shown in Figures 3.2-3.9\*\*\*\*,  $A_V$  was fixed at a value of 1.0.

\*\*\*\*why use 50,000K?! plateau -> 15-20,000K\*\*\*\*

In each of the CMDs, the extinction ratio functions have been applied to a solar-metallicity ( $[\text{Fe}/\text{H}] = 0$ ), 500 Myr isochrone, which is shown as a solid orange line. A fixed extinction ratio has been applied to three solar-metallicity isochrones with ages of 400 (solid green), 500 (solid blue) and 600 (solid red) Myr, respectively. A solar-metallicity, 500 Myr isochrone with zero extinction is added for illustration purposes as a solid purple line.

### 3.2.1 ACS

The F435W-(F435W-F814W) CMD was chosen for the ACS. This CMD is useful as it pairs the bluest and reddest wide-field filters for the ACS in its colour index, which is the index most likely to distinguish between objects in a given dataset with a large range of effective temperatures, making it useful for modelling the main sequence and MSTO, the two most important CMD components for calculating cluster isochrone ages. This CMD corresponds, by design, to the pre-existing Johnson-Cousins  $B-(B-I)$  CMD (Siriani et al., 2005), which allows direct comparison of observed data with archive data obtained before the creation of the ACS filters.

It can be seen in Figure 3.2, by comparing the position of the blue and orange isochrones, that the impact of changing between the FBER and fixed-extinction methods in this CMD is insignificant. Although there are some larger differences in the position of the isochrone in the post-sub-giant branch (SGB) evolutionary stages, this is irrelevant when determining the isochrone age of an observed stellar population.

The result of using  $(A_X/A_V)_{plat}$  is not significantly different from that of using  $(A_X/A_V)_{MS}$  for this CMD. By comparing Figures 3.2 and 3.3, it is clear that any change in the fixed-extinction  $A_X/A_V$  value used in the F435W and F814W ACS filters (see Figure 2.8) is insignificant in the context of these isochrones.

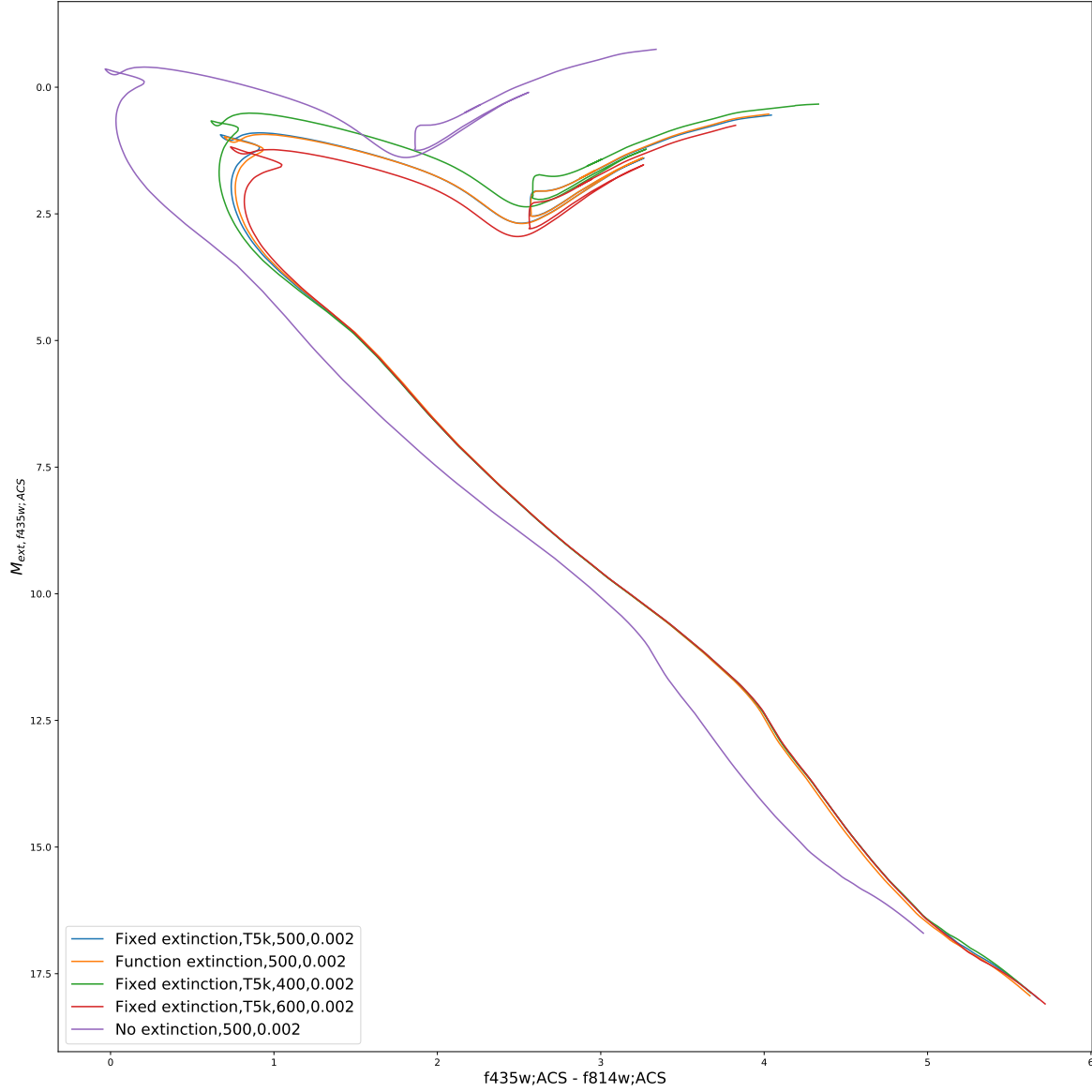


Figure 3.2: ACS F435W-(F435W-F814W) CMD with a fixed extinction ratio equal to  $(A_X/A_V)_{MS}$  for each filter

### 3.2.2 WFC3

Two different CMDs were chosen whose filters are part of the WFC3 system. The first is the F555W-(F555W-F814W) CMD. This CMD pairs a wide yellow filter (F555W) with the WFC3's reddest IR wide-field filter. This CMD mimics the pre-existing and widely used Johnson-Cousins  $V-(V-I)$  CMD (Sahu et al., 2014), which allows direct comparison of observed data with archive data obtained before the creation of the WFC3 filters.

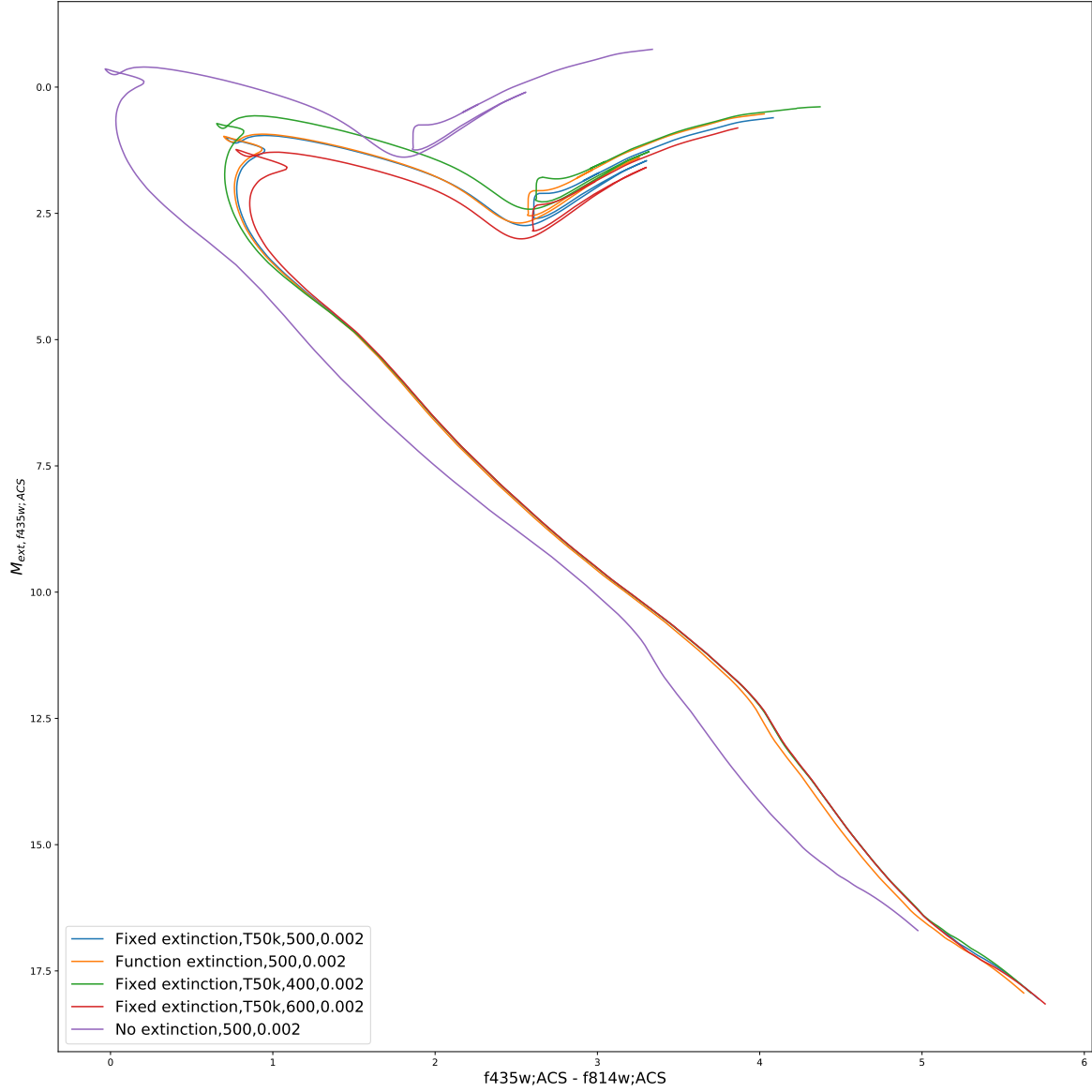


Figure 3.3: ACS F435W-(F435W-F814W) CMD with a fixed extinction ratio equal to  $(A_X/A_V)_{plat}$  for each filter

As with the previous ACS CMD, this CMD shows no significant changes in isochrone position resulting from either employing a FBER model or changing the extinction ratio value used for the fixed-value extinction model from  $(A_X/A_V)_{plat}$  to  $(A_X/A_V)_{MS}$  or vice versa, as demonstrated in Figures 3.4 and 3.5.

The second WFC3 CMD that was studied is the F814W-(F275W-F814W) CMD.



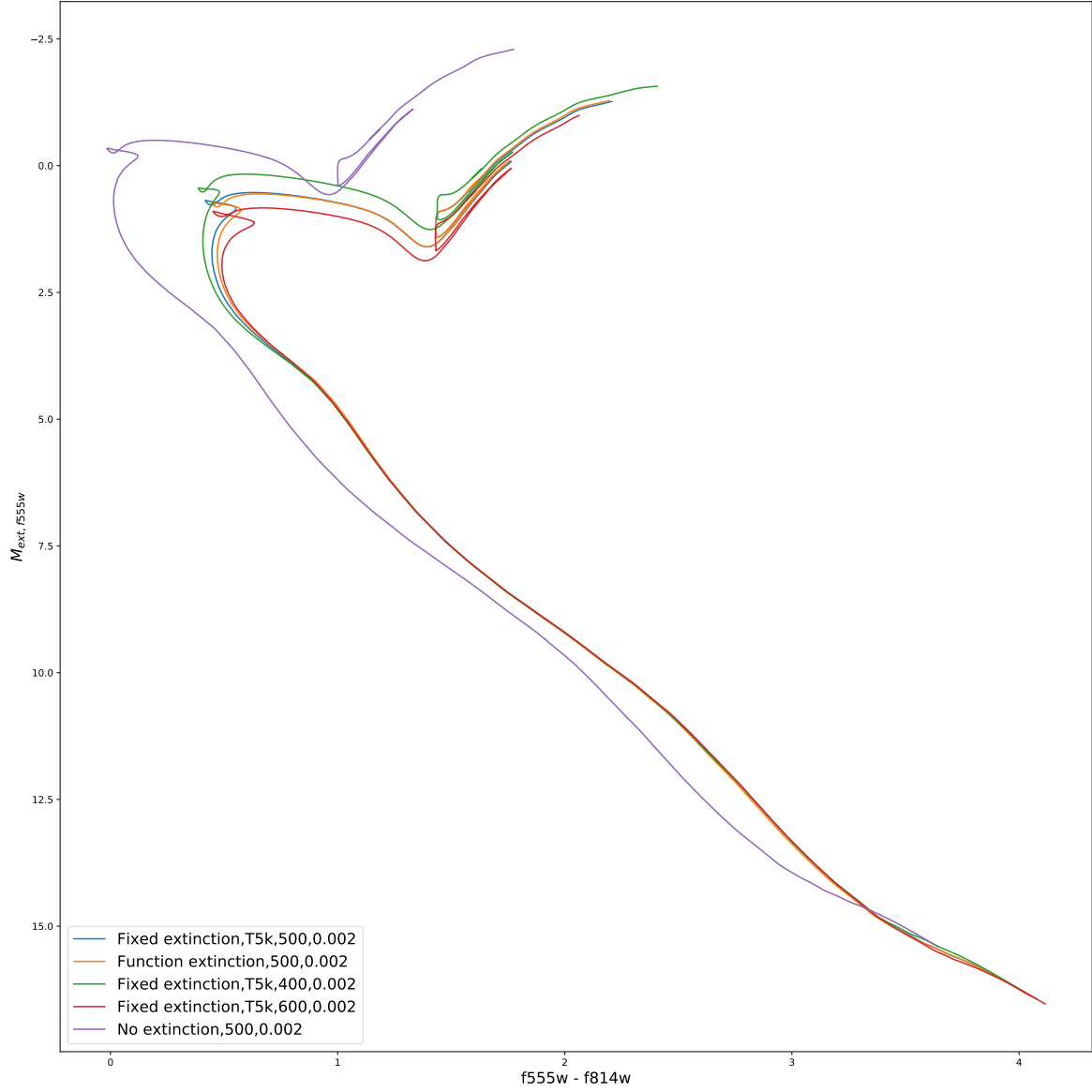


Figure 3.4: WFC3 F555W-(F555W-F814W) CMD with a fixed extinction value equal to  $(A_X/A_V)_{MS}$  for each filter

The filters that form this CMD cover the soft-UV and near-IR spectral regions. The high baseline wavelength coverage of this combination of filters makes the colour index more sensitive to differences in  $T_{\text{eff}}$  in hot horizontal branch (HB) stars. These objects are important due to direct helium abundance measurements (from absorption lines) being available in globular clusters only for HB stars with  $8000 \lesssim T_{\text{eff}} / \text{K} \lesssim 11500$  (Lagioia et al., 2018).

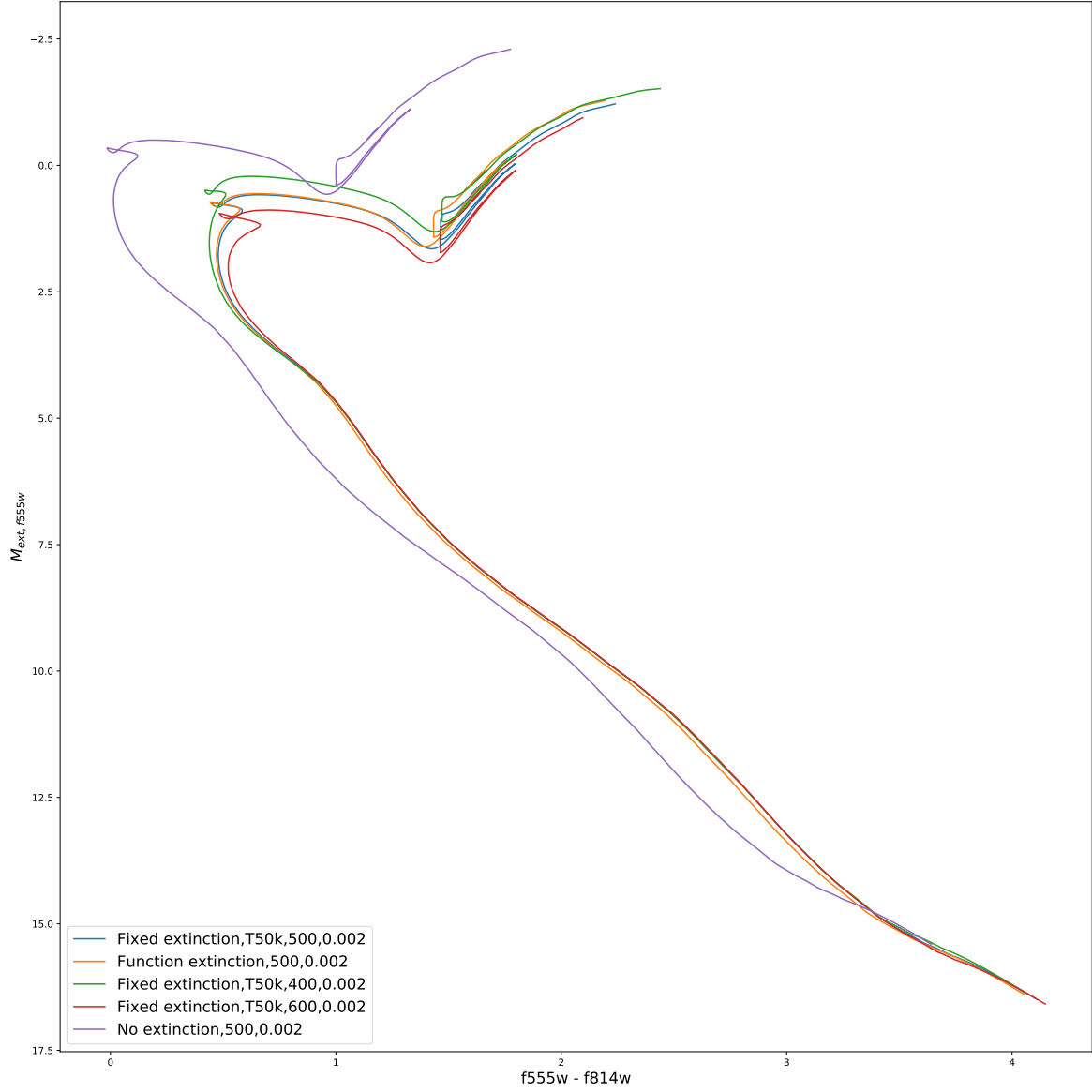


Figure 3.5: WFC3 F555W-(F555W-F814W) CMD with a fixed extinction value equal to  $(A_X/A_V)_{plat}$  for each filter

In Figure 3.6, it can be seen that, when the  $(A_X/A_V)_{MS}$  fixed model is being used as a reference (i.e., the models' upper main sequences below the MSTO are aligned), the position of the MSTO of the FBER 500 Myr isochrone aligns with that of the 600 Myr fixed-ratio isochrone. By the point at which the MS hook (Pols et al., 1998) appears, the FBER isochrone has almost realigned with the 500 Myr fixed-ratio isochrone. There are significant differences between the two 500 Myr isochrones after the lower portion of the RGB. In the lower main sequence, all isochrones with fixed extinction

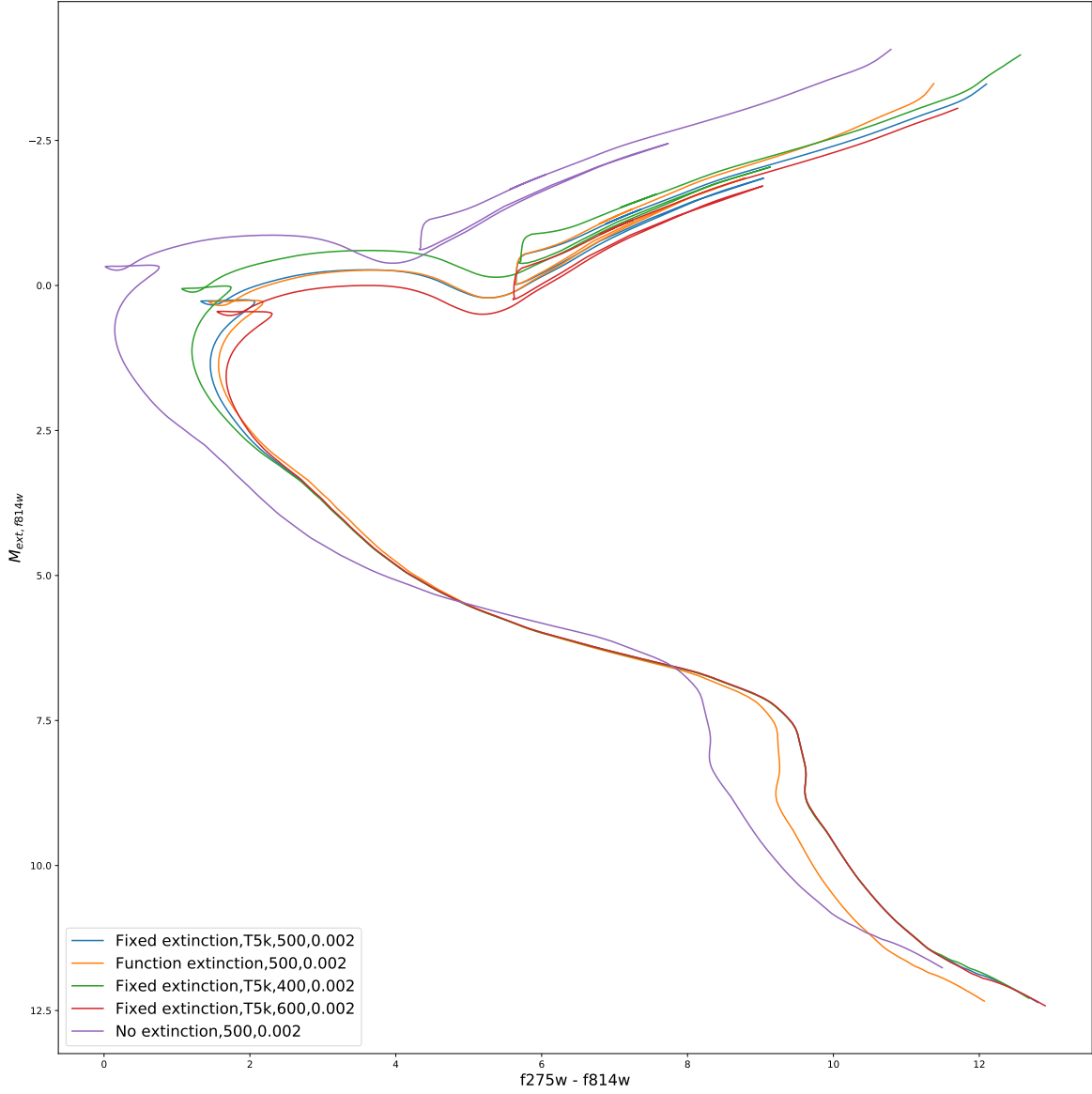


Figure 3.6: WFC3 F814W-(F275W-F814W) CMD with a fixed extinction value equal to  $(A_X/A_V)_{MS}$  for each filter.

ratios appear significantly redder, while the infrared F814W magnitudes appear to be more or less unchanged from the FBER case. This can only be the result of significant differences in  $A_{F275W}/A_V$  values between stars in the upper main sequence (higher  $T_{\text{eff}}$  values) and in the lower main sequence (lower  $T_{\text{eff}}$  values), as these differences are not reflected in the fixed-extinction models.

As shown in Figure 3.7, choosing  $(A_X/A_V)_{\text{plat}}$  for the fixed-extinction isochrones

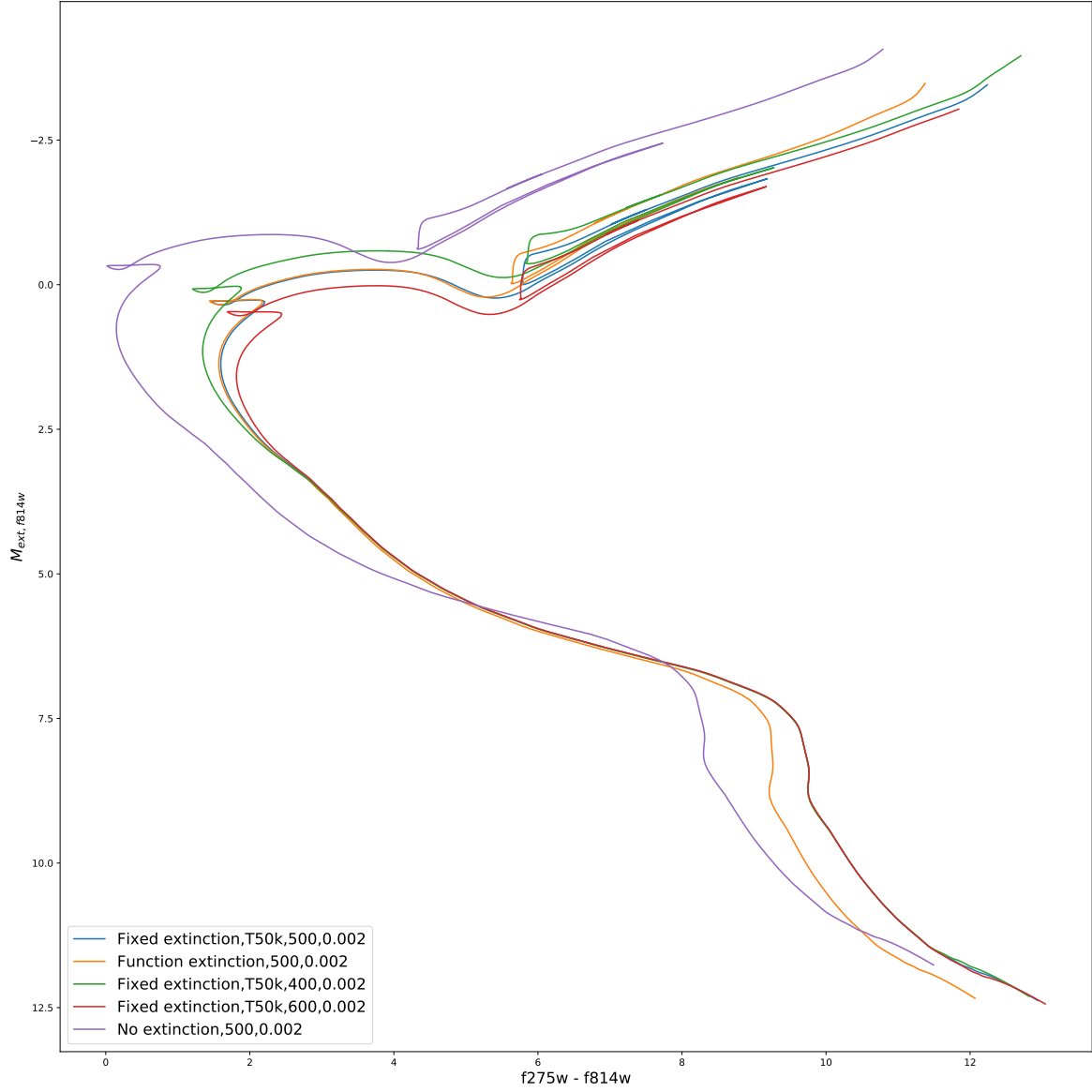


Figure 3.7: WFC3 F814W-(F275W-F814W) CMD with a fixed extinction value equal to  $(A_X/A_V)_{plat}$  for each filter

leads to those isochrones shifting down and to the right. Ironically, the higher  $T_{\text{eff}}$  value of 50,000 K used, which is far greater than any  $T_{\text{eff}}$  values present in the isochrone data, brings the MSTO positions of the two 500 Myr isochrones back into alignment. However, the use of  $(A_X/A_V)_{plat}$  increases the lower main sequence gap between the fixed-extinction and FBER isochrones. Beyond the lower main sequence, the misalignment between the two 500 Myr isochrones now begins at a later stage in the evolutionary cycle, at the base of the RGB.

Furthermore, there is a possibility of the extinction-related lower main sequence discrepancy causing a further discrepancy in the estimated metallicity when an isochrone is fitted to the observed CMD of a cluster, as the CMD position of this part of the isochrone is the most sensitive to changes in isochrone metallicity.

### 3.2.3 Gaia

The photometric filters in Gaia, as shown by their respective response functions in Figure 2.3, are designed such that the only useful colour index is the  $(G_{\text{bp}} - G_{\text{rp}})$  index, with the widest filter ( $G$ ) being on the vertical axis.

For the Gaia CMD, when  $(A_X/A_V)_{MS}$  is used for the fixed-extinction ratio isochrones, as shown in Figure 3.8, the turnoff position of the 500 Myr FBER isochrone appears to be lower on the main sequence than even the 600 Myr fixed-extinction case, suggesting that using the fixed-extinction treatment significantly and consistently over-estimates the isochrone age for an observed cluster. However, unlike the WFC3 F814W-(F275W-F814W) CMD, the alignment of the main sequence continues almost along the entire MS length.

When using  $(A_X/A_V)_{\text{plat}}$  for the fixed-extinction isochrones, the whole isochrone is significantly shifted down and to the right when moving from the FBER isochrone to the fixed-extinction isochrone, as can be seen in Figure 3.9. Since all four isochrones with added extinction in this figure assume that  $A_V = 1.0$ , alignment of the upper main sequences when using  $(A_X/A_V)_{\text{plat}}$  can only be achieved by having a lower value of  $A_V$  for the fixed-extinction isochrones than for the FBER case. Depending on the exact value of the fixed  $A_X/A_V$  used for fitting an isochrone to a given observed cluster, the resulting value calculated for  $A_V$  and, subsequently,  $E_{B-V}$  could be significantly underestimated.

## 3.3 NGC 6793

### 3.3.1 Uncertainties in observational data

The final Gaia observational sample of stars in NGC 6793 is shown as a distance-corrected CMD in Figure 2.9, with distances and photometric errors propagated directly from parallax measurements.

The uncertainties in the parallax data for objects assigned to NGC 6793 were significant for stars in the lower main sequence. This trend is to be expected, since stars in the lower main sequence are the faintest objects in the data and therefore are the

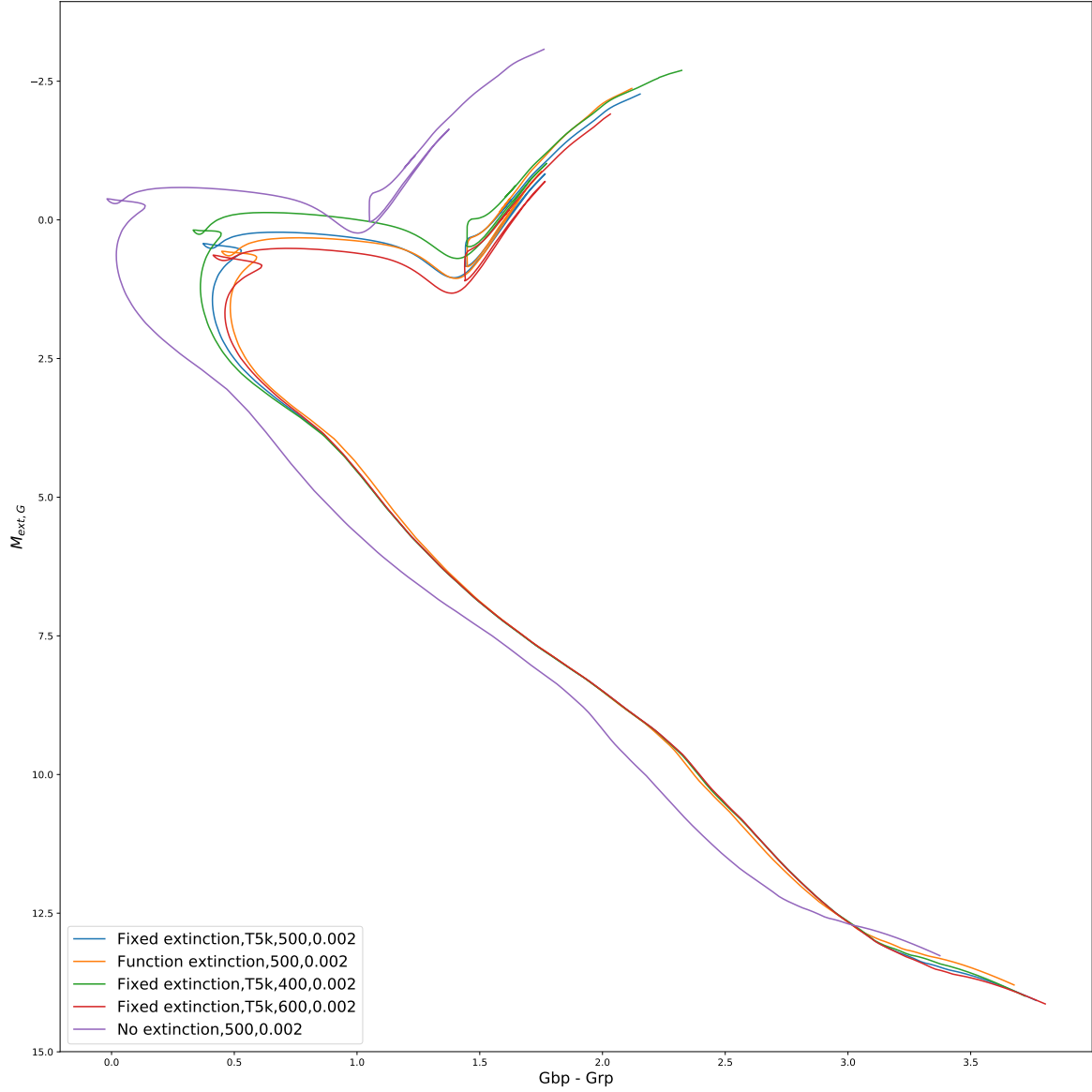


Figure 3.8: Gaia  $G-(G_{bp}-G_{rp})$  CMD with a fixed extinction value equal to  $(A_X/A_V)_{MS}$  for each filter

most difficult to track against background sources. The significance of the uncertainties persists despite this project assuming that the only sources of photometric error are the parallax measurements. This leads to uncertainties in the predicted  $M_{ext,X}$  magnitudes, which are calculated by rearranging Equation 1.1.

Since the table of photometric magnitudes did not include photometric errors, the parallax errors alone accounted for the total error in the calculated  $M_{ext,X}$  values.

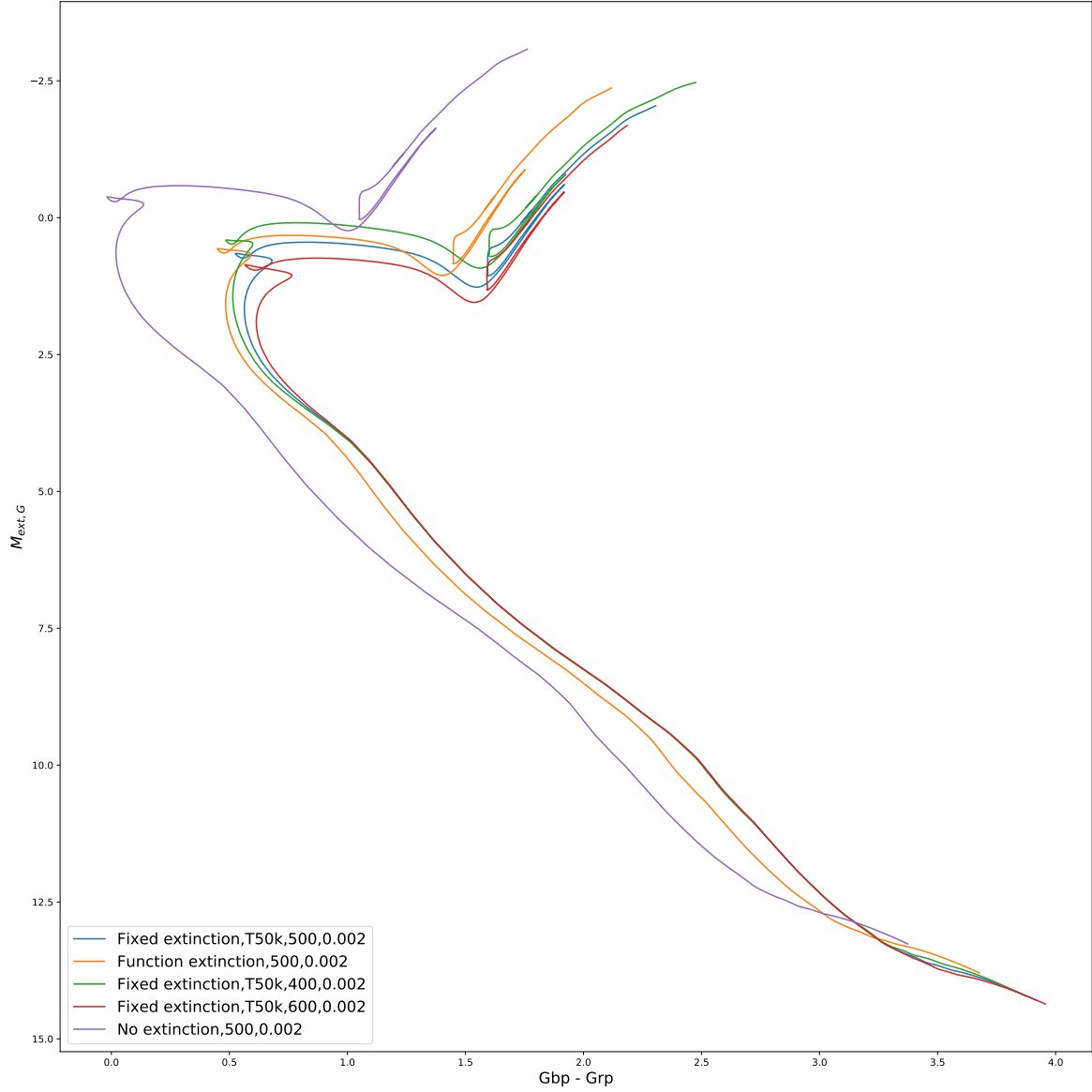


Figure 3.9: Gaia  $G$ -( $G_{\text{bp}}$ - $G_{\text{rp}}$ ) CMD with a fixed extinction value equal to  $(A_X/A_V)_{\text{plat}}$  for each filter

Therefore, the propagated errors for the  $M_{\text{ext},X}$  values were fully independent of the value of the absolute magnitude of a given star. The parallax-derived errors on the  $(G_{\text{bp}} - G_{\text{rp}})$  colour index are zero, as an object's colour index can simply be calculated as the difference between its apparent magnitudes in both filters, and is therefore independent of the object's parallax.

The uncertainties in coefficient values could have an impact on the significance

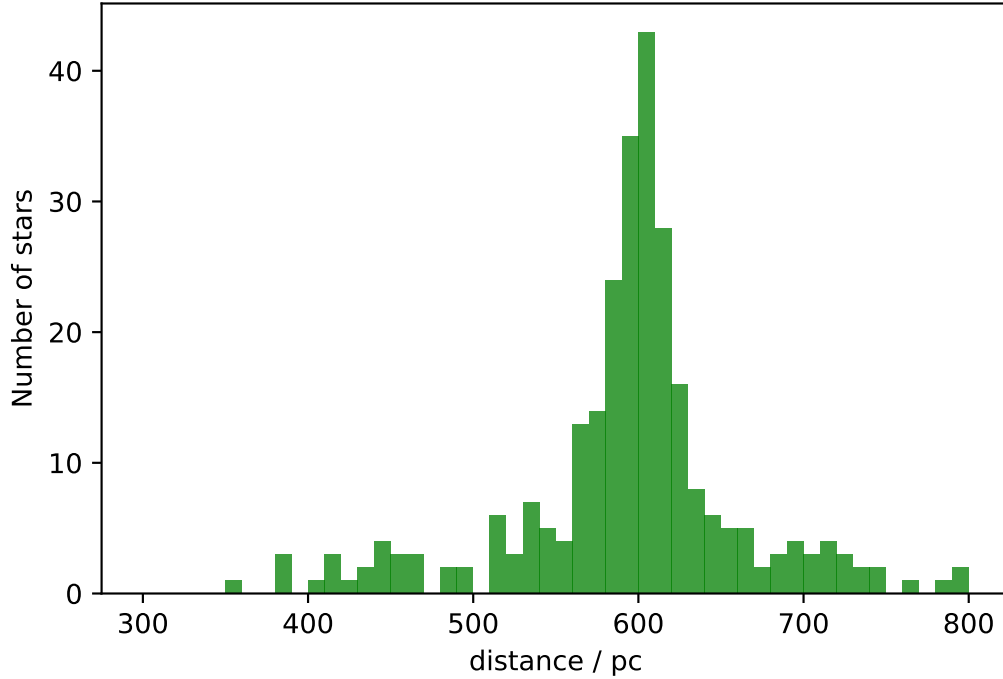


Figure 3.10: Histogram of distances for the 274\*\*\*\* stars in the final observational dataset. The bins are set to a fixed width of 10 pc.

of changing extinction treatment methods - if sufficiently large, they could render the FBER approach unnecessary. To model the uncertainty in the position of the resulting CMD isochrones, the standard deviation of each coefficient

\*\*\*\*Figure 3.14 shows the observed objects in the CMD of NGC 6793 alongside the same objects shifted downwards by 0.75 magnitudes. As outlined in Section 2.6, objects not associated with any post-MS regions of the CMD that lie 0.75 magnitudes or less directly above the actual main sequence are likely to be MS stars with unresolved binary companions. The figure shows that almost all\*\*\*\* of the purple points above the purple MS and below the MSTO region are either in or below the actual MS, indicating that these points are likely to represent stars in unresolved binary systems, and can therefore be ignored when positioning isochrones to the observed MS.

\*\*\*\*In Section 2.6, it was noted that, where there was an apparent spread in the line forming the MS, the fainter of the possible MS paths was chosen as representing the “true” MS position. This is because the effect of an unresolved photometric binary manifests itself as an increase in the flux of the observed star. The size of this increase depends on the ratio of the fluxes emitted by each of the components. The upper limit of this effect is 0.753 magnitudes, equivalent to a doubling of the observed flux, for a



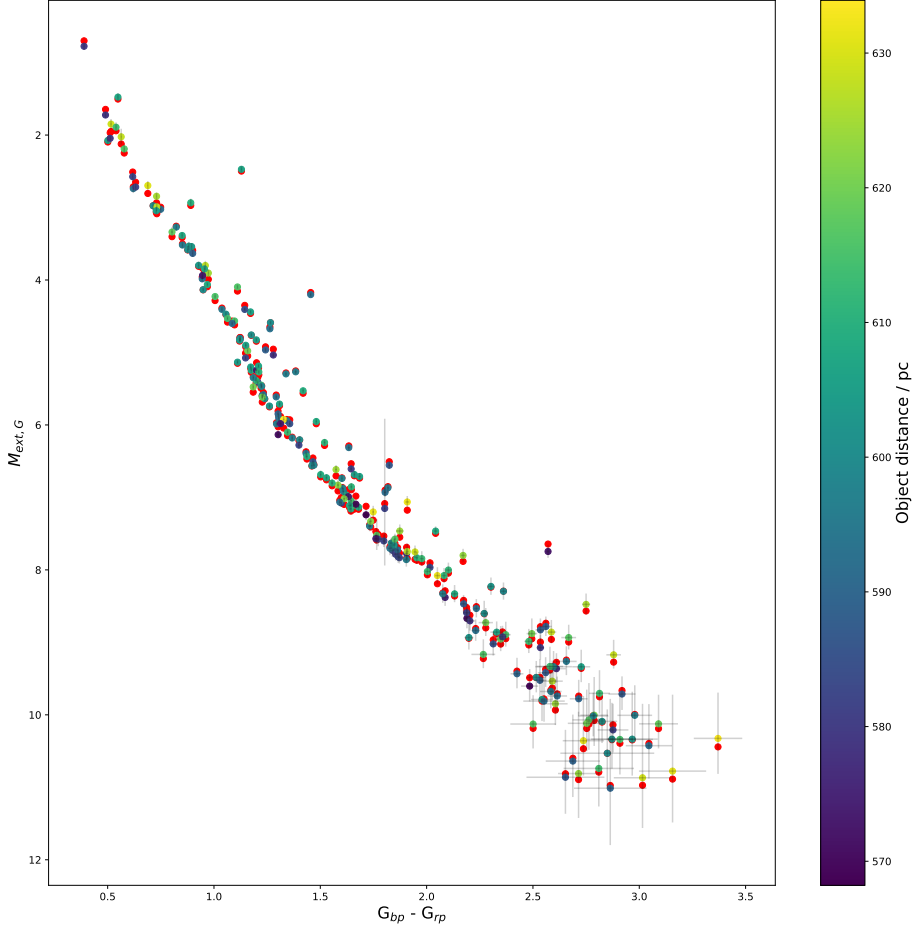


Figure 3.11: Observed CMD of NGC 6793. The distance-coloured points are cluster members whose absolute magnitudes were calculated using their individual parallax-determined observer distances. The red points denote the same data, except that the absolute magnitude were calculated using the GC18 distance value for the cluster for all the stars.

binary system composed of two identical stars. The colour index of the unresolved binary, being a difference of two magnitudes, is unaffected. Therefore, binary systems in a given cluster can be identified in a CMD as objects positioned up to 0.753 magnitudes directly above the actual MS and away from, and therefore not associated with, the post-MS regions of the CMD, such as the RGB and AGB. To illustrate the potential impact on results for NGC 6793 in this project, Figure 3.14 shows the observed CMD

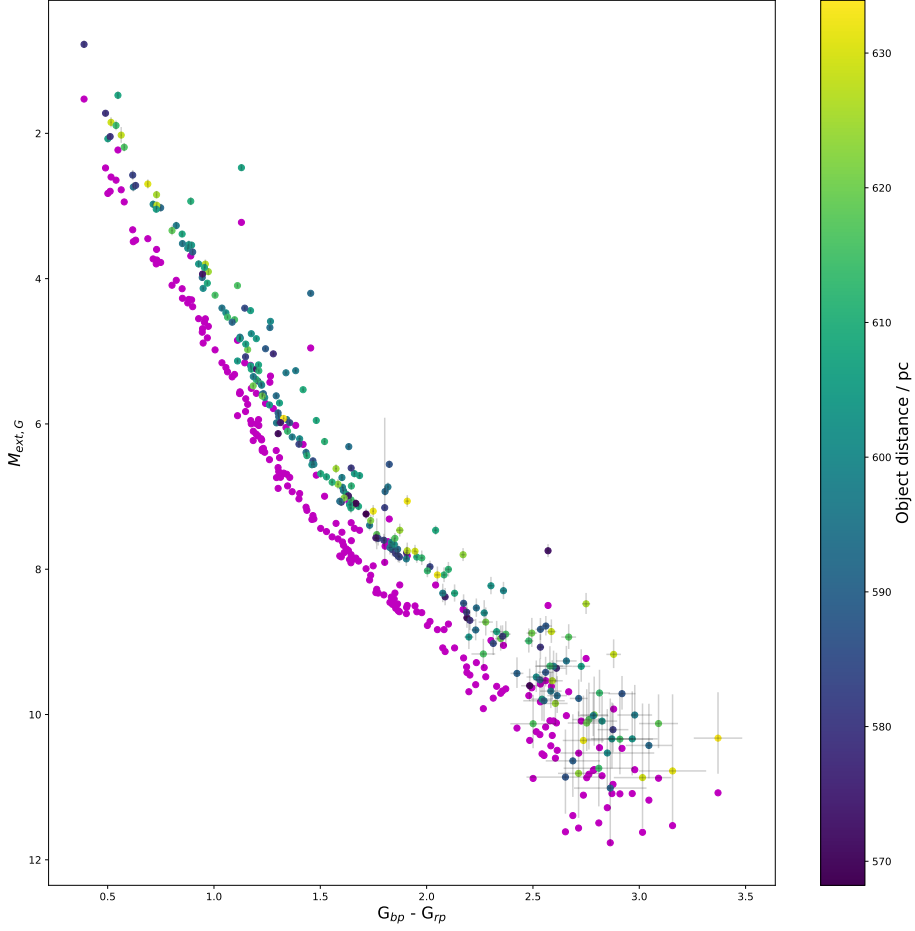


Figure 3.12: The observed CMD of NGC 6793 (coloured by object distance) overplotted with the same data shifted down in the  $M_{\text{ext},G}$  direction by 0.753. Purple points which either overlap the observed main sequence or appear between the purple and observed main sequences are likely to represent stars being affected photometrically by flux from unresolved binary companions.

data for NGC 6793 plotted twice. The purple points represent the data after it was shifted down by 0.753 magnitudes in the  $M_{\text{ext},G}$  direction. From Figure 3.14, it is clear that only a handful of MS stars have CMD positions which cannot be reconciled to the observed MS under the assumption of an undetected binary companion. Therefore, the use of the faintest MS path was justified on the basis that the vast majority of MS

stars that appeared brighter than that path can be easily reconciled with the path by uncertainties caused by potential binary companions.

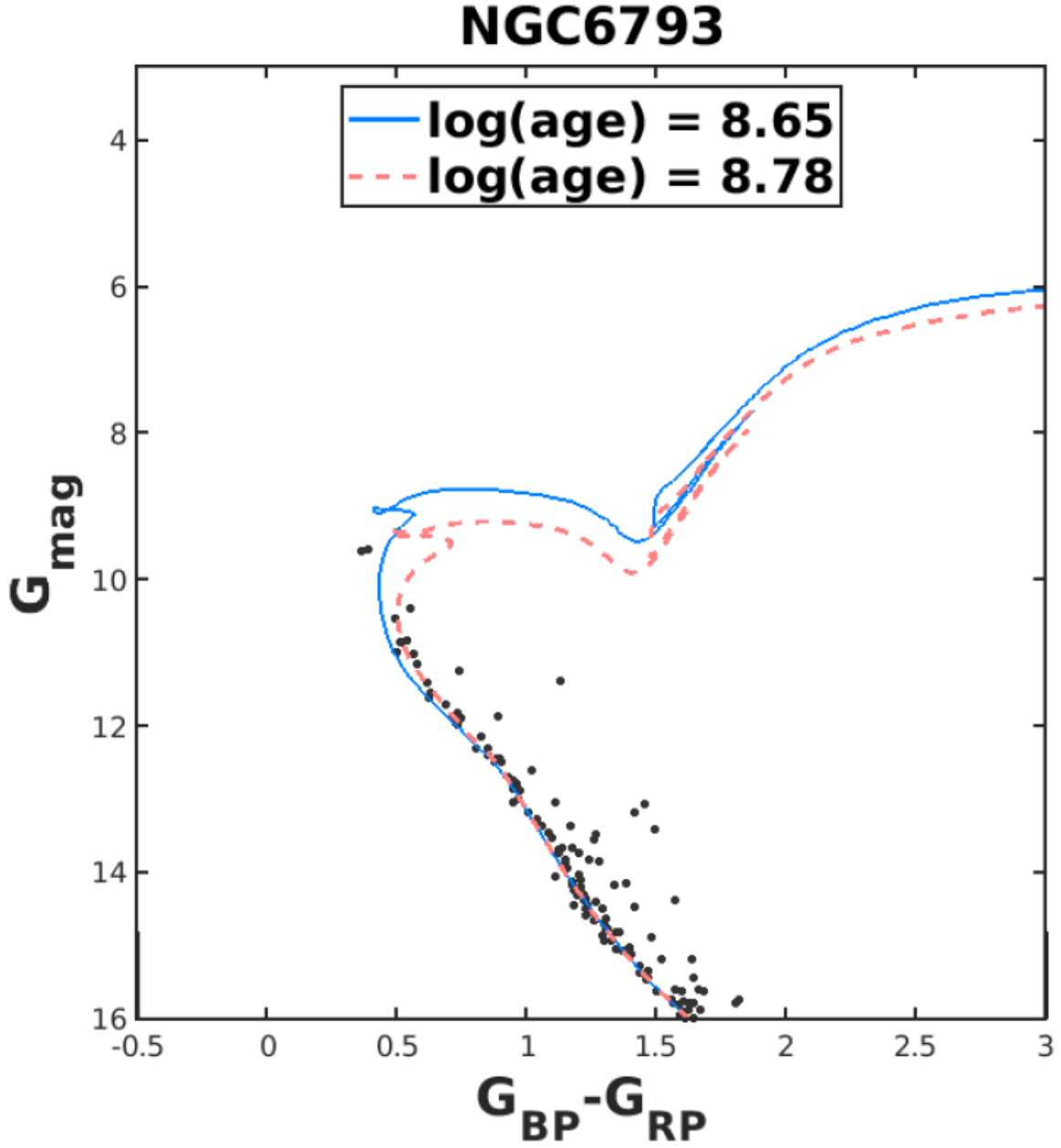


Figure 3.13: Disagreement on Gaia DR2 age estimates for NGC 6793 between GC18 (dashed red line) and Bossini et al. (2019) (solid blue line). The reasons for the disagreement are summarised in the main text. Source: Bossini et al. (2019)

Bossini et al. (2019) claim that, in the case of NGC 6793 and other clusters, the

estimated age values given by GC18 are inaccurate. In some cases the authors ascribe this as being due to the clusters being inconspicuous, while in others, including NGC 6793, they ascribe this to membership determination. For NGC 6793, they claim that a high-likelihood member at  $G \sim 9$ , as determined by Cantat-Gaudin et al. (2018), is missing from the dataset of cluster member used in GC18 and that this star, if taken to be a member of NGC 6793, causes the position of the MSTO in the cluster to change. The authors calculated that the new MSTO, instead of the GC18 value of  $\log(\text{age}) = 8.78$  (age = 603 Myr), gives an estimated value of  $\log(\text{age}) = 8.65$ , or a cluster age of 447 Myr. This indicates that the uncertainty in ages caused by the choice of extinction treatment can be less significant than uncertainty caused by disagreement over cluster membership. Such a disagreement is solely due to member selection criteria and does not impact on the difference between different methods of extinction treatment, which is the focus of this project.

However, the significance of the choice of extinction treatment is not impacted by cluster membership disagreements, as the new age estimate made by Bossini et al. (2019) is still subject to the same extinction treatment as that of GC18. As shown in Figure 3.19, in order to align the positions of best-fit isochrones generated using two different extinction treatments, there must be differences in the estimates for the cluster age,  $A_V$  and metallicity between the two isochrones. Since this result is independent of the position of the isochrones in the CMD, using a new age estimate for a fixed-extinction best-fit isochrone, with no change in the other parameters, simply requires a new estimate for the FBER isochrone, in order to realign the MSTOs in both isochrones again. This is shown in Figure ??\*\*\*\*provide a figure with EVIDENCE!!!!

Looking at the distances to the objects in the final sample shown in Figure 3.10, it is clear that there are significant variations in the observed parallaxes of individual stars, far beyond the maximum cluster radii expected for the largest open clusters, given as  $16.8 \pm 2.4$  pc by Schilbach et al. (2006) or even radii of compact stellar associations, given as  $33.2 \pm 21.7$  pc in the same paper. Some objects in the original dataset (which contains 338 members in total) were even assigned negative parallax values, which are physically impossible, as a result of measurement errors. Figure 3.10 shows a histogram of stars in the final NGC 6793 sample, binned by the parallax-derived distance. It is clear that a substantial fraction of this sample have measured parallax distances which put them outside the physical limits determined from other, better-studied open clusters, even after the distance limits outlined in Section 2.6 were imposed. On the other hand, applying stricter distance limits, in line with those given by Schilbach et al. (2006), produced a dataset with too few stars remaining to be able to reasonably determine cluster parameters. This led to the decision to impose limits resulting in a dataset of similar size to that used by GC18. In summary, therefore, there are additional uncertainties from the data due to selection of questionable sources as cluster members.

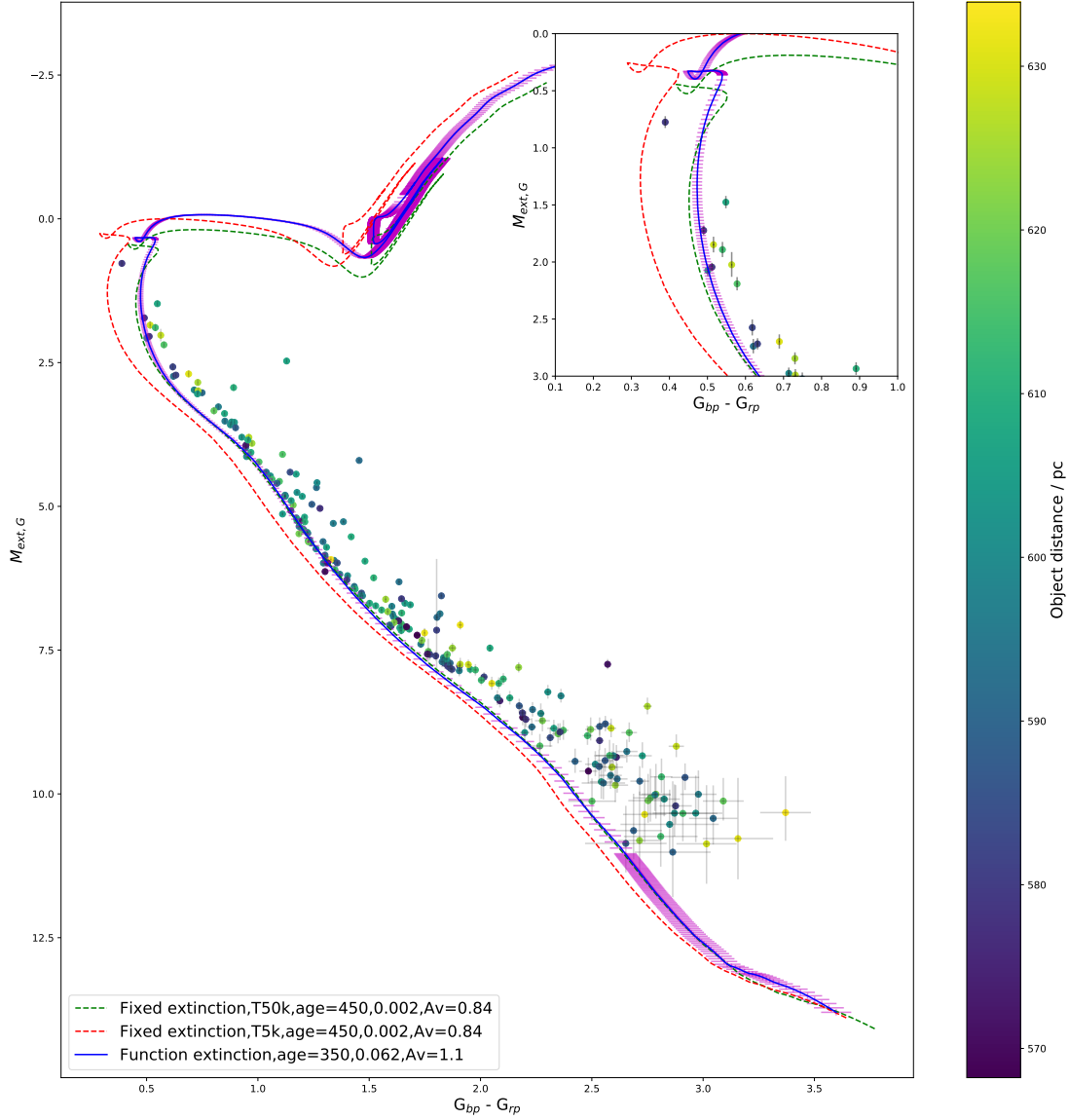


Figure 3.14: Same as Figure ??,

### 3.3.2 Isochrones

Before comparisons between the GC18 results and those for a FBER-based fit can be made, a reference isochrone, with a globally-fixed  $A_V$  value of 0.843 and age of 600 Myr (in accordance with the GC18 values in Table 2.4), was created. This was done to test whether or not a BaSTI isochrone constructed according to the GC18 results could produce an accurate fit to the observational data. The  $A_X/A_V$  values required for this isochrone to achieve alignment with the upper main sequence below the MSTO were equal to the  $(A_X/A_V)_{plat}$  values for each Gaia filter. While the results from GC18

do not include a metallicity estimate for NGC 6793, it can be estimated from its age that a solar-like metallicity is likely. Therefore, the relevant isochrone has a metallicity of  $[\text{Fe}/\text{H}] = 0$ . Due to the overall red-ward shift of an isochrone when treated with an extinction ratio of  $(A_X/A_V)_{\text{plat}}$ , rather than the physically more-realistic  $(A_X/A_V)_{\text{MS}}$ , as demonstrated in Figure 3.9, the GC18 parameter values, in particular the listed  $A_V$  value of 0.843, do not produce an accurate fit when using the FBER treatment in the isochrones for the NGC 6793 observational data.

Using the cluster parameters determined by GC18 did not produce a satisfactory fit between the FBER isochrone and the observations. As shown in Figure 3.15, the GC18 values produce an FBER isochrone whose MS lies too far beyond the blue colour-index range of the MS and thereby does not align with the position of the MSTO either, necessitating a higher value of  $A_V$  to increase the predicted colour index of the isochrone. The metallicity had to be increased in order to realign the FBER and fixed-extinction isochrones in the lower main sequence. After this, the age of the FBER isochrone needed to be lowered in order to realign the MSTO positions of the two isochrones.

Before making an age estimate, the main sequence of the FBER isochrone had to align with the MS of NGC 6793. It was found that the positions of MS objects in the region  $1.0 \lesssim (G_{\text{bp}} - G_{\text{rp}}) \lesssim 1.5$ , well below the MSTO, varied the least with changes in metallicity for the FBER isochrone, as shown in Figure 3.18. By contrast, changing the  $A_V$  value applied to the isochrone produced a more homogeneous shift in positions along the entire isochrone, as would be expected. The effect of changing between  $A_V$  values is shown in Figure 3.16, in which it can be seen that the shift is much more uniform along the length of the main sequence below the MSTO region than the MS shifts between different metallicity values shown in Figure 3.18. Therefore, the initial alignment of this region was achieved by placing greater importance on the isochrone  $A_V$  value than on the metallicity. The metallicity variations were then used to align the remaining regions of the MS with the observed data. Finally, isochrones of different ages were plotted to determine the best-fit cluster age, since the age has no significant effect on the isochrone position below the MSTO, as shown in Figure 3.17.

The alignment of the MS region described above for a FBER treatment was achieved using a value of  $A_V = 1.1$ . To better align the FBER isochrones to the lower main sequence, an increase in isochrone metallicity was required. The best-fit metallicity value was found to be  $[\text{Fe}/\text{H}] = 0.062$ . However, the magnitudes of the observational errorbars in  $M_{\text{ext},G}$  for lower MS stars (see Figure ??) dwarf any isochrone position changes due to changing between extinction treatments in the main sequence. Once these parameters were determined, the isochrone with best-fitting MSTO position had an age of 500 Myr.

The wide range of distances determined for the individual stars included in the final sample, as mentioned earlier, is orders of magnitude greater than is the case for

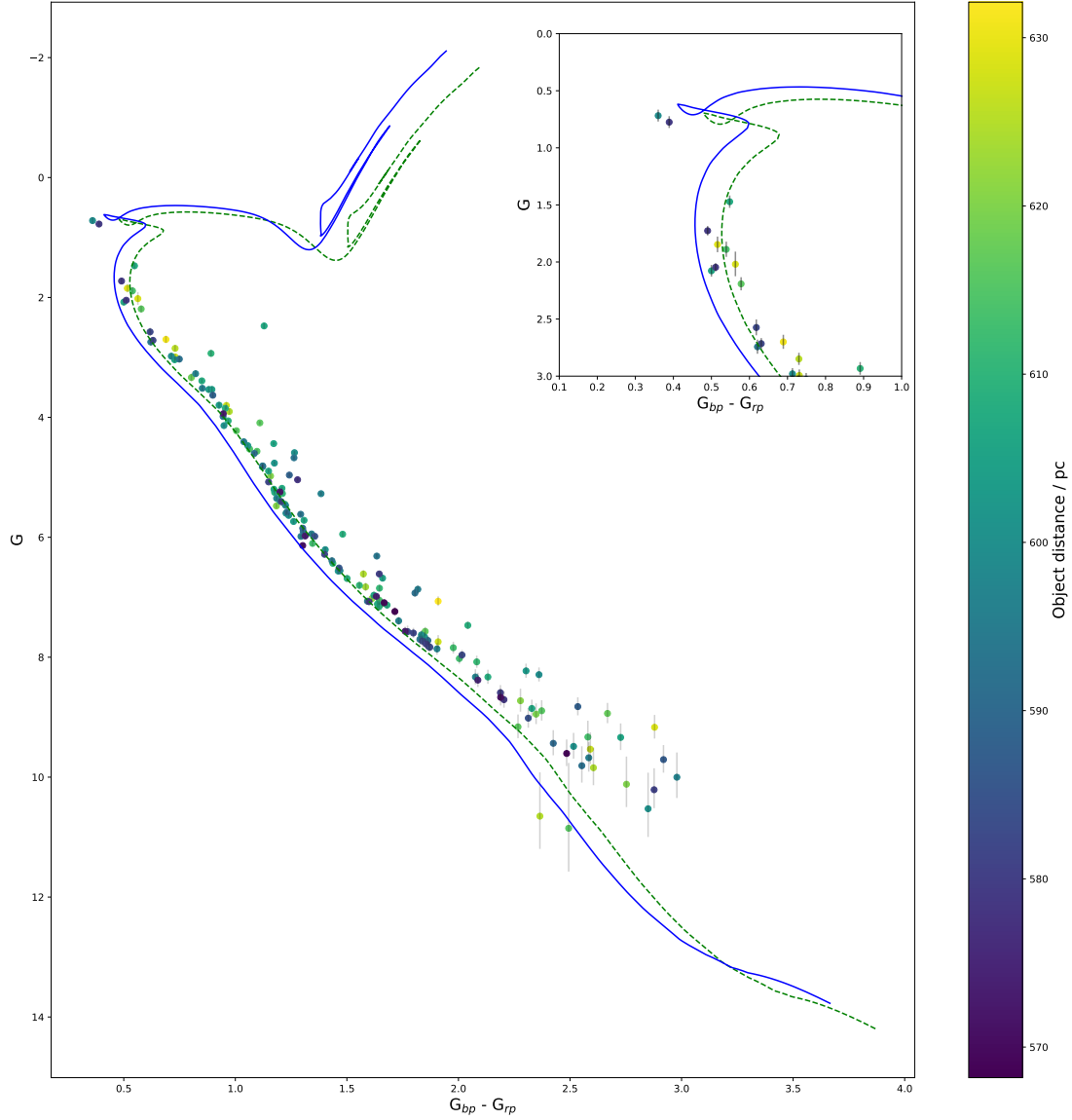


Figure 3.15: FBER treatment (solid blue) and fixed-extinction ratio (dashed green) isochrones calculated using the GC18 cluster parameters, i.e., an age of 600 Myr, an  $A_V$  value of 0.84 and solar metallicity.

the largest better-known clusters. Stars whose distances place them furthest from the projected cluster centre make up a significant portion of the objects which are widely scattered from the expected position of the main sequence. Therefore, between this and the magnitude of the errorbars in the lower main sequence in particular, the isochrone fits shown in Figure 3.19 can be considered accurate.

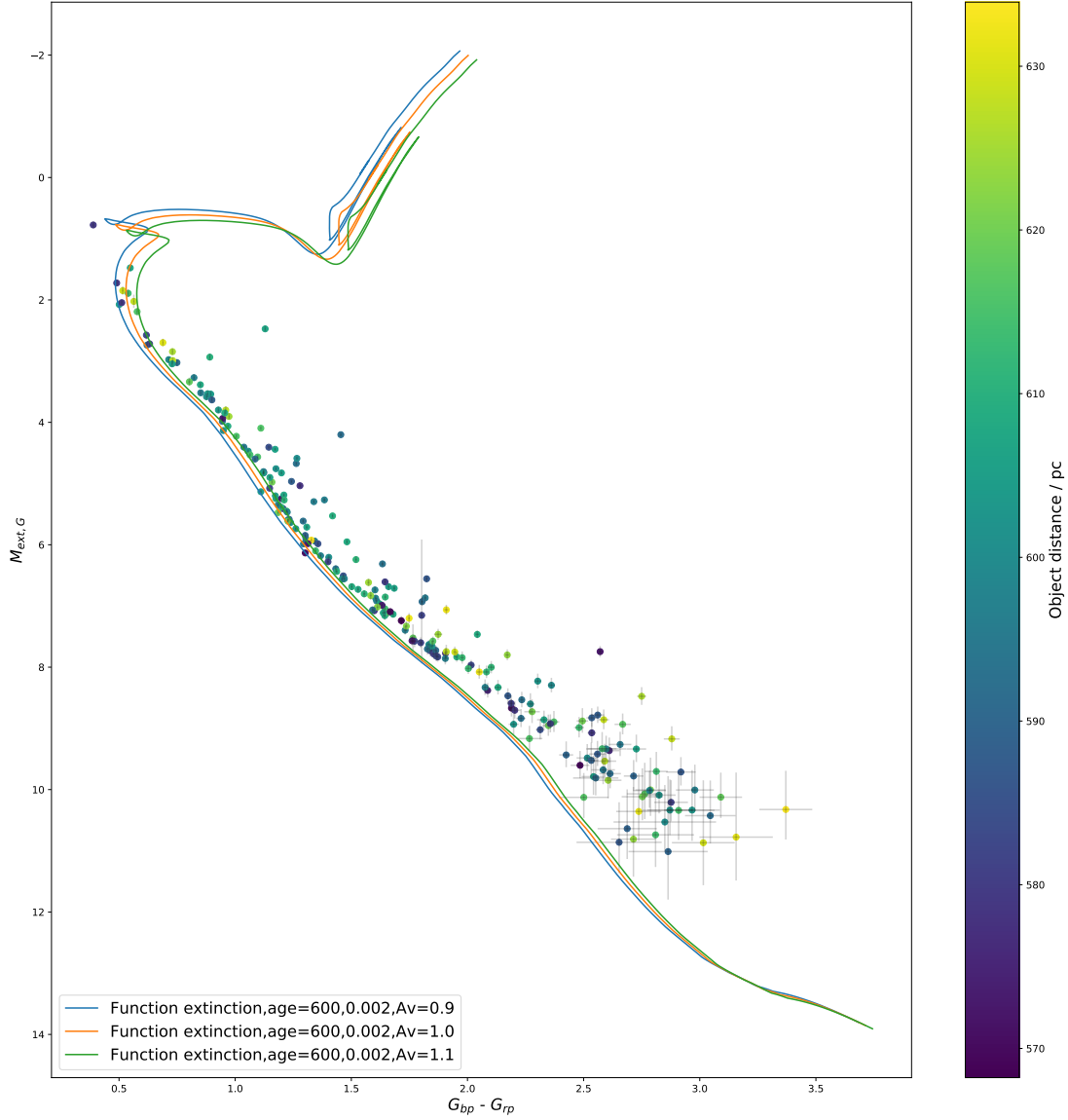


Figure 3.16: Illustration of the effect in the Gaia CMD of changing the value of  $A_V$  used in the calculation of the FBER models applied to isochrones. The observed CMD of NGC 6793 is plotted, together with three FBER isochrones, all with ages of 600 Myr and solar metallicity. The curves have  $A_V$  values of 0.9 (orange), 1.0 (green) and 1.1 (blue), respectively.

### FBER model uncertainties

The statements made in the previous section cannot be considered accurate with absolute certainty, since the FBER models, describing the changes in extinction ratios due to changes in stellar atmosphere parameters\*\*\*\*, themselves represent an additional source of uncertainty. As shown in Tables 3.1 and 3.2, the models contain uncertain-



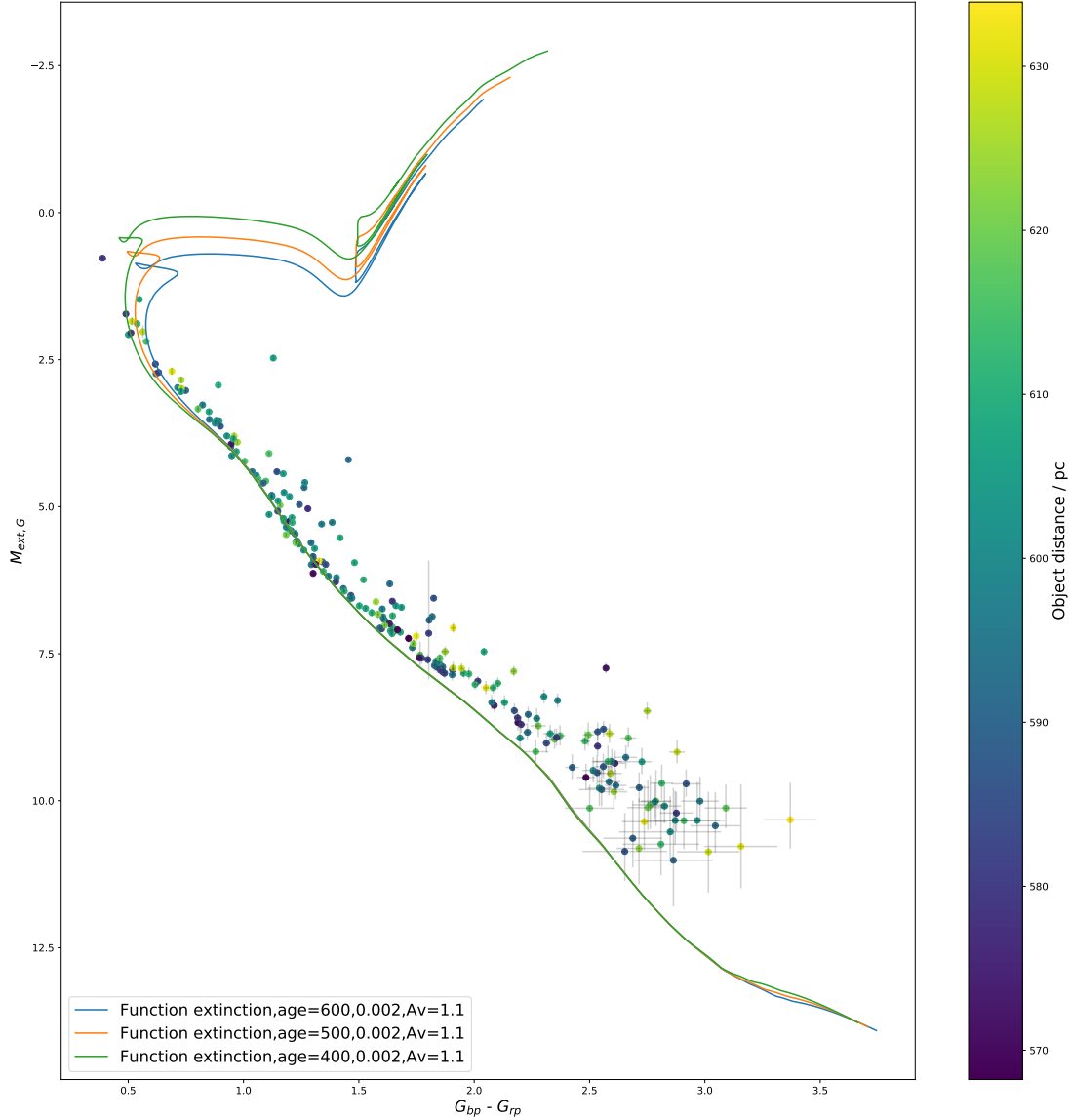


Figure 3.17: Illustration of the effect in the Gaia CMD of changing the age of an isochrone. The observed CMD of NGC 6793 is plotted, together with three FBER isochrones, all with an  $A_V$  value of 1.1 and solar metallicity. The curves have ages of 400 (green), 500 (orange) and 600 (blue), respectively.

ties which are manifested as errors in the fitted coefficient values. These errors were propagated, using the standard error-propagation formula of partial derivatives with respect to each coefficient, to produce an estimate for the errors in  $A_X/A_V$  for these models. Since each photometric filter has an independently-fitted function with different coefficients and errors, each of the three filters used for the CMD has an associated FBER model error. For the  $G_{bp} - G_{rp}$  axis, the error in the extinction ratio for the

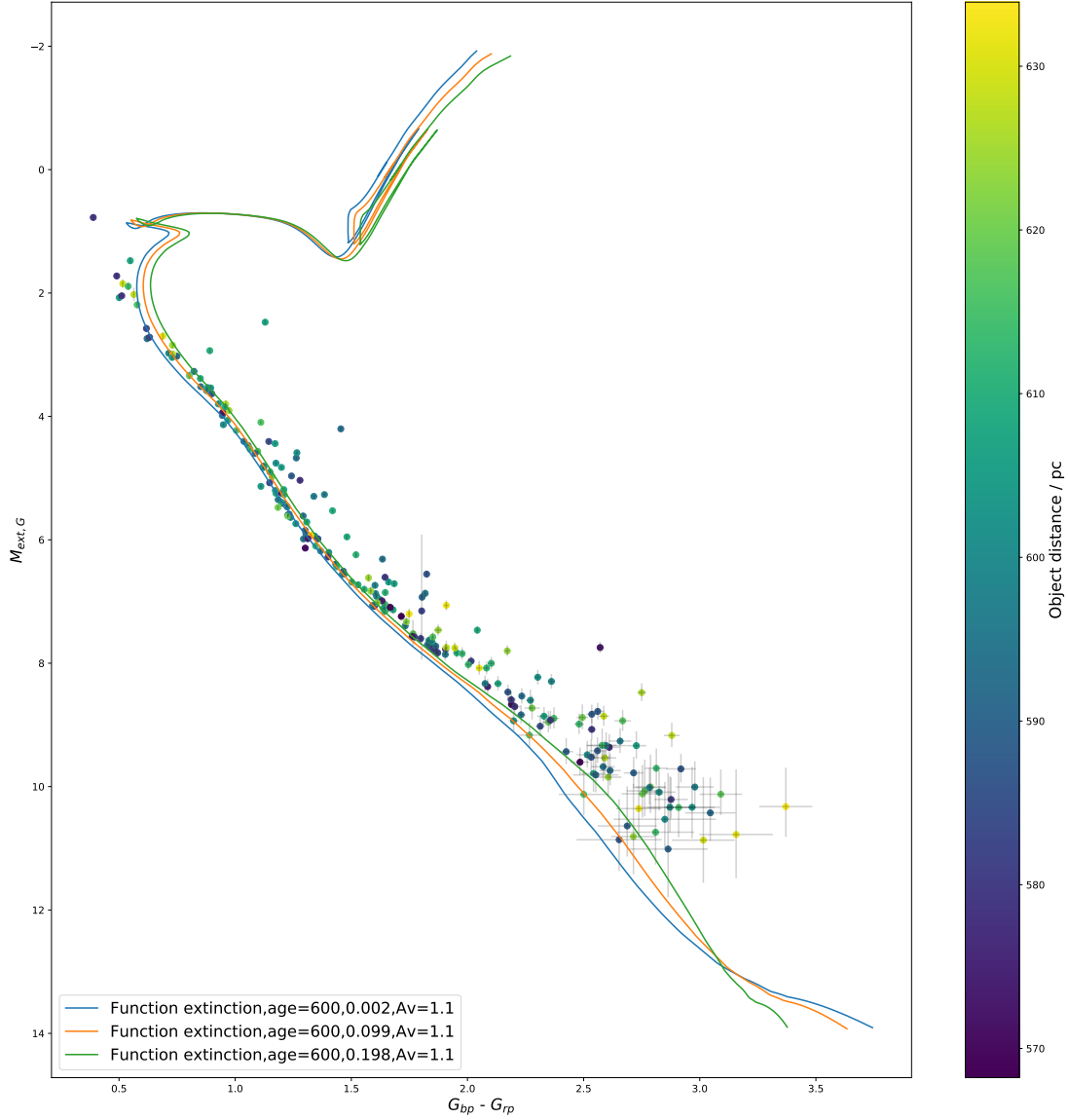


Figure 3.18: Illustration of the effect in the Gaia CMD of changing the metallicity of an isochrones. The observed CMD of NGC 6793 is plotted, together with three FBER isochrones, all with ages of 600 Myr and an  $A_V$  value of 1.1. The curves have  $[\text{Fe}/\text{H}]$  values of 0.0 (blue), 0.1 (orange) and 0.2 (green), respectively.

colour index was obtain by adding the individual filters' uncertainties in quadrature.

\*\*\*\*Once the FBER error estimates for  $M_{\text{ext},G}$  and  $G_{bp} - G_{rp}$  were obtained, they were applied to the isochrone dataset and the results were plotted as errorbars originating from the FBER isochrone, as shown in Figure 3.20. Errorbars were chosen over shading regions within the  $1\sigma$  uncertainty range because of complications in the

Cluster property	K05	K13	GC18	This project
Age / Myr	437	495	603	500
$A_V$ / mag	0.53	0.967	0.843	1.1
[Fe/H]	?	?	?	0.062
Members	?	133	271 (photometric)	274

Table 3.3: Comparison of results from this project with results of previous studies of NGC 6793.

RGB-HB-AGB region which resulted in incorrect shading in that region.

From the errorbars in Figure 3.20, it is clear that the differences in cluster parameters resulting from the use of different extinction treatment methods, as summarised in Table 3.3, cannot be reconciled even when considering the uncertainties in both the observational data and the empirical  $A_X/A_V$  models.

### Uncertainties due to choice of software

The conclusion that different extinction treatment methods produce different cluster parameter estimates could have its validity undermined by a different source of uncertainty. When comparing the best-fit isochrone results of this project for NGC 6793 with those from GC18, this project employs the latest BaSTI isochrone database (Hidalgo et al., 2018) for the fixed-extinction treatment, while GC18 uses the PARSEC isochrone database (Marigo et al., 2017) for the same. This project’s use of isochrones generated by a different model stellar evolution code from that used by GC18 could impact the validity of comparing the  $A_V$  values, ages and metallicities arising from both extinction treatments.

A recent comparison of isochrones, including those generated using BaSTI and PARSEC, was made by Gontcharov et al. (2019). The authors carried out a detailed set of observations of the Galactic globular cluster NGC 5904 in 29 photometric bands. The CMDs created from these data were used to fit isochrones from five different databases, including PARSEC and BaSTI. They adopted the Cardelli et al. (1989) extinction law with the parameters having values of  $R_V = 3.60 \pm 0.05$  and  $A_V = 0.20 \pm 0.02$ . As shown in Table 3.4, the Gaia colour excess  $E(G_{bp} - G_{rp})$  for NGC 5904 differs significantly between the best-fits from the two databases, which in turn causes disagreements for the projected cluster age and (photometric) distance. Across all filter systems and isochrone databases, the authors calculated mean estimates of the cluster properties and found that the resulting photometric distance to be in agreement with the cluster distance calculated from the Gaia parallaxes of the cluster members.

In the case of the analysis of NGC 6793 carried out in this project, the distance

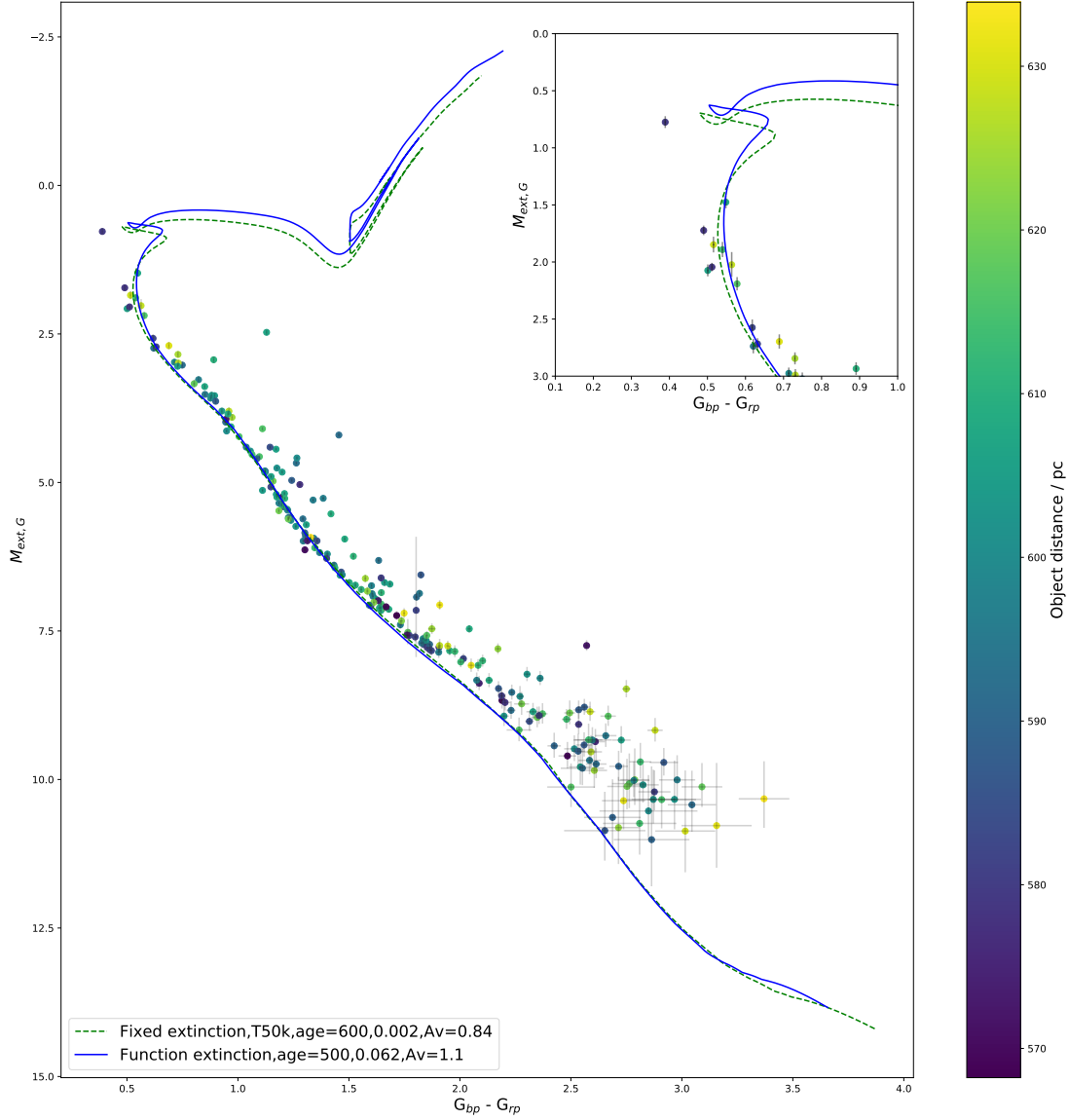


Figure 3.19: Gaia  $G$ -( $G_{bp}$ - $G_{rp}$ ) CMD of NGC 6793, showing the 274 distance-corrected cluster members in the final dataset overlaid with a isochrone treated with a fixed extinction-ratio value of  $(A_X/A_V)_{plat}$  and age,  $A_V$  and  $[\text{Fe}/\text{H}]$  values taken from the GC18 results in Table 2.4 and a 500-Myr FBER isochrone (solid blue) with an  $A_V$  value of 1.1 and a metallicity of  $[\text{Fe}/\text{H}] = 0.062$ , with observational errorbars added. The inset panel shows a zoomed-in view of the MSTO region.

measurements are derived from Gaia parallax measurements and so are unaffected by the choice of model stellar evolution code used to generate isochrones, allowing the GC18 cluster distance to be validly assumed here (as 600 pc to the cluster centre). Furthermore, using the PARSEC-derived parameters from GC18, an accurate BaSTI

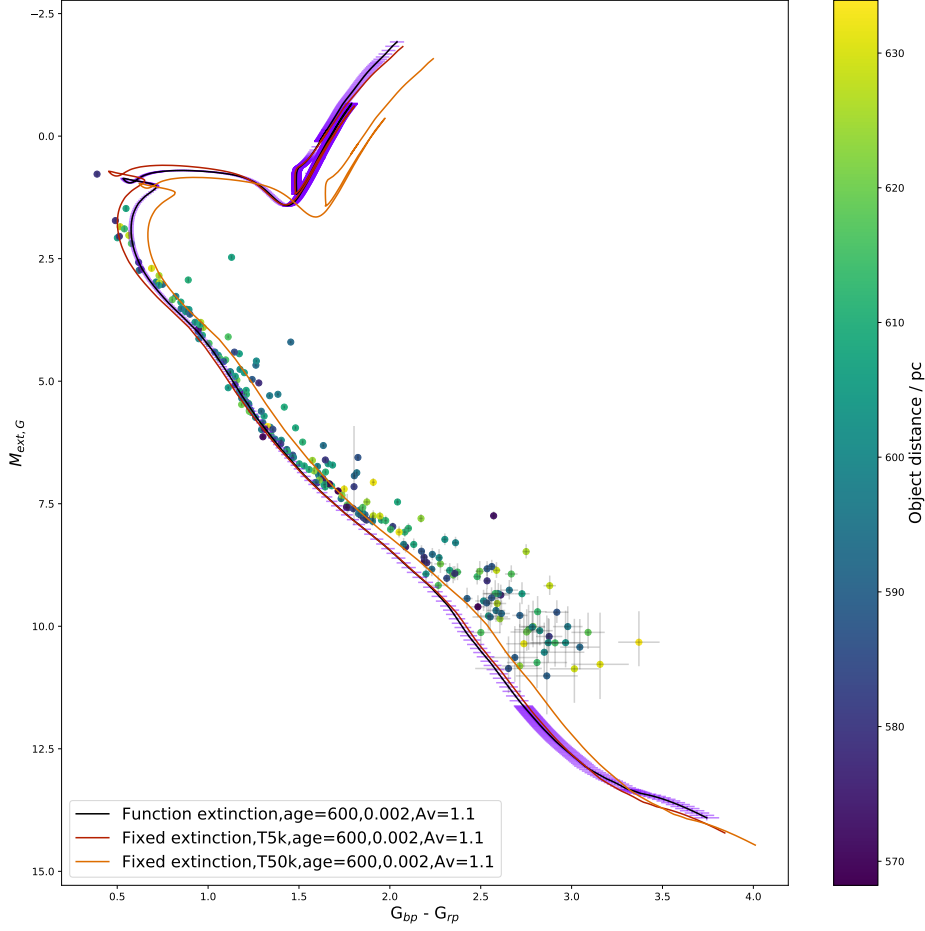


Figure 3.20: Observed CMD of NGC 6793, with three extinction scenario cases plotted over the observed data. All three isochrones have the same cluster parameter values, as shown in the legend. The curve treated using the FBER models introduced in this project is shown in black. The uncertainties in these models, whose calculation is briefly described in the text, are shown in both axes via the purple errorbars. The fixed-extinction models generated using  $(A_X/A_V)_{plat}$  and  $(A_X/A_V)_{MS}$  are shown in light orange and brown, respectively.

model isochrone for NGC 6793 was calculated successfully for a fixed  $A_X/A_V$  extinction model. Therefore, it was concluded that the validity of comparing the respective  $A_X$ ,  $[\text{Fe}/\text{H}]$  and age values from GC18 and this project was not endangered by the use of different isochrone databases by each study.

Cluster property	PARSEC	BaSTI
$E(G_{\text{bp}} - G_{\text{rp}}) / \text{mag}$	$0.080 \pm 0.02$	$0.013 \pm 0.03$
Age / Gyr	11.5	12.5
Distance / pc	7600	8400

Table 3.4: Comparison of best-fit parameter results for NGC 5904 using PARSEC and BaSTI. Data taken from Gontcharov et al. (2019).

As predicted by the comparisons made for isochrones in the Gaia CMD in Section 3.2.3, the isochrone with a FBER at the GC18 estimated value of  $A_V = 0.843$  is systematically too blue and too bright to fit to the observed CMD of NGC 6793. This remains the case regardless of changes in age and metallicity. Therefore, as predicted, there is significant disagreement between the best-fitting  $A_V$  values for the two extinction-calculation methods.

There are considerable uncertainties for the parameters in both of the isochrones plotted in Figure 3.19. Most fundamentally, the position of the MSTO is reliant only on the position of the four brightest cluster members, of which the brightest two, if the positions of the isochrones are taken to be accurate, appear to be part of part of the cluster’s MS hook. The objects’ parallax errors, as shown in Figure 2.11, are large enough to make the effect of any changes in metallicity for either isochrone insignificant. On the other hand, any significant changes in  $A_V$  and age cause misalignment of the main sequence and MSTO, respectively, with the observational data, making analysis of their impact on the MS hook region unnecessary.

\*\*\*\*The two objects to the right of the MS which appear to form a straight line connecting to the MS at  $M_{\text{ext},G} \approx 3 - 3.5$  were not considered to represent the location of the MSTO due to the much larger number of blue stragglers than MSTO objects that would result from placing the MSTO there. Furthermore, the shape of the would-be MSTO region does not match the shape of the same region in any isochrone tested on the region. Overall, therefore, the MS region at  $M_{\text{ext},G} \approx 3 - 3.5$  cannot be the MSTO region.

Looking at the CMD number density of member objects along the upper main sequence of NGC 6793, specifically for the region  $M_{\text{ext},G} < 5$ , it would be expected that main sequence stars at and below the MSTO heavily outnumber any blue stragglers constituting any population of MS-like objects above the MSTO point. Since the number density of stars in the upper MS is relatively uniform until  $M_{\text{ext},G} \approx 1.5$ , it was considered that regions fainter than this point were unlikely to represent locations above which the number density would markedly decrease, and therefore were unlikely to represent the location of the MSTO and the start of the blue straggler population.

This assessment agrees with those made by GC18 and Bossini et al. (2019). Since the observational data used in this project to determine the MSTO location is the same as that used by GC18, but not in Bossini et al. (2019), it was considered that using the same CMD location as GC18 for the MSTO would be advantageous, particularly since any differences in the estimated cluster age between the fixed-extinction and FBER isochrones would not be affected by uncertainty regarding the relative locations of the MSTO for each of these isochrones.

In summary, the use of different stellar models for isochrones in GC18 and this project was found to have no significant impact when comparing the resulting parameter values for the NGC 6793 Gaia data. The use of the FBER treatment on isochrones, when applied to the Gaia CMD for NGC 6793, required significant changes in the values of  $A_V$ , metallicity and age for the best-fitting isochrone, compared with those derived by GC18, to align with the observed sample of stars in the cluster (see Table 3.3 for details). Using the FBER treatment results in an observed sample requiring higher  $A_V$  extinction, higher metallicity and, most importantly, a younger age in its best-fitting isochrone, compared to the standard fixed-extinction ratio treatment. Furthermore, the best-fit isochrones for both treatments have a similar level of accuracy to the observational data. However, the significance of the results is impacted by the lack of photometric errors in the Gaia data used in this project. The age difference in particular is important, as this project has shown that it occurs in other CMDs and instruments, so there is the potential for this difference to occur for a large number of observations for different star clusters. If this apparent age discrepancy is found to occur for a significantly large number of star clusters, it could potentially cause a revision of the history of star clusters and, subsequently, their host galaxies.

# Chapter 4

## Conclusion

This project aimed to use theoretical stellar atmosphere data to map variations in the extinction ratios  $A_X/A_V$  in three different photometric filter systems as the atmospheric effective temperature, surface gravity and metallicity were varied. The greatest variations in  $A_X/A_V$  for all filters were found to occur with variations in effective temperature, with variations due to changes in metallicity and surface gravity found to be much smaller, as expected. Within individual filters, the greatest range of  $A_X/A_V$  values occurred for UV filters, with the range decreasing with increasing filter wavelength, again in line with previous predictions and observational evidence. Mathematical functions were constructed and their coefficients fitted to the  $A_X/A_V$  data in each filter. The resulting functions were able to describe the data to a reasonable degree of accuracy, and are therefore a suitable, and much simpler, substitute for performing interpolation on tables of  $A_X/A_V$  data.

The  $A_X/A_V$  values generated by applying these functions to objects in an isochrone were then added to those objects (the FBER method). The isochrone was then plotted in selected CMDs alongside the same isochrone to which a fixed value of  $A_X/A_V$  was applied to all objects. This allowed the effects of the FBER and fixed extinction ratio methods on the isochrone position in the CMD to be compared.

In all the CMDs studied in this project, applying a fixed value of  $A_X/A_V$  to the entire isochrone causes the main-sequence turn-off to occur at a more luminous, bluer point in a given CMD than the MSTO point for the same isochrone with extinction values derived using the FBER method. The significance of this position change is dependent on the filters used to construct the particular CMD in question. The position changes in two of the four CMDs studied are insignificant.

The WFC3 F814W-(F275W-F814W) CMD shows significant differences between the positions of certain sections of isochrones treated under different extinction-calculation methods, particularly for the lower main sequence but also for the MSTO, depending on the value of  $A_X/A_V$  used in the fixed-extinction case. This is a consequence of the



much larger variation of extinction between different stellar types in the UV spectral range.

The Gaia photometric CMD is highly sensitive to both the choice of extinction-calculation method and the choice between  $(A_X/A_V)_{plat}$  and  $(A_X/A_V)_{MS}$  for the fixed-extinction ratio method. This underscores the substantial risk of incorrect assumptions being made when fitting isochrones to observational data with a single globally-fixed  $A_X/A_V$  value across all constituent stellar model objects, which in turn leads to incorrect estimates of important cluster parameters, as was demonstrated in detail here for the open cluster NGC 6793.

## 4.1 Future work

There are multiple ways to extend the applicability of the work done in this project. The most obvious examples are to study more CMDs in the filter systems used in this project and to utilise the filter response functions for more filter systems, particularly for more modern and more sensitive instruments, such as the James Webb Space Telescope (JWST) and the proposed WFIRST and PLATO space telescopes, to create FBER models for observations made with these instruments.

Another extension would be to apply the FBER method to observed clusters with isochrone ages previously determined using the fixed-extinction ratio method. If, as predicted for the limited examples studied in this project, the isochrone ages of a given cluster CMD are greater when employing a fixed-extinction method, there is the possibility of a systematic decrease in the predicted ages of these observed clusters after comparison with ages derived using an FBER method.

Regarding the case of NGC 6793, follow-up observations with Johnson-Cousins filters, if feasible, could resolve the  $A_V$  disagreement between the extinction-calculation methods by providing a direct measured value upon which the Gaia extinction ratios can be calculated.

Finally, the limits on the accuracy of the model functions presented here require investigation, particularly the accuracy limit at the lowest  $T_{\text{eff}}$  values available from ATLAS9. This could be done using the same approach as that used by Girardi et al. (2008), who use SEDs generated from sources other than ATLAS9 to extend their bolometric correction database to a minimum  $T_{\text{eff}}$  of  $\sim 1000$  K. The coolest known stellar objects (excluding brown dwarfs) have  $T_{\text{eff}} \sim 2500$  K. Extending the dataset would constrain the allowed behaviour of the model functions for the lowest ATLAS9 effective temperatures. The lack of data below 3500 K for this project prevents investigation of the significance of the tail-flick phenomenon, since the phenomenon, at present, ex-

tends to (and possibly beyond) the lower  $T_{\text{eff}}$  limit for the affected filters in ATLAS9.

# Bibliography

- Beichman C. A., Neugebauer G., Habing H. J., Clegg P. E., Chester T. J., 1988, in Infrared astronomical satellite (IRAS) catalogs and atlases. Volume 1: Explanatory supplement.
- Bertelli G., Bressan A., Chiosi C., Fagotto F., Nasi E., 1994, A&A Suppl. Ser., 106, 275
- Bessell M. S., 1990, PASP, 102, 1181
- Bessell M. S., 2005, ARAA, 43, 293
- Bossini D., et al., 2019, A&A, 623, A108
- Cantat-Gaudin T., et al., 2018, A&A, 618, A93
- Cardelli J. A., Clayton G. C., Mathis J. S., 1989, ApJ, 345, 245
- Casagrande L., VandenBerg D. A., 2014, MNRAS, 444, 392
- Casagrande L., VandenBerg D. A., 2018a, MNRAS, 475, 5023
- Casagrande L., VandenBerg D. A., 2018b, MNRAS, 479, L102
- Castelli F., Kurucz R. L., 2004, ArXiv Astrophysics e-prints
- Dias W. S., Assafin M., Flório V., Alessi B. S., Líbero V., 2006, A&A, 446, 949
- Fitzpatrick E. L., 1999, PASP, 111, 63
- Flower P. J., 1996, ApJ, 469, 355
- Forbes J. D., 1842, Philosophical Transactions of the Royal Society of London Series I, 132, 225
- Gaia Collaboration et al., 2018, A&A, 616, A10
- Girardi L., Bertelli G., Bressan A., Chiosi C., Groenewegen M. A. T., Marigo P., Salasnich B., Weiss A., 2002, A&A, 391, 195

- Girardi L., et al., 2008, *PASP*, 120, 583
- Gontcharov G. A., 2016, *Astrophysics*, 59, 548
- Gontcharov G. A., Mosenkov A. V., Khovritchev M. Y., 2019, *MNRAS*, 483, 4949
- Grainger R. G., Lucas J., Thomas G. E., Ewen G. B. L., 2004, *Appl. Opt.*, 43, 5386
- Grebel E. K., Roberts W. J., 1995, *A&A Suppl. Ser.*, 109, 293
- Gustafsson B., Edvardsson B., Eriksson K., Jørgensen U. G., Nordlund Å., Plez B., 2008, *A&A*, 486, 951
- Hidalgo S. L., et al., 2018, *ApJ*, 856, 125
- Johnson H. L., Morgan W. W., 1953, *ApJ*, 117, 313
- Jordi C., et al., 2010, *A&A*, 523, A48
- Kalirai J. S., Baggett S., Borders T., Rajan A., 2010, Technical report, The Photometric Performance of WFC3/UVIS: Temporal Stability Through Year 1
- Kharchenko N. V., Pakulyak L. K., Piskunov A. E., 2003, *Astronomy Reports*, 47, 263
- Kharchenko N. V., Piskunov A. E., Röser S., Schilbach E., Scholz R.-D., 2005, *A&A*, 438, 1163
- Kharchenko N. V., Piskunov A. E., Schilbach E., Röser S., Scholz R. D., 2013, *A&A*, 558, A53
- Kurucz R., 1993, *ATLAS9 Stellar Atmosphere Programs and 2 km/s grid*. Kurucz CD-ROM No. 13. Cambridge, Mass.: Smithsonian Astrophysical Observatory, 1993., 13
- Lagioia E. P., et al., 2018, *MNRAS*, 475, 4088
- Landgraf M., Krüger H., Altobelli N., Grün E., 2003, *Journal of Geophysical Research (Space Physics)*, 108, 8030
- MacKenty J. W., Kimble R. A., O’Connell R. W., Townsend J. A., 2010, in *Space Telescopes and Instrumentation 2010: Optical, Infrared, and Millimeter Wave*. p. 77310Z
- Marigo P., et al., 2017, *ApJ*, 835, 77
- Mie G., 1908, *Annalen der Physik*, 330, 377
- O’Donnell J. E., 1994, *ApJ*, 422, 158
- Ohvri H., Okulov O., Teral H., Teral K., 1999, *Solar Energy*, 66, 305

- Ortolani S., Cassisi S., Salaris M., 2017, *Galaxies*, 5, 28
- Pajot F., et al., 2006, *A&A*, 447, 769
- Pietrinferni A., Cassisi S., Salaris M., Castelli F., 2004, *ApJ*, 612, 168
- Pols O. R., Schröder K.-P., Hurley J. R., Tout C. A., Eggleton P. P., 1998, *MNRAS*, 298, 525
- Rieke G. H., Lebofsky M. J., 1985, *ApJ*, 288, 618
- Sahu K., Deustua S., Sabbi E., 2014, Technical report, WFC3/UVIS Photometric Transformations
- Sarajedini A., et al., 2007, *ApJ*, 133, 1658
- Schilbach E., Kharchenko N. V., Piskunov A. E., Röser S., Scholz R.-D., 2006, *A&A*, 456, 523
- Siegel M. H., LaPorte S. J., Porterfield B. L., Hagen L. M. Z., Gronwall C. A., 2019, *ApJ*, 158, 35
- Sirianni M., et al., 2005, *PASP*, 117, 1049
- Valencic L. A., Clayton G. C., Gordon K. D., 2004, *ApJ*, 616, 912
- Witt A. N., 2000, *Journal of Geophysical Research (Space Physics)*, 105, 10299